Dissolution Phenomena of Nuclear Research Reactor Fuel Constituents in Molten Salt Systems

A Dissertation

Presented in Partial Fulfillment of the Requirements for the

Degree of Doctor of Philosophy

with a

Major in Chemical Engineering

in the

College of Graduate Studies

University of Idaho

by

Steven D. Herrmann

Major Professor: Haiyan Zhao, Ph.D.

Committee Members: Vivek Utgikar, Ph.D.; Eric Aston, Ph.D.; Shelly X. Li, Ph.D.

Department Administrator: Ching-An Peng, Ph.D.

May 2021

Authorization to Submit

This dissertation of Steven D. Herrmann, submitted for the degree of Doctor of Philosophy with a Major in Chemical Engineering and titled, "Dissolution Phenomena of Nuclear Research Reactor Fuel Constituents in Molten Salt Systems," has been reviewed in final form. Permission, as indicated by the signatures and dates below, is now granted to submit final copies to the College of Graduate Studies for approval.

Major Professor: Concurrence provided electronically Date: April 30, 2021
Haiyan Zhao, Ph.D.

Committee Members: Concurrence provided electronically Date: April 30, 2021
Vivek Utgikar, Ph.D.

Concurrence provided electronically Date: April 30, 2021
Eric Aston, Ph.D.

Concurrence provided electronically Date: April 30, 2021
Shelly X. Li, Ph.D.

Department Administrator: Concurrence provided electronically Date: April 30, 2021
Ching-An Peng, Ph.D.

Abstract

In its 70-year history, Idaho National Laboratory has pioneered significant nuclear advancements and enduring technologies, including liquid metal reactors with an accompanying electrometallurgical treatment process for conditioning the reactor's used metallic fuels, pressurized water reactors operating with uranium oxide fuels, and materials testing reactors operating with aluminum matrix fuels. These highly productive nuclear technology developments at the Laboratory have resulted in a legacy of nuclear fuels and materials that require stabilization prior to their ultimate disposal. A primary concern with disposal of these materials is their potential release of radioactive constituents into the biosphere. One way to lessen the burden on a repository for used nuclear fuel and materials is to process them into waste forms that are more robust than the used fuel matrix itself. Such is an outcome of the electrometallurgical treatment process, which is based on molten salt dissolution of specific metallic fuels and could be extended to other used nuclear fuels.

The aim of this study was to examine molten salt dissolution techniques that could be used to address stabilization and disposition of select legacy nuclear fuels and materials at the Laboratory. Specifically, the scope of this study was limited to dissolution phenomena of nuclear research reactor fuel constituents in molten salt systems. Fuels and constituents in this study included (1) used nuclear oxide fuels, (2) aluminum matrix fuels, (3) bond sodium from metallic fuels, and (4) uranium metal and hydride to synthesize high-purity uranium trichloride for use in molten salt dissolution studies.

The dissolution of used nuclear oxide fuels in molten salt systems initially involved contacting various forms of nuclear oxide fuel in molten lithium chloride – potassium

chloride eutectic with 9 wt% uranium as the trichloride at 500°C. Alkali, alkaline earth, lanthanide, and transuranium constituents partitioned from the oxide fuels into the molten salt phase to varying extents with a wide range of 12 – 99%. Higher extents of fuel constituent dissolution were attributed to reducing conditions in the fuel matrix and preconditioning of the fuel. Subsequent experiments were performed in which reducing conditions in preconditioned oxide fuel were created via electrolytic and chemical-seeded means. Other parameters, including higher operating temperatures (500 to 800°C) and uranium trichloride concentrations (upwards of 19 wt% uranium as the trichloride), were investigated in these experiments, leading to fuel constituent dissolution above 90%.

Dissolution of an aluminum fuel matrix involved contacting and heating neodymium metal (as a surrogate for uranium metal) and aluminum metal (in foil and particulate form) initially with lithium and ammonium chloride. The aluminum metal forms reacted into volatile aluminum chloride, separating from the neodymium metal which simultaneously reacted to form neodymium chloride and fused with the lithium chloride. Experiments were repeated with lithium and ammonium bromide to assess the performance of a bromide system vis-à-vis a chloride system. Extents of aluminum removal ranged from 94.5 – 98.2% and 91.4 – 97.8% for the chloride and bromide systems, respectively.

Sodium metal was deactivated into molten salt systems via reaction with non-metal (ammonium) and metal (ferrous) chlorides. The reaction of molten sodium metal with metered ammonium chloride particulate proceeded without excursions, producing a pure colorless sodium chloride. The reaction of molten sodium with ferrous chloride yielded occasional excursions and salt fuming, producing a dark salt-metal mixture. These experiments identified a controlled technique to convert reactive and pyrophoric sodium

metal into a stable sodium chloride – a technique that could be applied in a remote-handled inert-atmosphere environment with sodium metal containing elevated levels of reactivity, such as bond sodium in used nuclear metallic fuels.

Uranium metal and uranium hydride were separately reacted with ammonium chloride in the presence of lithium chloride – potassium chloride eutectic to form a ternary mixture of uranium trichloride with the alkali-metal chlorides. Similar experiments were performed to synthesize a eutectic mixture of sodium chloride – uranium trichloride. Extensive characterization of the synthesized products was performed to assess their form and purity.

This collection of experimental studies highlights the safety and effectiveness of molten salts at dissolving select used nuclear research reactor fuel constituents under specific conditions. When applied to used fuels, the radioactive components in the molten salt systems may be further treated, as needed, into leach-resistant, robust waste forms for ultimate disposal in a federal repository.

Acknowledgements

As a newly minted B.S. graduate in Chemical Engineering, I emerged with a determination to focus on clean energy options for a career. Accordingly, I set my sights on a PhD program in hydrogen fuel cell technology. However, this PhD pursuit failed to materialize. Fortunately, Prof. Dee Barker, a nuclear scientist, had instructed me in the basics of nuclear engineering as an undergraduate and introduced me to what is now Idaho National Laboratory. This experience intrigued me and gave me confidence to branch out from my groundwork in chemical engineering and launch a career in nuclear energy. As a new employee of Bettis Atomic Power Laboratory, I received classroom instruction at the Naval Nuclear Power School and practical training at the Naval Reactors Facility. I am indebted to my supervisors and colleagues, including David Bright, Craig Olson, and Cliff Sing among many others, at the Naval Reactors Facility, who trained me in the safe operation and maintenance of a prototype naval nuclear power plant. After prototype operations at the Naval Reactors Facility ended, I jumped ship to Argonne National Laboratory – West, where the flagship reactor, Experimental Breeder Reactor – II, was still operating. I sincerely appreciated the support of my supervisor and senior colleagues, Bill Buschman, Bob Washburn, and John Krsul, who mentored me in the science and engineering of sodium coolant systems for liquid metal fast reactors. I was also profoundly influenced at Argonne by Dr. Pete Planchon, who encouraged and set me on a path to assist in the research and development of a treatment process for used nuclear oxide fuels in molten salt systems. This brought me into the company of Drs. Charles Till and Yoon Chang, the champions behind the Integral Fast Reactor program, and their highly skilled and talented team of scientists and engineers. Dr. Shelly Li was part of this team, and I sincerely appreciate her willingness to

mentor me in high-temperature electrochemistry. She has supported me through years of productive research and development work at the Laboratory. I sincerely appreciate the comradery and support over many years at Argonne National Laboratory and now Idaho National Laboratory of numerous capable supervisors, mentors, and long-time colleagues, including Ken Bateman, Bob Benedict, Dean Burt, Dan Cummings, Steven Frank, Guy Fredrickson, Jeff Giglio, Mike Goff, Karthick Gourishankar, Mike Holzemer, Karen Howden, Dawnette Hunter, Pat Kern, Ron King, Gavin Knighton, Shelly Li, Tim Malewitz, Bob Mariani, Ken Marsden, Michael Patterson, Supathorn Phongikaroon, Dave Sell, Michael Simpson, Prabhat Tripathy, Dee Vaden, Dale Wahlquist, Dennis Wahlquist, Ron Wallace, Leon Walters, Brian Westphal, Scot White, Mark Williamson, Jim Willit, Tae-Sic Yoo, and many others. While engaged in various research and development activities, I was honored by an invitation from Prof. Haiyan Zhao to pursue a PhD program in Chemical Engineering at the University of Idaho. I am indebted to her for taking a chance on a non-traditional student and for capably instructing and advising me through this PhD program. I value the instruction, friendship, and support of other University of Idaho professors and classmates throughout my graduate studies. I also sincerely appreciate committee members, Prof. Vivek Utgikar and Prof. Eric Aston, who have devoted their time and consideration toward my research along with Prof. Zhao and Dr. Li. Funding for the research in this study was facilitated primarily through the Laboratory Directed Research and Development program and a Nuclear Science User Facilities Rapid Turnaround Experiment award at Idaho National Laboratory under the U.S. Department of Energy, Office of Nuclear Energy, Idaho Operations Office contract DE-AC07-05ID14517.

Dedication

I dedicate this work to my family.

My loving parents, Gideon and Arlene, were educators and sacrificed their time and means for my brothers, David and Edward, and me to receive our initial college degrees. My dear children, Jace, Chad, Shauna, Paige, Lukas, and Breanne have all excelled in their own educational pursuits, which in turn inspired me to continue mine, albeit later in my career. My precious wife, Laura, has stood by my side throughout my doctorate program and without complaint has encouraged me to fulfill this important life goal.

I love and thank you all.

Table of Contents

List of Tables

List of Figures

Nomenclature

List of Abbreviations

AEC	Atomic Energy Commission
AGHCF	Alpha-Gamma Hot Cell Facility
AL	Analytical Laboratory
ANL	Argonne National Laboratory
ATR	Advanced Test Reactor
BR3	Belgium Reactor 3
BWR	Boiling water reactor
CAES	Center for Advanced Energy Studies
CANDU	Canada Deuterium Uranium
CE	Counter electrode
CNEA	Comision Nacional de Energia Atomica
DEOX	Decladding by Oxidation
DOE	Department of Energy
DU	Depleted uranium
EBR-I	Experimental Breeder Reactor – I
EBR-II	Experimental Breeder Reactor – II
EDS	Energy-dispersive X-ray spectroscopy

EELS	Electron energy loss spectroscopy
EIS	Environmental Impact Statement
EMT	Electrometallurgical Treatment
ETR	Engineering Test Reactor
EU	European Union
FASB	Fuel and Applied Science Building
FCF	Fuel Cycle Facility or Fuel Conditioning Facility
FCG	Fuel Cycle Glovebox
FFTF	Fast Flux Test Facility
GCR	Gas-cooled reactor
HEU	High-enriched uranium
HFDA	Hot Fuel Dissolution Apparatus
HFEF	Hot Fuel Examination Facility
ICP-MS	Inductively Coupled Plasma – Mass Spectroscopy
ICP-OES	Inductively Coupled Plasma – Optical Emission Spectroscopy
IFR	Integral Fast Reactor
IMCL	Irradiated Material Characterization Laboratory
INL	Idaho National Laboratory

LEU	Low-enriched uranium
LMR	Liquid metal reactor
MOX	Mixed uranium-plutonium oxide
MTHM	Metric tons of heavy metal
MTR	Materials test reactor
NRTS	National Reactor Testing Station
PHWR	Pressurized heavy-water reactor
PWR	Pressurized water reactor
RE	Reference electrode
STEM	Scanning transmission electron microscope
TRU	Transuranium or transuranic
USS	United States Ship
WCL	Water Chemistry Laboratory
WE	Working electrode
XRD	X-ray diffraction

List of Symbols

α	Alpha particle	--
γ	Gamma particle or gamma ray	--
ΔG_f	Gibbs free energy of formation	J mol^{-1}
ΔG_{Rx}	Gibbs free energy of reaction	J mol^{-1}
ΔG°	Gibbs free energy change at specified standard condition	J mol^{-1}
ΔH_f	Heat of formation	J mol^{-1}
ΔH_{Rx}	Heat of reaction	J mol^{-1}
μ_i	Chemical potential	J mol^{-1}
σ_γ	Gamma-yielding absorption cross section (barn = 10^{-28} m^2)	m^2
σ_a	Absorption cross section (barn = 10^{-28} m^2)	m^2
σ_f	Fission cross section (barn = 10^{-28} m^2)	m^2
a_i	Activity of species i	--
C_p	Heat capacity (constant pressure)	J K^{-1} kg^{-1}
C_v	Heat capacity (constant volume)	J K^{-1} kg^{-1}
E	Cell potential	J C^{-1}
E°	Cell potential at specified standard conditions	J C^{-1}

E_{cell}	Full-cell potential	J C^{-1}
$E°_{cell}$	Full-cell potential at specified standard conditions	J C^{-1}
E_{Ox}	Half-cell oxidation potential	J C^{-1}
$E°_{Ox}$	Half-cell oxidation potential at specified standard conditions	J C^{-1}
E_{Red}	Half-cell reduction potential	J C^{-1}
$E°_{Red}$	Half-cell reduction potential at specified standard conditions	J C^{-1}
F	Faraday's constant (96485 C per mole electron)	C mol^{-1}
G	Gibbs free energy	J mol^{-1}
H	Enthalpy	J mol^{-1}
I	Current	A
m	Mass	kg
M_i	Molecular weight of species i	kg
n	Neutron	--
n	Number of moles of electrons	mol
N_{AV}	Avogadro's number (6.022E23 mol^{-1})	mol^{-1}
N_i	Chemical component of i	mol
p	Proton	--
P	Pressure	Pa

q	Unit of charge (1.6E-19 C)	C
Q	Heat	J
Q	Charge	C
s_i	Stoichiometric coefficient of species i	--
S	Entropy	$J\ K^{-1}$
T	Temperature	K
U	Internal energy	J
V	Volume	m^3
W	Work (thermodynamic or mechanical)	J
W_{el}	Work (electrical)	J

1. Introduction

Since the dawn of the nuclear age in the mid-twentieth century, the peaceful use of nuclear energy has offered humanity a clean and plentiful source of electric power generation. Indeed, the world's first nuclear-generated electricity came from Experimental Breeder Reactor-I (EBR-I), a metal-fueled and liquid metal-cooled reactor, which began operations in 1951 at the National Reactor Testing Station (NRTS) near Arco, Idaho. Since then, various nuclear reactors ranging from small-scale research reactors to commercial-scale nuclear power plants have been designed, built, and operated throughout the world. As of July 2020, there were approximately 440 nuclear reactors operating throughout the world generating approximately 10% of the world's electric power, and another 50 reactors were under construction. [1] Within the U.S. there were 95 commercial nuclear power reactors with another 2 reactors under active construction as of May 2020. [2] For the past three decades nuclear power has generated and continues to generate about 20% of the electricity in the U.S. [3]

Many of the power-generating nuclear reactors operating today are based on technologies that were pioneered over a 70-year history at the NRTS, now Idaho National Laboratory (INL), where 52 nuclear reactors have operated. All but four have been decommissioned and those four remain in operation today. [4] This rich history in nuclear power generation development at INL has also left a legacy of nuclear fuels and materials that require stabilization prior to their ultimate disposal. ***The goal of this study was to examine molten salt dissolution techniques that could be used to address stabilization and disposition of select legacy nuclear fuels and materials at INL.*** The following introduces

these legacy fuels/materials and their origins within a context of nuclear power generating reactors.

Power-generating nuclear reactors have evolved over the past seven decades into a wide variety of types based on an array of different fuels, moderators, and coolants – the primary components of nuclear reactors. They can be broadly categorized into thermal and fast reactors – the former containing fuel, moderator, and coolant, while the latter contains only fuel and coolant. [5]

A moderator is used in a thermal nuclear reactor to slow down high energy (fast) neutrons generated from fission to thermal energies, where they are more easily absorbed by fissile nuclei (e.g., uranium-235) to sustain a controlled fission chain reaction. Consequently, thermal reactors may operate with uranium containing a natural abundance of uranium-235 (0.72 atom %) or higher concentrations – generally 3-5 atom % uranium-235 (low-enriched uranium or LEU) for commercial reactors or above 20 atom % uranium-235 (high-enriched uranium or HEU) for some research, test, and other specialty reactors. Moderators consist of solid and liquid media with low atomic numbers, typically at or below that of oxygen. Accordingly, water, heavy water, and graphite are common moderators in power generating nuclear reactors. [5]

Coolant is used to remove heat from fission in the core of a nuclear reactor and transfer it for use in power production. Common coolants in thermal reactors include various gases (e.g. helium or carbon dioxide), water, and heavy water – the latter two of which may also serve as moderators. Fast reactors may also be cooled by gases; however, they are generally cooled by liquid metal, typically liquid sodium. [5]

A controlled fission chain reaction in a power generating nuclear reactor is sustained by a complex matrix of its fuel and coolant (and moderator in a thermal reactor). In short, fission of a fissile actinide nucleus (e.g., uranium-235) produces two daughter nuclei (fission products) and two to three high energy (fast) neutrons, as illustrated in Figure 1.1. As they discharge from a fissioned atom, the neutrons primarily experience one of three things – (1) elastic and inelastic scattering with nuclei in a reactor, which slow down the neutrons eventually toward thermal energies, (2) absorption in nuclei inside the reactor, or (3) leakage from the reactor. By design, neutrons are predominantly scattered by coolants and moderators, and some are allowed to leak where they are absorbed by media outside the reactor. Those neutrons that remain in the reactor are by design primarily absorbed into nuclei in the fuel matrix. Only one of the neutrons from a preceding fission is needed for subsequent absorption and fission within a fissile nucleus in the reactor to sustain a chain reaction. Absorption of neutrons into fertile nuclei, e.g., uranium-238 or thorium-232, in a reactor form unstable nuclei that subsequently decay to other fissile nuclei, e.g., plutonium-239 or uranium-233, respectively. Uranium-235 is the only fissile nuclide that is found in nature and is, consequently, the primary constituent in new nuclear fuel. [5]

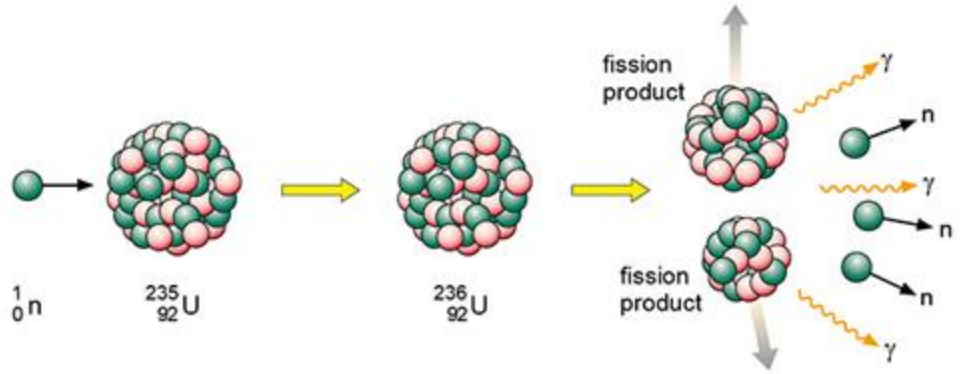

Figure 1.1. Fission of uranium-235.

The primary forms of fuel in fission reactors are oxide and metal. Other forms include (1) non-oxide ceramic fuels, such as uranium nitride, uranium silicide, and uranium carbide, and (2) fluid fuels, such as molten salt or aqueous solutions. Oxide fuels in the form of uranium oxide (UO_2) and mixed uranium-plutonium oxide (MOX) fuels are the predominant forms of fuel in commercial reactors throughout the world, owing to their high thermodynamic stabilities and high melting points, compared to their respective metal fuel counterparts. Typical commercial oxide fuels are formed from dense pellets of uranium oxide or MOX stacked inside a tight-fitting sealed tube (i.e., cladding) for good thermal contact between the fuel pellets and cladding (typically Zircaloy for water cooled/moderated reactors). In contrast to oxide fuels, metal fuels have higher thermal conductivities but lower melting points. Metal fuels are typically alloys of uranium and other metals, including plutonium (and other minor actinides), zirconium, aluminum, or molybdenum. A metal fuel is bonded directly to its cladding or indirectly through a thermal bond, such as sodium metal. Typical metal fuel cladding materials include aluminum for uranium-aluminum alloy fuels in water cooled/moderated reactors and steel in liquid metal cooled reactors. [6-7]

While nuclear reactors are largely defined by their fuel, moderator, and coolant, essentially all power-generating reactors can be classified into six different types – pressurized water reactors (PWRs), boiling water reactors (BWRs), pressurized heavy-water reactors (PHWRs), liquid metal reactors (LMRs), gas-cooled reactors (GCRs), and light-water graphite reactors (LWGRs). Of these six, PWRs and BWRs, collectively referred to as light-water reactors (LWRs), dominate in the commercial generation of electrical energy. GCRs and LWGRs operate primarily in the United Kingdom and countries of the former Union of Soviet Socialist Republics, respectively, both of which are being phased out. (Note: The 1986 Chernobyl disaster involved a LWGR.) PHWRs are primarily associated with Canada Deuterium Uranium (CANDU) reactors, which operate with natural uranium and consequently necessitate a heavy water moderator/coolant. While PHWRs are used in several countries, they represent a small fraction of commercial electric power generation. Despite a long development history, LMRs have so far had little bearing on commercial electric power generation. However, as fundamental forms of breeder reactors, LMRs offer perhaps the most potential for sustained future nuclear power generation. [7-8] A summary of power-generating reactor types, including fuel, moderator, and coolant, is shown in Table 1.1.

Table 1.1. Summary of power-generating reactors [8]

Reactor Type	**Fuel**	**Moderator**	**Coolant**
Pressurized Water Reactor (PWR)	Enriched uranium	Light water	Light water
Boiling Water Reactor (BWR)	Enriched uranium	Light water	Light water
Pressurized Heavy Water Reactor (PHWR)	Natural or slightly enriched uranium	Heavy water	Heavy water
Light Water Graphite Reactor (LWGR)	Enriched uranium	Graphite	Light water
Gas-Cooled Reactor (GCR)	Natural or enriched uranium	Graphite	Carbon dioxide
Liquid-Metal Reactor (LMR)	Enriched uranium or plutonium	N/A	Sodium

Development of nuclear reactors for peaceful purposes in the U.S. commenced with the Atomic Energy Act of 1946, which established the Atomic Energy Commission (AEC) to foster and control the development of atomic science and technology. [9] The AEC (the function of which was absorbed by the U.S. Department of Energy in 1977) selected the high desert plain near Arco, Idaho, as a NRTS, which later became INL. In 1948, construction began on several new reactor facilities at NRTS, including EBR-I (an LMR), a prototype PWR for submarine propulsion (known as S1W), and a high-flux materials test reactor (MTR), each of which evolved into enduring nuclear reactor technologies at NRTS and INL.

These reactor technologies and their bearing on the work in this study are discussed further in turn.

Overview and Relevance of Liquid-Metal Reactors at INL

EBR-I operated from 1951 to 1963. It was fueled initially by HEU metal and later by plutonium metal. It was cooled by a eutectic mixture of sodium and potassium metal (i.e., NaK). As a fast reactor, it had no moderator. Within the first two years of operation, EBR-I proved the concept of breeding by producing more fissile material (plutonium-239 from uranium-238) than it consumed. In 1962, it became the first reactor to operate with a plutonium metal-fueled core. [7]

The successes of EBR-I paved the way for the next step in the scaleup of the U.S. breeder reactor, Experimental Breeder Reactor-II (EBR-II). EBR-II was a metal-fueled sodium-cooled fast reactor that operated from 1964 to 1994 at INL. The fuel that made up the core of the reactor (i.e., driver fuel) and drove the power production in EBR-II consisted of HEU metal alloys. The driver fuel was enveloped radially and axially in the reactor by depleted uranium metal blanket fuel, where breeding occurred. The sodium coolant consisted of an 87,000-gallon pool of primary sodium, in which the reactor was immersed, and 13,000 gallons of secondary sodium coolant, which transferred heat from the primary system to super-heated steam generators. The design output of EBR-II was 60 MW-thermal and 19 MW-electric. EBR-II operated with an adjacent Fuel Cycle Facility (FCF), as pictured in Figure 1.2, where irradiated fuel from EBR-II was treated remotely via a melt refining process and returned to the reactor through the period of 1964 to 1969. [10] Between 1970 and 1983, EBR-II functioned primarily as a fuel irradiation facility, before an Integral Fast Reactor (IFR) initiative drove EBR-II operations from 1984 to its closure in 1994.

During the 30-year operation of EBR-II, the driver fuel evolved into assemblies of uranium metal alloy pins that were loaded into steel cladding tubes which were pre-loaded with sodium metal. The tubes were heated to settle the fuel pins within the liquid sodium to the bottom of the cladding tube. The top open end of the cladding was then evacuated and sealed to form a driver fuel element, where the fuel pin was thermally bonded to its cladding by the pre-loaded sodium metal. EBR-II blanket fuel elements, although larger in diameter and length, were similarly constructed with a thermal sodium bond. [10-11]

Figure 1.2. Experimental Breeder Reactor-II (center) with adjacent power plant (left) and Fuel Cycle Facility (right, which was later named the Fuel Conditioning Facility).

As part of the IFR initiative, an electrochemical pyroprocess was developed to recycle used EBR-II driver and blanket fuel. However, the IFR initiative was terminated before any used fuel was recycled by the pyroprocessing route. Yet the need to disposition used EBR-II fuel remained, primarily due to the reactive nature of its bond sodium which

precluded its direct disposal in a geological repository. Consequently, existing infrastructure within FCF was modified into an electrometallurgical treatment (EMT) process that could treat sodium-bonded fuel not only from EBR-II, but also from the Fermi-1 reactor and the Fast Flux Test Facility (FFTF). The EMT process deploys electrorefining to dissolve used sodium-bonded fuel into a molten salt system in which some fission products accumulate and from which refined uranium metal and undissolved cladding and fission products are separately removed. The recovered uranium metal is melted to remove adhering salt and blended with depleted uranium, as necessary, to produce low-enriched or depleted uranium ingots. After a three-year demonstration of the EMT process with used EBR-II fuel, an Environmental Impact Statement, and an independent review by the National Research Council, the U.S. Department of Energy (DOE) issued a Record of Decision identifying EMT as the preferred alternative for treatment of EBR-II and FFTF sodium-bonded spent nuclear fuel. [12]

While the EMT process deactivates the bulk of the bond sodium as part of the fuel treatment, a substantial fraction of the sodium remains as residue in untreated sections of a driver fuel element above the fueled region, which is commonly referred to as plenum sodium. As an alternative to EMT, sodium-bonded blanket elements may be subjected to elevated temperature and reduced pressure to distill away the bond sodium from the fuel and cladding. In either case, sodium metal is produced which contains significant concentrations of radioactive fission products, primarily cesium. Consequently, an appropriate disposition pathway is needed for deactivation and disposition of this reactive fuel constituent. ***Thus, one objective of this study was to investigate deactivation of bond sodium via dissolution in a molten salt system.***

Overview and Relevance of Pressurized Water Reactor Development at INL

The design, fabrication, and operation of S1W, a prototype of the world's first nuclear powered naval vessel, was momentous for the development of commercial PWRs. [8] Operation of S1W began in 1953, and a year later the United States Ship (USS) Nautilus was launched. [13] The USS Nautilus and S1W operated until 1980 and 1989, respectively. The successful operation of S1W and the USS Nautilus cannot be understated, as their demonstration of safety and reliability of nuclear power directly influenced the commercial development of PWR technology. Indeed, Westinghouse, which designed and built the S1W and USS Nautilus PWRs, also built the PWR for Shippingport Atomic Power Station – the first commercial nuclear power plant in the U.S., which began operations in 1957. [8] Shippingport pioneered the use of uranium dioxide fuel in a water-cooled reactor, laying the foundation for other commercial PWRs to follow. [8] A typical uranium oxide fuel pellet within a commercial fuel assembly is shown in Figure 1.3. A notable variation of the PWR is the BWR, which was advanced by General Electric. As of May 2020, the 95 commercial nuclear power reactors operating in the U.S. were comprised of LWRs – two thirds of which were PWRs and the balance were BWRs. [14]

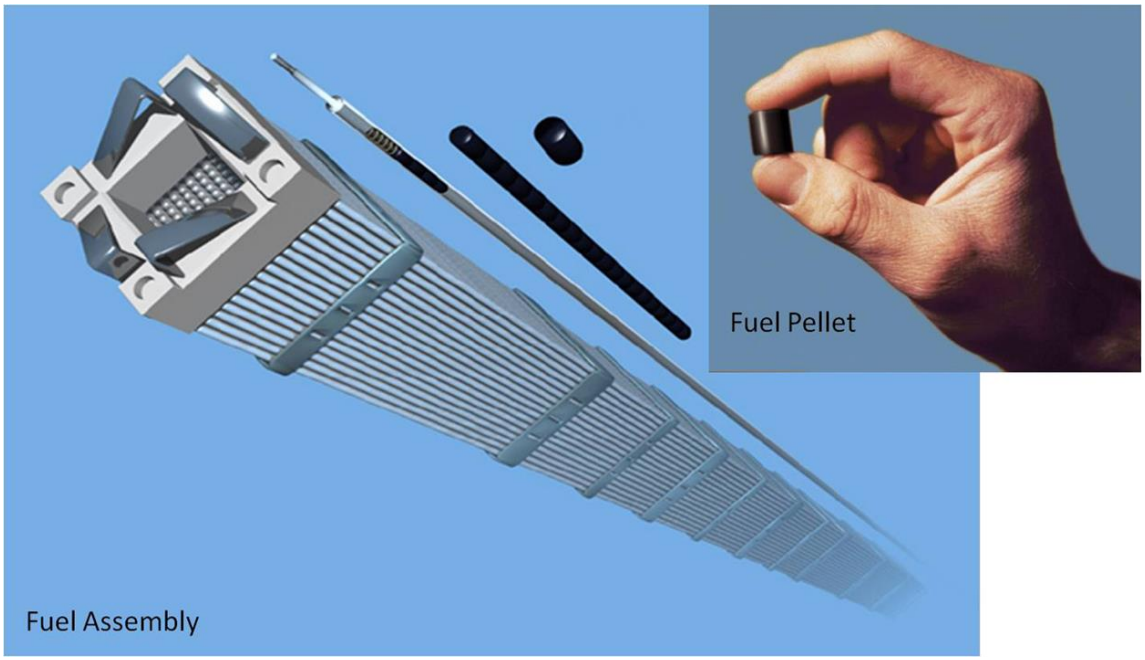

Figure 1.3. Uranium oxide fuel pellet within a commercial fuel assembly.

As a result of the deployment of commercial LWRs in the U.S. over the last 60 years, a significant mass of used nuclear oxide fuel has been generated. Indeed, over 80,000 metric tons of heavy metal (MTHM) in used commercial nuclear fuel has accumulated in the U.S. and continues to accumulate at a rate of 2000 MTHM per year. [15] Per the Nuclear Water Policy Act of 1982, a comprehensive national program for the safe and permanent disposal of highly radioactive wastes (including used nuclear fuel), the U.S. DOE was given the responsibility to site, construct, and operate a repository for these materials. [16] Yucca Mountain Nuclear Waste Repository has been extensively evaluated as a possible federal repository for used nuclear fuel since 1987. However, neither Yucca Mountain nor a suitable alternative has yet to become operational. Consequently, used commercial nuclear fuel continues to stockpile at power stations across the U.S., and some of that commercial fuel has accumulated at INL over the years for various research purposes.

A primary concern with a federal repository is the stability of used nuclear fuel packages that would be placed in it and the potential release of radioactive constituents into the biosphere. One way to lessen the burden on a federal repository for used nuclear fuel is to process it into waste forms that are more robust than the used fuel itself. Such is an outcome of the EMT process for used nuclear metal fuel, which could also be extended to used nuclear oxide fuels. In fact, the U.S. DOE Record of Decision for Treatment and Management of Sodium-Bonded Spent Nuclear Fuel states that modifications to the process could be used for the treatment of oxide fuels. [12] ***Thus, a primary objective of this study was to investigate a novel variation of the EMT process for used nuclear oxide fuel using a molten salt dissolution technique.***

An essential compound in the EMT process and in a novel extension of this process to oxide fuel dissolution in molten salt systems is uranium trichloride. Because uranium is a radioactive nuclear material, compounds of it are not readily available from commercial chemical suppliers. Thus, the uranium trichloride used in the EMT process has been and continues to be synthesized in DOE laboratories. To accommodate a study of used nuclear oxide fuel dissolution in molten salt systems, ***an accompanying objective of this study was to investigate and demonstrate techniques to synthesize high-purity uranium trichloride in forms needed for this study.***

Overview and Relevance of Materials Testing Reactors at INL

A series of three reactors specific to materials testing was developed and operated at the NRTS and INL over its 70-year history, including: 1) The Materials Testing Reactor (MTR), a 40-MW thermal reactor which operated from 1952 to 1970; 2) The Engineering Test Reactor (ETR), a 175-MW thermal reactor which operated from 1957 to 1981; and 3)

The Advanced Test Reactor (ATR), which began operations in 1967 and is one of four nuclear reactors which continues to operate at INL. (Note: The other three operating nuclear reactors at INL are the Advanced Test Reactor Critical at the Test Reactor Area, the Transient Test Reactor, and the Neutron Radiography Reactor – the latter two of which are located at the Materials and Fuels Complex.) The primary purpose of the test reactors has been to provide a neutron generating environment in which other nuclear materials, including fuels, coolants, and moderators, could be tested before use in a conventional or other power generating reactor. [17-20]

Each of the three test reactors were designed as pressurized light-water thermal reactors, fueled with a high-enriched uranium-aluminum alloy in an aluminum clad. [21] As materials test reactors, each was configured with beryllium reflectors, which serve to elevate the neutron flux levels in the reactor to 10 to 100 times that of a conventional thermal reactor. Accordingly, nuclear materials in a test reactor experience the same neutron exposure in a matter of days to weeks that they might experience in a commercial or other power generating reactor in months to a year. This capability is invaluable in developing and demonstrating new nuclear materials for advancing power generating nuclear reactors. [17-19]

At 250 MW-thermal, ATR is the world's most powerful research reactor and is the flagship irradiation facility in the U.S. It simultaneously supports a wide range of experiments for multiple customers, including materials and fuels testing for the U.S. Navy, medical isotopes for diagnosing and treating diseases, and materials and nuclear fuels testing for government and university research reactors and the commercial nuclear power industry.

[22] The ATR is known for its unique serpentine fuel arrangement, as shown in Figure 1.4, which affords unique experimental versatility and reactor control. [23]

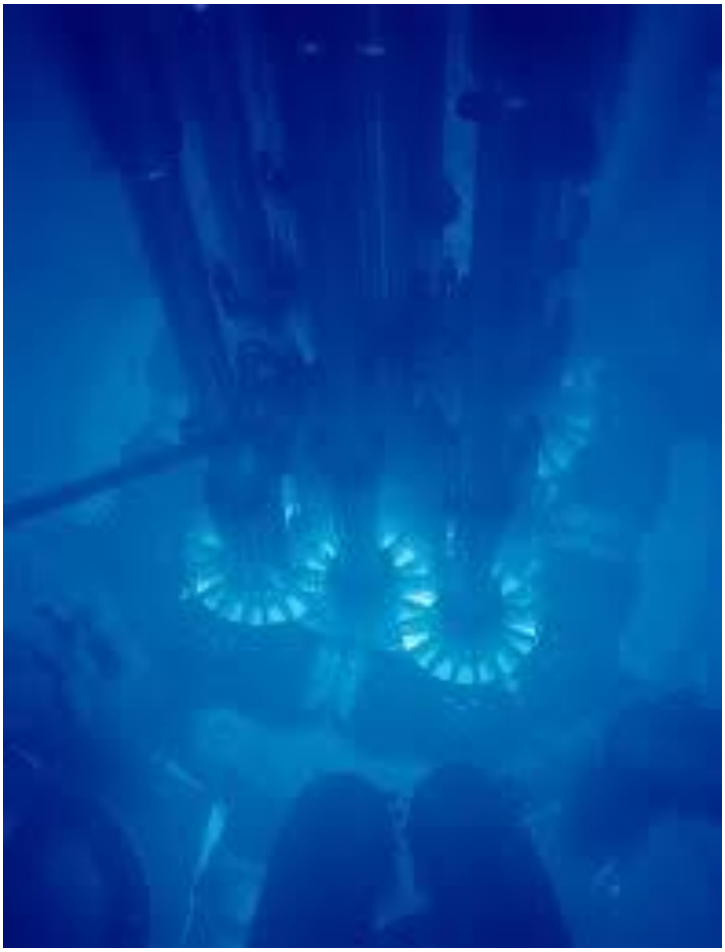

Figure 1.4. Core of Advanced Test Reactor with a characteristic blue Cherenkov radiation.

Used fuel from the materials testing reactors at INL has accumulated over the years at INL. An EMT process may be applied to treatment of this used metal fuel with appropriate headend conditioning. ***Thus, the final objective of this study was to investigate novel techniques involving molten salt dissolution of used aluminum-based test reactor fuels as a headend step to EMT.***

In summary, the three overarching nuclear technologies that were developed and advanced over the 70-year history of INL include the 1) LMR and accompanying EMT process, 2) the PWR with uranium oxide fuel, and 3) materials testing reactors. What remains of the LMR development activities at INL is an ongoing EMT process to condition the accumulated used EBR-II fuel and recover its HEU for subsequent down blending and disposition. The legacy of the pressurized water reactor and uranium oxide fuel development at INL is the commercial nuclear power industry that stemmed from it, as well as a concomitant accumulation of various used nuclear oxide fuels at the INL site. Nuclear materials testing will continue well into the future with the ATR, yielding used nuclear fuel that continues to accumulate at the INL.

The primary aim of this study was an extension of a proven EMT process to stabilize other legacy fuels at INL, namely used oxide fuels and used aluminum-based test reactor fuels, which involved dissolution of these fuels into molten salt systems. Related studies included synthesis of the compounds needed to support these dissolution techniques and dissolution of remnant bond sodium resulting from the EMT process. *Nuclear research reactor* is used broadly in this study to include reactors that are not commercialized, e.g., test, experimental, and demonstration reactors. ***In summary, the scope of this study was limited to dissolution phenomena of nuclear research reactor fuel constituents in molten salt systems with the following foci.***

1. ***Dissolution of used nuclear oxide fuels in molten salt systems.***
2. ***Dissolution of aluminum matrix fuels in molten salt systems.***
3. ***Deactivation of sodium metal via dissolution in a molten salt system.***

4. Synthesis of high-purity uranium trichloride for use in molten salt dissolution studies.

2. Background

Dissolution of nuclear research reactor fuel constituents in molten salt systems is based on a fundamental understanding of used nuclear fuel characteristics, the thermodynamics that govern the thermostabilities of fuel constituents, and associated electrochemistry within molten salt environments. The following provides a brief background into used metal and oxide nuclear fuels from thermal and fast reactors along with thermodynamic and electrochemical properties that apply to dissolution of these fuels in molten halide salt systems. A fundamental understanding of used nuclear fuel characteristics and their associated thermodynamics and electrochemistry in molten salt systems paves the way for additional background into the EMT process. Extension of the EMT process to specific legacy fuels and related investigations, i.e., the primary foci of this study, follows.

2.1 Used Nuclear Fuel Characteristics

When neutrons collide with nuclei, they interact in one of two ways. They either *scatter* (which is the primary interaction with coolants and moderators in a nuclear reactor) or they are *absorbed* into nuclei (which is the primary interaction with fuel in a nuclear reactor). The primary interactions of neutrons that are absorbed into nuclei include 1) radiative capture, 2) charged-particle reactions, 3) neutron-producing reactions, and 4) fission. In radiative capture a neutron (n) is absorbed into a nucleus and one or more gamma (γ) rays are released. This interaction is denoted as (n, γ). In charged-particle reactions a neutron is absorbed into a nucleus and one or more charged particles, such as alpha (α) or proton (p) particles are released. These interactions are denoted as (n, α) and (n, p), respectively. In neutron-producing reactions a neutron (typically a higher energy neutron) is absorbed into a nucleus and one or more neutrons are released, denoted as (n, n) or (n, 2n) type interactions.

When neutrons are absorbed into certain nuclei (particularly *fissile* and *fissionable* actinides) the resulting nuclei can fission, or split apart, releasing fission products, neutrons, gamma rays, and other particles. [5]

Fissile nuclei are those that lead to fission following the absorption of a neutron at essentially zero energy (referred to as thermal neutrons or those with an ambient thermal energy of 0.0253 eV in accordance with a Maxwellian distribution function). The primary fissile nuclei include uranium-233, uranium-235, plutonium-239, and plutonium-241. *Fissionable* nuclei are those that fission when struck by a neutron of sufficiently high energy to overcome the binding energy of the newly formed nucleus. Examples of fissionable nuclei are uranium-238 and thorium-232. [5]

When neutrons interact with fissile or fissionable nuclei, they are primarily absorbed as the incidents of scattering are relatively low. The probability of a neutron being absorbed by a fissile or fissionable nucleus is defined by an effective cross-sectional area (in units of barns or 10^{-28} m^2) of that nucleus within a neutron field. The probability of a neutron being absorbed by a fissile or fissionable nucleus that leads to fission is similarly defined by an effective cross-sectional area, which is smaller than the absorption cross section. Absorption cross-sections (σ_a) and fission cross-sections (σ_f) are strong functions of neutron energy. Absorption and fission cross-section values for thermal neutron interactions can be found in standard charts of the nuclides, a short list of which is compiled in Table 2.1.

Table 2.1. Thermal absorption and fission cross-sections of select fissile and fissionable nuclei. [24]

Nuclide	**σ_a (barns) = $\sigma_\gamma + \sigma_f$**	**σ_f (barns)**
Thorium-232	7.34	<1E-6
Uranium-233	577	531
Uranium-235	683	585
Uranium-238	2.68	~5E-6
Plutonium-239	1021	750
Plutonium-241	~1371	1010

The ratio of fission to absorption cross-sections from Table 2.1 identifies the fraction of absorbed thermal neutrons in these nuclei that lead to fission. For example, the fraction of absorbed thermal neutrons that lead to fission of uranium-235 is 585/683, or 85.7%, whereas that for plutonium-239 is 73.5%. Conversely, absorbed thermal neutrons in nuclei that do not fission result in the formation of heavier nuclei, e.g., uranium-235 (n, γ) uranium-236 or plutonium-239 (n, γ) plutonium-240. The data in Table 2.1 also illustrate how fissionable nuclei transform into fissile nuclei. For example, uranium-238 can absorb a neutron to form uranium-239 which subsequently decays, releasing a beta-particle over a 23-minute half-life to form neptunium-239 which in turn beta decays over a 2.4-day half-life to form fissile plutonium-239. This transformation of non-fissile uranium-238 to a fissile plutonium-239, which is a form of breeding, leads to the designation of uranium-238 as a *fertile* nuclide. These examples illustrate how absorption of thermal neutrons in fissile and fertile nuclei yield a complex accumulation of heavier nuclei, some of which participate in subsequent fission. In short, thermal reactors generally result in a net accumulation of transuranium

(TRU) nuclei, or those nuclei with a higher atomic number than uranium. Some TRU elements are referred to as *minor actinides* or those nuclei that are not forms of plutonium, including neptunium, americium, and curium. All heavy nuclei (i.e., actinides) are unstable (i.e., radioactive), most of which have a long half-life of predominantly alpha decay.

In fast reactors, absorption and fission cross-sections of fissile and fissionable nuclei are generally substantially lower than those in a thermal reactor and vary over a broad range of neutron energies. Consequently, higher concentrations of fissile nuclei (e.g., HEU) are necessary in fast reactors. However, fast reactors yield lower concentrations of minor actinides than those in thermal reactors, owing to higher fission cross sections of minor actinides in a fast neutron spectrum.

A summary composition of, and reaction pathways for, actinides in a typical used uranium oxide (UO_2) fuel from a thermal reactor is shown in Figure 2.1. The flowchart in Figure 2.1 illustrates how an original UO_2 fuel enriched in uranium-235 to 4% was subjected to a nominal 45,000 MWd/t burnup, resulting in a used fuel composition of 5% fission products (60% of which originated from uranium-235 fission and 40% of which originated from plutonium-239 fission born from uranium-238), 1% plutonium isotopes, 1% uranium-235, and 93% uranium-238.

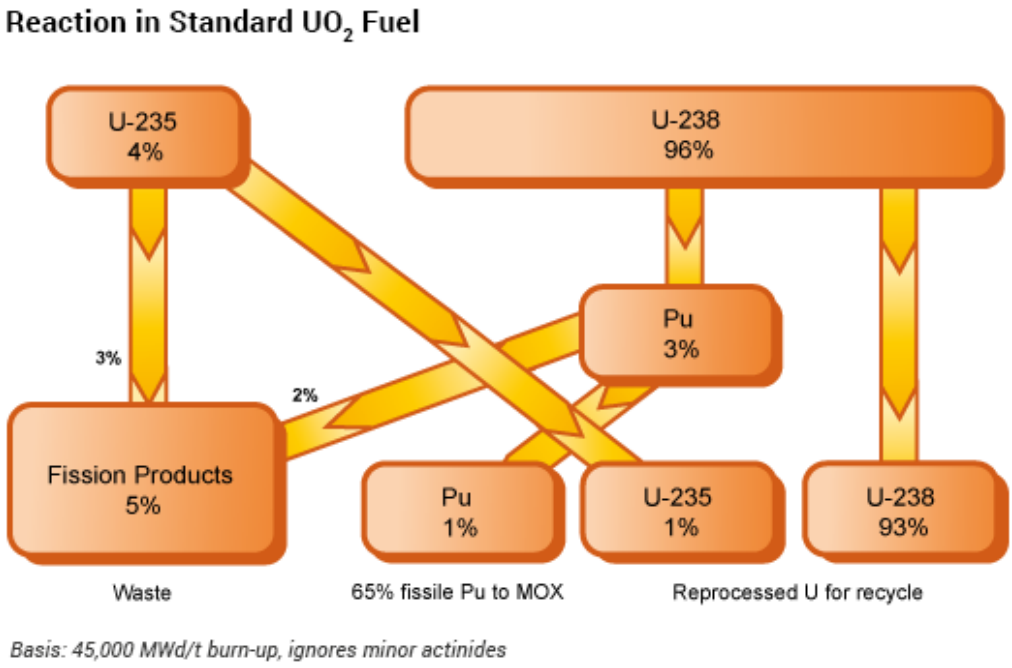

Figure 2.1. Flowsheet of reactions in standard UO_2 fuel. [25]

The fission of heavy nuclei in used nuclear fuel does not result in the same similarly massed products every time; rather, it forms a broad spectrum of fission product elements and isotopes with an abnormal distribution of atomic mass. The distribution of fission products is defined by *fission product yields*, which are the fraction of fission fragments produced by atomic mass number. The fission product yields are also listed on a standard chart of the nuclides. [24] The fission product yields for thermal and fast fission of uranium-235 are shown in Figure 2.2. A pseudo axis of symmetry in Figure 2.2 at an atomic mass of 116 is consistent with the fission of uranium-235, an accompany release of three neutrons, and halving the remaining atomic mass of 232. The two fission yield peaks in Figure 2.2 are centered primarily around atomic mass 95 (including stable and unstable isotopes of zirconium, niobium, and molybdenum) and 137 (including stable and unstable isotopes of cesium and barium), which sum to an atomic mass of 232. The primary difference in fission

product yields between thermal and fast fission is a relatively flatter distribution of atomic masses between the two peaks for fast fission, as illustrated in Figure 2.2.

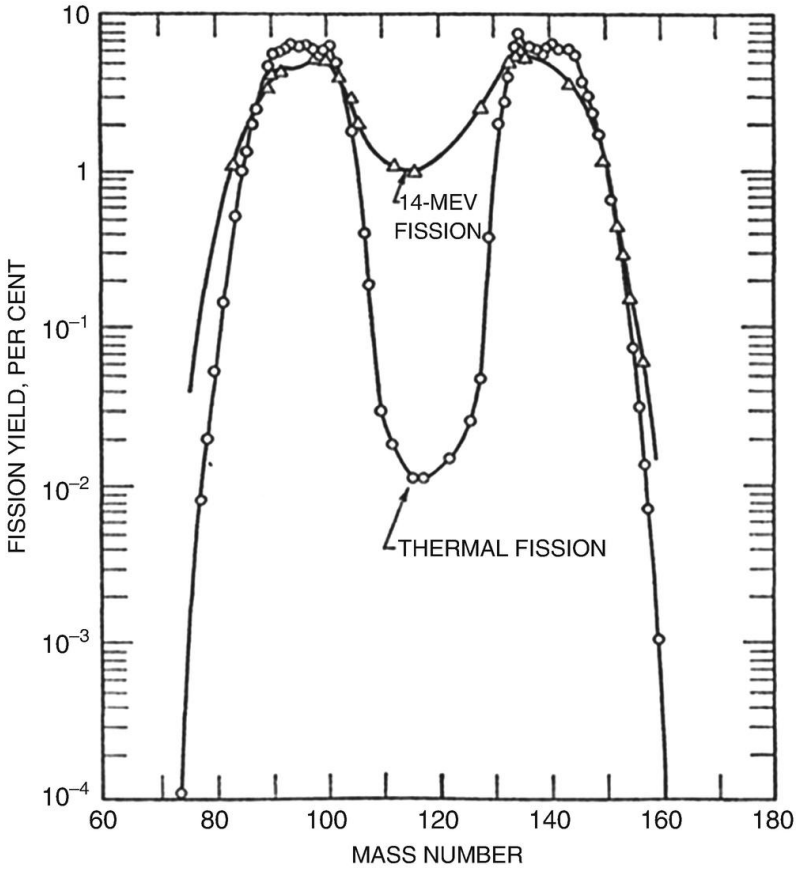

Figure 2.2. Fission product yield for thermal and fast fission of uranium-235. [26]

When fission products are formed, they are neutron rich, owing to the higher requisite neutron to proton ratio in heavy fissile nuclei. Consequently, fission products decay primarily by beta decay, where a neutron in an unstable nucleus of a fission product transforms into a proton and releases an electron (a negative β-particle for charge balance) often accompanied by a gamma ray. Thus, hundreds of unstable fission product isotopes in used fuel undergo radioactive decay, each with its own characteristic half-life and decay radiation. Furthermore, fission products are born in different phases, including gas, solid,

metallic, or oxide, which phases can also change through radioactive decay. [5] A typical composition of used nuclear oxide fuel from a thermal reactor is shown in Figure 2.3, which is limited to the most prevalent and consequential fission product isotopes.

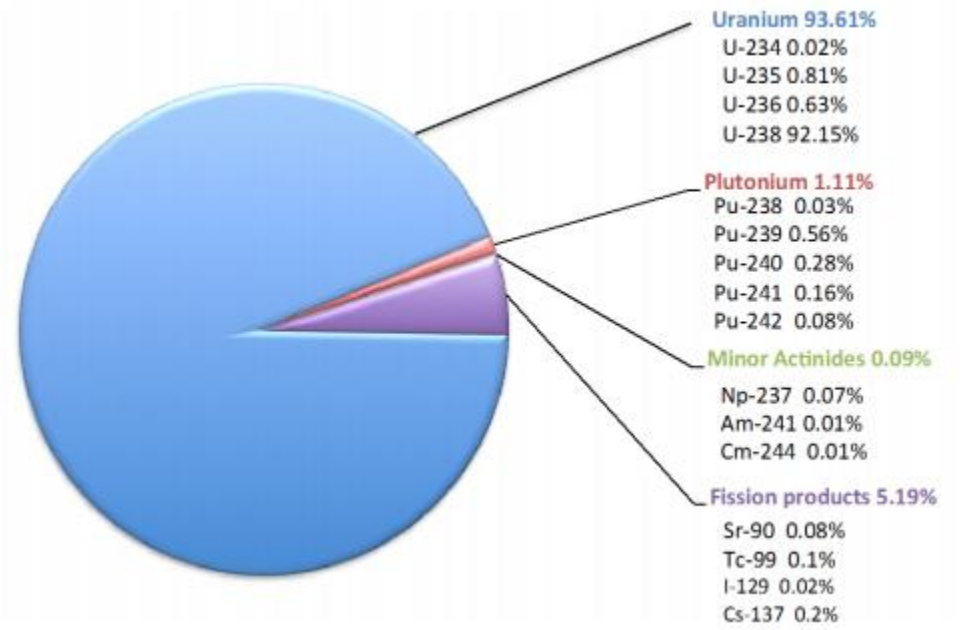

Figure 2.3. Composition of used uranium oxide fuel on a metals basis with initial uranium-235 enrichment of 4.5% after 45,000 MWd/t burnup. [27]

Fission of oxide or metal fuel results in the degradation of the fuel matrix, principally due to the formation of fission products and associated pressure exerted particularly by fission product gases. This leads to cracking and core hollowing of oxide fuels, and perforation followed by sodium intercalation in sodium-bonded metal fuels. Migration of fission products occurs in both oxide and metal fuels to varying degrees with some fission products concentrating in grain boundaries, others concentrating on the inner cladding wall, while some collect in voids and the plenum regions above a fuel column. In oxide fuels, essentially all the oxygen liberated by the fission of UO_2 is combined with fission products, forming complex oxide precipitates, e.g., $(Ba_{1-a-b}Sr_aCs_b)(U, Pu, Zr, Mo)O_3$, or oxides in solid

solution with the fuel matrix. [28] In short, a typical used nuclear fuel is a complex mixture of uranium isotopes, TRU isotopes, and fission products, the composition of which changes over time from radioactive decay. The decay heat associated with the radioactive decay of used fuel constituents over time is illustrated in Figure 2.4. The decay heat in used nuclear fuel, which correlates to the radiotoxicity of the used fuel constituents, underscores the need to stabilize these constituents prior to disposition of a used fuel in a repository to preclude their release into the biosphere. Thus, a primary aim of this study was to investigate techniques that would stabilize select used nuclear fuel constituents and facilitate an environmentally responsible disposition of these materials.

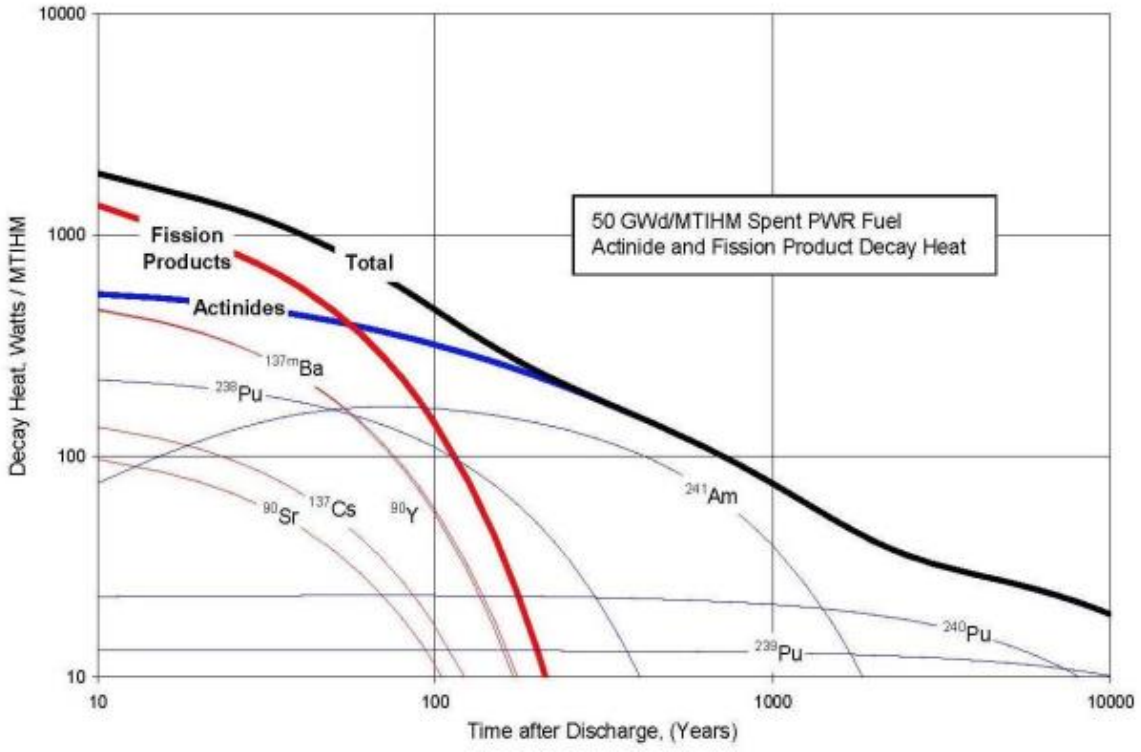

Figure 2.4. Decay heat generated by used thermal reactor fuel after 50,000 MWd/t burnup. [29]

2.2 Thermodynamics and Associated Electrochemistry

Thermodynamics is a broad scientific field devoted to the relationships between heat and other forms of energy, including mechanical, electrical, and chemical. For the purposes of this study a brief overview of governing thermodynamic relationships between heat, electrical, and chemical forms of energy is given.

The first law of thermodynamics states that the change in internal energy, ΔU, of a system is equal to the energy gained as heat, Q, less the thermodynamic work, W, done by the system on the surroundings, or an energy balance as defined below.

$$\Delta U = Q - W \qquad (2.1)$$

Internal energy is an extensive property that is measured by changes in its extensive variables, including entropy (S), volume (V), and chemical components (N_i) along with intensive variables, including temperature (T), pressure (P) and chemical potential (μ_i), as follows.

$$\Delta U = T\,\Delta S - P\,\Delta V + \sum \mu_i\,\Delta N_i \qquad (2.2)$$

Heat is typically defined in terms of temperature, mass (m), and heat capacities (C_p or C_v), as follows.

$$Q = m\,C_p\,\Delta T \quad \text{for constant pressure systems} \qquad (2.3)$$

$$Q = m\,C_v\,\Delta T \quad \text{for constant volume systems} \qquad (2.4)$$

Work (i.e., mechanical work) is often defined in terms of pressure and volume, as follows. [30]

$$W = P\,\Delta V \quad (2.5)$$

$$W = V\,\Delta P \quad (2.6)$$

Other thermodynamic properties, including enthalpy (H) and Gibbs free energy (G), are defined for relating thermodynamic variables. Specifically, enthalpy defines the total heat content of a system, which is the sum of the internal energy and the product of pressure and volume, as follows.

$$H = U + PV \quad (2.7)$$

The enthalpy of all elements is zero as a reference state, and the change in enthalpy (ΔH), a measurable property, has a positive value for *endothermic* reactions and a negative value for *exothermic* reactions. Enthalpy changes are useful in defining the heats of formation (ΔH_f) of compounds, from which the heats of reaction (ΔH_{Rx}) may be determined, as follows. [30-31]

$$\Delta H_{Rx} = \sum \Delta H_f \text{ (products)} - \Delta H_f \text{ (reactants)} \quad (2.8)$$

Gibbs free energy (G) is used to calculate the maximum reversible work that may be performed by a thermodynamic system at a constant temperature and pressure. Gibbs free energy is defined as follows.

$$G = H - TS \quad (2.9)$$

Like enthalpy, Gibbs free energy of all elements is zero as a reference state, and the change in Gibbs free energy (ΔG) has a negative value for *spontaneous* (or favored) reactions and a positive value for *non-spontaneous* (or non-favored) reactions. Gibbs free energy is also minimized when a system reaches chemical equilibrium. Like heats of reaction, Gibbs free

energy changes of reactions (ΔG_{Rx}) may be determined from Gibbs free energies of formation (ΔG_f), as follows. [30, 32]

$$\Delta G_{Rx} = \sum \Delta G_f \text{ (products)} - \Delta G_f \text{ (reactants)} \quad (2.10)$$

Regarding electrochemistry, the maximum reversible work as defined by Gibbs free energy includes electrical work (W_{el}). Accordingly, the change in Gibbs free energy is equal to electrical work, as shown below where work done by a system on the surroundings is positive.

$$\Delta G = -W_{el} \quad (2.11)$$

The electrical work is also defined as the product of an electrochemical cell potential (E with units of J/C or V), the number of moles of electrons in a full electrochemical reaction (n), and Faraday's constant (F with units of C per mole of electrons), as shown below.

$$W_{el} = nFE \quad (2.12)$$

Thus, the electrochemical cell potential can be determined from the change in Gibbs free energy as follows. [32]

$$\Delta G = -nFE \quad (2.13)$$

Furthermore, a change in Gibbs free energy can be related to a Gibbs free energy change at a specified standard condition ($\Delta G°$) and corrected for the activities of the species (a_i) involved in a full electrochemical reaction with stoichiometric coefficients (s_i), as shown below.

$$\Delta G = \Delta G° + RT \ln \prod a^{si}_i \quad (2.14)$$

Using the electrochemical work relation to Gibbs free energy (Eq. 2.13) leads to the classical Nernst equation, as shown below.

$$E = E° - RT/nF \ln \prod a^{si}_i \quad (2.15)$$

The Nernst equation applies to half-cell (denoted as E_{Red}, E_{Ox}, $E°_{Red}$, or $E°_{Ox}$) as well as full-cell (E_{cell} or $E°_{cell}$) reactions. [32]

The values for enthalpies, entropies, heat capacities, and Gibbs free energies of compounds can be found in standard thermodynamic tables. For this study, a commercial database [33] was used exclusively to determine heats of formation and reaction, Gibbs free energies of formation and reaction, and electrochemical cell potentials per the foregoing equations. Accordingly, the thermodynamic stabilities (listed top down from most stable to least stable) in terms of Gibbs free energy of formation and cell potential under reducing conditions at 500, 650, and 800°C for chloride and oxide compounds of interest in this study are shown in Tables 2.2 and 2.3, respectively. The constituent chlorides and oxides of interest in this study include uranium, TRU, predominant fission products, relevant molten salt compounds, and primary materials of construction. (Notes to Tables 2.2 and 2.3: Grey columns were used for sorting highest to lowest values; colored text: **U and TRU species**; **group 3 and lanthanide fission products**; **group 1 and 2 fission products**; **noble metal fission products**; and **common chloride/oxide species and materials of construction**.

Table 2.2. Gibbs free energy of formation for select chlorides at 500, 650, and 800°C. [33]

Compound	500°C		650°C		800°C	
	$\Delta G_f°$ (kJ/mol Cl)	E° (V)	$\Delta G_f°$ (kJ/mol Cl)	E° (V)	$\Delta G_f°$ (kJ/mol Cl)	E° (V)
CsCl	-366.610	3.800	-353.095	3.660	-343.335	3.558
$BaCl_2$	-366.592	3.799	-355.348	3.683	-343.983	3.565
KCl	-362.658	3.759	-348.624	3.613	-335.692	3.479
RbCl	-361.201	3.744	-347.103	3.597	-335.176	3.474
$SrCl_2$	-356.962	3.700	-346.246	3.589	-336.006	3.482
LiCl	-344.843	3.574	-333.705	3.459	-325.403	3.373
$EuCl_2$	-341.075	3.535	-329.312	3.413	-318.684	3.303
NaCl	-339.284	3.516	-325.597	3.375	-312.297	3.237
$CaCl_2$	-338.919	3.513	-328.045	3.400	-317.670	3.292
$SmCl_2$	-338.528	3.509	-326.809	3.387	-315.186	3.267
$LaCl_3$	-293.623	3.403	-282.258	2.925	-267.529	2.773
$PrCl_3$	-289.323	2.999	-277.969	2.881	-267.129	2.769
$CeCl_3$	-289.226	2.998	-277.701	2.878	-266.344	2.760
$NdCl_3$	-283.923	2.943	-272.579	2.825	-262.165	2.717
YCl_3	-272.379	2.823	-261.228	2.707	-250.970	2.601
$AmCl_3$	-265.093	2.748	-253.987	2.632	-242.975	2.518
$PuCl_3$	-262.299	2.719	-251.372	2.605	-241.335	2.501
$MgCl_2$	-259.332	2.688	-247.013	2.560	-237.073	2.457
$CmCl_3$	-255.676	2.650	-239.290	2.480	-222.178	2.303
$NpCl_3$	-243.006	2.519	-232.288	2.408	-221.453	2.295
UCl_3	-232.761	2.412	-222.726	2.308	-212.662	2.204
ZrCl	-196.786	2.040	-185.159	1.919	-174.170	1.805
$AlCl_3$	-179.883	1.864	-172.768	1.791	-165.422	1.714
$CrCl_2$	-145.592	1.509	-137.178	1.422	-129.039	1.337
$TaCl_2$	-145.516	1.508	-136.868	1.419	-128.533	1.332
$FeCl_2$	-121.727	1.262	-112.989	1.171	-107.112	1.110
HCl(g)	-99.305	1.029	-100.345	1.040	-101.324	1.050
$NiCl_2$	-94.163	0.976	-83.403	0.864	-72.815	0.755
AgCl	-86.479	0.896	-82.760	0.858	-79.329	0.822
$MoCl_2$	-86.101	0.892	-75.395	0.781	-64.898	0.673
$TcCl_3$	-44.407	0.460	-35.390	0.367	-26.809	0.278
RhCl	-40.251	0.417	-32.848	0.340	-27.036	0.280
$PdCl_2$	-28.127	0.292	-17.720	0.184	-8.770	0.091
$RuCl_3$	-18.184	0.188	-7.993	0.083	1.839	-0.019

Table 2.3. Gibbs free energy of formation for select oxides at 500, 650, and 800°C. [33]

Compound	500°C		650°C		800°C	
	$\Delta G_f°$ (kJ/mol O)	E° (V)	$\Delta G_f°$ (kJ/mol O)	E° (V)	$\Delta G_f°$ (kJ/mol O)	E° (V)
Y_2O_3	-559.255	2.898	-545.073	2.825	-531.008	2.752
CaO	-553.929	2.871	-538.365	2.790	-522.714	2.709
Sm_2O_3	-532.584	2.760	-518.036	2.685	-503.500	2.609
Nd_2O_3	-528.680	2.740	-514.975	2.669	-501.369	2.598
Pr_2O_3	-528.490	2.739	-514.762	2.668	-501.153	2.597
Ce_2O_3	-528.084	2.737	-514.184	2.665	-500.331	2.593
La_2O_3	-522.786	2.709	-508.965	2.638	-495.278	2.567
MgO	-518.303	2.686	-502.361	2.603	-485.047	2.514
SrO	-516.537	2.677	-502.329	2.603	-487.941	2.529
EuO	-515.422	2.671	-501.492	2.599	-487.568	2.527
Pu_2O_3	-491.234	2.546	-478.142	2.478	-464.916	2.409
Am_2O_3	-491.090	2.545	-477.593	2.475	-464.271	2.406
Li_2O	-496.752	2.574	-475.734	2.465	-454.968	2.358
BaO	-481.481	2.495	-467.652	2.423	-453.201	2.349
UO_2	-475.143	2.462	-462.645	2.397	-449.940	2.332
Al_2O_3	-477.769	2.476	-462.260	2.396	-445.738	2.310
ZrO_2	-475.943	2.466	-461.946	2.394	-448.052	2.322
Cm_2O_3	-476.742	2.471	-456.658	2.366	-435.613	2.257
NpO_2	-469.247	2.432	-455.920	2.363	-442.312	2.292
Ta_2O_5	-339.262	1.758	-326.591	1.692	-314.098	1.628
Cr_2O_3	-310.917	1.611	-298.342	1.546	-285.874	1.481
Na_2O	-309.065	1.602	-288.238	1.494	-267.954	1.389
K_2O	-252.770	1.310	-232.789	1.206	-214.952	1.114
Cs_2O	-242.963	1.259	-226.939	1.176	-211.499	1.096
Rb_2O	-232.994	1.207	-217.934	1.129	-203.545	1.055
MoO_2	-222.819	1.155	-209.686	1.087	-196.765	1.020
FeO	-213.273	1.105	-203.916	1.057	-194.421	1.008
$H_2O(g)$	-205.013	1.062	-196.939	1.021	-188.691	0.978
NiO	-168.454	0.873	-155.269	0.805	-142.212	0.737
TcO_2	-157.205	0.815	-143.849	0.745	-130.657	0.677
RuO_2	-86.461	0.448	-74.650	0.387	-63.138	0.327
Rh_2O	-57.474	0.298	-51.053	0.265	-44.902	0.233
PdO	-33.232	0.172	-17.591	0.091	-2.117	0.011

2.2.1 Electrolytic Cells

Electrochemistry is a study of changes in chemical compounds that occur due to the flow of an electrical current (an electrolytic cell), or the production of electricity from a change in chemical compounds (a galvanic cell, or battery). [32] The work in this study primarily involves electrolytic cells with applied electrical currents and potentials. A simple electrolytic cell consists of two electrodes – an anode (where oxidation occurs) and a cathode (where reduction occurs) – and an electrolyte. A simple diagram of an electrolytic cell is shown in Figure 2.5.

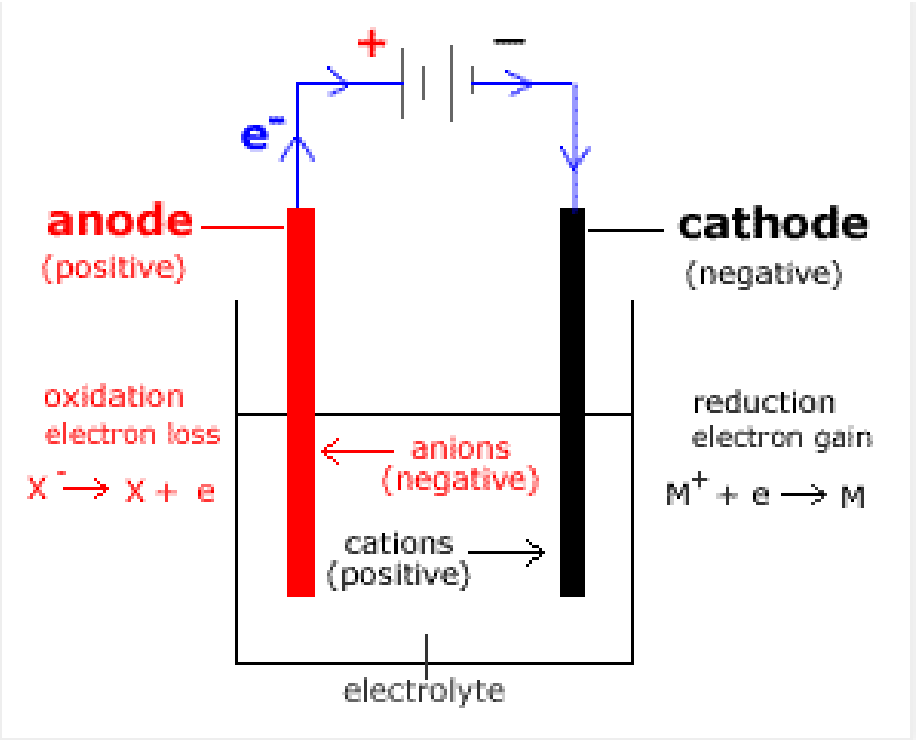

Figure 2.5. Diagram of a simple electrolytic cell. [34]

Electrons move through an external power supply that connects the electrically conductive anode and cathode. However, in the electrolyte the current is carried by negatively charged ions (anions) and positively charged ions (cations), which are free to

move in the electrolyte, as opposed to electron conduction. The reactions of chemical compounds occur at the interfaces between the electrodes and the electrolyte, which are termed heterogeneous electron-transfer reactions. [32] For example, if two inert electrodes were immersed in a pool of molten lithium chloride at 650°C containing a minor fraction of soluble lithium oxide, and an external power supply was applied at sufficient potential to decompose the lithium oxide, the following anodic and cathodic reactions (i.e., half-cell reactions) and full-cell reaction would occur.

Cathode reaction:	$4\ Li^{+} + 4\ e^{-} \rightarrow 4\ Li$	(2.16)
Anode reaction:	$2\ O^{2-} \rightarrow O_2(g) + 4\ e^{-}$	(2.17)
Full-cell reaction:	$2\ Li_2O \rightarrow 4\ Li + 2\ O_2(g)$	(2.18)

The above reactions are an example of an electrolysis reaction, which is one type of an electrolytic cell operation. The standard potential for the decomposition of lithium oxide in the above example at 650°C is 2.47 V (see Table 2.3).

Another common type of electrolytic cell operation is electrotransport, which involves the simultaneous dissolution and deposition of an electroactive species in an electrolytic cell. For example, if uranium metal were suspended as an anode in a pool of LiCl-KCl-UCl_3 at 500°C across from a cathode, an applied electric current or potential would dissolve uranium metal at the anode and simultaneously deposit uranium metal at the cathode per the following anodic and cathodic reactions.

Anode reaction: $U \rightarrow U^{3+} + 3\ e^-$ (2.19)

Cathode reaction: $U^{3+} + 3\ e^- \rightarrow U$ (2.20)

As an electrotransport process, there is no overall change in chemical compounds; uranium is merely moved from one electrode to another. If the uranium in the anode from the above example originated from an impure source and the objective of the electrotransport process was to recover a more pure uranium product at the cathode, then this process would be appropriately referred to as electrorefining. If the objective of the above example was to coat the cathode with a layer of uranium metal, then the electrotransport process would be more appropriately termed electroplating. Because there is no overall change in chemical compounds in this example, there is also no requisite cell potential (E°) to overcome, as in an electrolysis cell. Rather, an electrotransport process merely needs to overcome the overpotentials at the anode and cathode and ohmic resistance within the electrolyte to move the select electroactive species.

An important feature of electrolytic cells is that the reaction rate is a function of the applied current or potential. This feature is based on Faraday's law, which defines the relationship between the amount of current, or charge (Q), and the amount of material (m) and associated molecular weight (M_i) that is consumed or produced, as follows.

$$m_i = M_i\ Q / (n\ F) \quad (2.21)$$

The charge is the integrated current, as defined below for a variable current (I) and constant current (I), respectively.

$$Q = \int I \, dt \tag{2.22}$$

$$Q = I \, t \tag{2.23}$$

Faraday's constant (F) is further defined as the product of the fundamental unit of charge (q, 1.6E-19 coulombs or C) and Avogadro's number (N_{AV}), as follows. [32]

$$F = q \, N_{AV} \tag{2.24}$$

Thus, the reaction rate of an electrolytic cell may be controlled directly with a fixed current (galvanostatic) or indirectly with a fixed electric potential (potentiostatic) – the two primary modes of electrolytic cell operation.

An additional common feature in an electrolytic cell is a reference electrode, the purpose of which is to provide a known, stable potential against which other potentials can be measured. In principle, no current is passed through the reference electrode, thus leaving it at an equilibrium potential. [32] Silver-silver chloride (Ag/AgCl) is a common reference electrode, which consists of a silver wire in contact with a confined silver chloride solution, the housing of which is in ionic contact with the electrolyte. An electrochemical cell with a reference electrode is commonly referred to as a three-electrode system. A benefit of a three-electrode system is the ability to monitor relative effects of anode and cathode potentials under galvanostatic or potentiostatic control of an external power supply. Furthermore, a three-electrode system can be used in combination with a potentiostat to control an electrode potential (anode or cathode) relative to the reference electrode. The electrode potential that is being controlled relative to a reference electrode (RE) is termed the working electrode (WE) and the opposing electrode is termed the counter electrode (CE). A three-electrode system is often used in electroanalytical characterization of cells, including cyclic

voltammetry, chronoamperometry, and chronopotentiometry, which are discussed later in more detail (see Section 3.3.1).

2.3 Electrometallurgical Treatment Process

An EMT process was developed by researchers at Argonne National Laboratory (ANL) in the mid-1990s for treating sodium-bonded used metal fuel from fast reactors within the DOE complex. The need to treat this fuel was primarily driven by the reactive and pyrophoric nature of sodium, uranium, and plutonium metals in the fuel, which would likely preclude its direct (i.e., untreated) disposal in a geological repository. Additionally, sodium-bonded used fuel contained HEU which, if left untreated, was viewed as a proliferation concern to DOE. Consequently, when EBR-II was shut down in 1994, DOE officials moved rapidly to address the proliferation threat of the surplus HEU from EBR-II driver fuel and demonstrate to other nations the U.S. commitment to nonproliferation. [35] Accordingly, DOE initiated an Environmental Impact Statement (EIS) in 1999 for the treatment and management of sodium-bonded used nuclear fuel, which was issued in 2000 along with a Record of Decision to proceed with EMT for used sodium-bonded EBR-II fuel. [12, 36] In support of the EIS was an independent review of the EMT process, which began in 1994, by the National Research Council. The Council issued its final report in 2000. [37] The following summarizes the EMT process as described in these federally produced public documents.

Sodium-bonded used nuclear fuel in DOE's inventory consists primarily of two types – driver fuel and blanket fuel. Used driver fuel operated within the center of a sodium-cooled fast reactor and provided the primary power production of the reactor. The driver fuel contained uranium alloys that were highly enriched in uranium-235. Used EBR-II driver fuel

consisted of HEU that was typically alloyed with either zirconium or fissium (an alloy of molybdenum, ruthenium, rhodium, palladium, zirconium, and niobium). Thus, the two primary alloys in used EBR-II driver fuel were alloys of 90% HEU and 10% zirconium or 95% HEU and 5% fissium. The EBR-II driver fuel alloys were cast into pins and loaded with sodium in a 74-cm long stainless-steel tube (cladding). The tube was welded shut, as depicted in Figure 2.6, forming the primary boundary for the used fuel and associated fission products. As the driver fuel was irradiated in EBR-II (upwards of 20% burnup), the metallic fuel would swell and perforate until it contacted the cladding wall, causing bond-sodium to enter the porous fuel matrix and to displace into the plenum region above the fuel pin. [36]

Blanket fuel consisted of depleted uranium (DU) metal, which was typically 99.8% uranium-238 and 0.2% uranium-235. The blanket fuel was positioned radially outward of the driver fuel in a sodium-cooled fast reactor. Containing primarily fertile uranium-238, the blanket fuel produced fissile plutonium-239 as it absorbed neutrons produced primarily from fission in the driver fuel. Although, blanket fuel yielded some fission from its fissionable and fissile components, amounting to 0.1% burnup on average for used EBR-II blanket fuel. EBR-II blanket fuel consisted of multiple DU pins that were stacked with bond-sodium inside a stainless-steel tube and sealed, forming a blanket element, as also depicted in Figure 2.6.

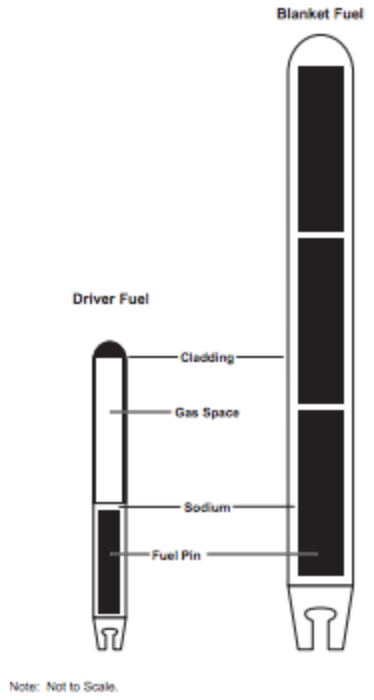

Figure 2.6. Simplified sectional view of EBR-II driver and blanket fuel elements. [36]

The EMT process encompasses a series of unit operations to dismantle and size used sodium-bonded fuel into a feed for an electrorefiner, which produces refined uranium metal. (Note: Electrorefining is a century-old technology used to produce pure metals from an impure metal feedstock.) Cladding hulls and undissolved fuel constituents from the electrorefiner are further processed into a metallic waste form. Other fuel constituents accumulate in the molten salt electrolyte of the electrorefiner, which salt is periodically removed and processed into a ceramic waste form. A summary flow diagram of the EMT process is shown in Figure 2.7. [36]

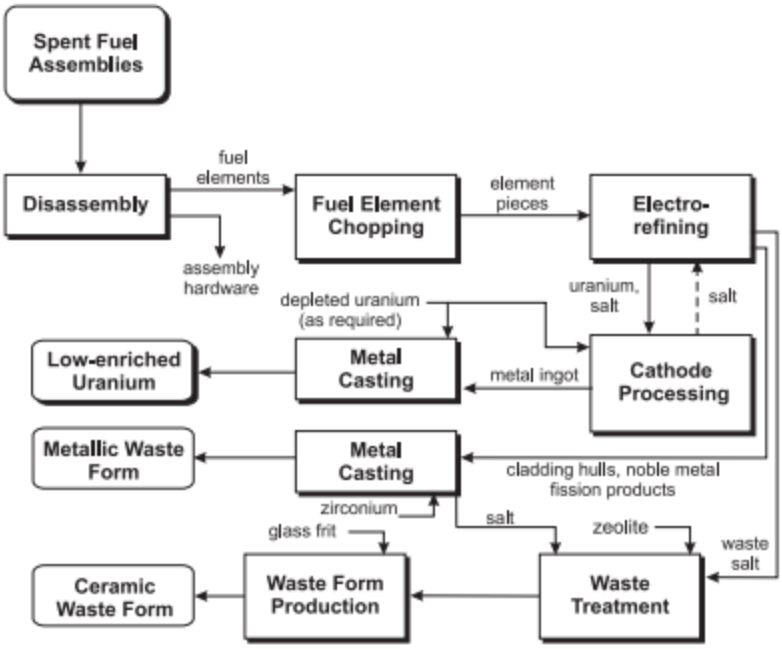

Figure 2.7. Summary flow diagram of the EMT process.

The first step of the EMT process involves mechanical separation of the fuel elements from assembly hardware. The elements are then chopped into short segments and placed into perforated steel baskets. A loaded basket is then immersed into a molten pool of lithium chloride and potassium chloride eutectic, containing a low concentration of uranium trichloride, at about 500°C in an electrorefiner. A bare steel rod is also suspended in the salt pool. The basket and steel rod are electrically connected as anode and cathode, respectively, to a power supply. A fixed current (galvanostatic) or voltage (potentiostatic) is applied to anodically dissolve impure uranium from the basket into the salt pool, from which uranium ions are simultaneously deposited as uranium metal on the cathode rod. During the uranium electrorefining process, bond sodium, transuranic elements (including plutonium), and the bulk of the fission products, dissolve into the salt pool. Once uranium from a batch of used fuel in an anode basket has been electrotransported to a cathode rod, the rod is removed to

harvest the deposited uranium metal. The basket, which contains the stainless-steel cladding hulls and insoluble fission products, is also removed. [36-37]

The harvested uranium metal is occluded with salt from the electrorefiner. Consequently, the salt-occluded product is loaded into a cathode processor (a vacuum furnace) to volatilize off the salt and consolidate the uranium product into an ingot. Depleted uranium is added to the product to lower the uranium-235 concentration, as needed. The recovered salt is returned to the electrorefiner. The uranium ingot is further processed in a casting furnace, in which depleted uranium is added, as needed, to produce a cast LEU product. [37]

The cladding hulls and insoluble fission products are mechanically removed from an anode basket and loaded into a metal casting furnace (a vacuum furnace) along with a predetermined amount of zirconium metal. The furnace is heated to melt the mixture and produce a metal waste form that is expected to be suitable for disposal in a geological repository. [36-37]

Periodically, salt is removed from the electrorefiner and combined with salt recovered from the metal waste form process. The salt is ground to a specific particle size and blended with zeolite. The blend is heated to effect the absorption of salt into the zeolite, which is designed to capture fission product ions from the salt into the zeolite microstructure. Glass frit is then added to the mixture, which is heated and pressed into a ceramic waste form. The ceramic waste form is also expected to be suitable for disposal in a geological repository. [36-37]

The distribution of fission products in an electrorefining process is defined by the thermodynamic stability of the used fuel constituents in a chloride phase at system temperature. A plot of Gibbs free energies of formation for select used fuel constituents at 500°C from Table 2.2 is shown in Figure 2.8. Under equilibrium conditions, those fuel constituents more active (i.e., more negative Gibbs free energy of formation) than uranium trichloride partition from an anode basket to the chloride salt phase, while those constituents more noble (i.e., less negative Gibbs free energy of formation) than uranium trichloride remain in an anode basket, including steel cladding hulls. [36]

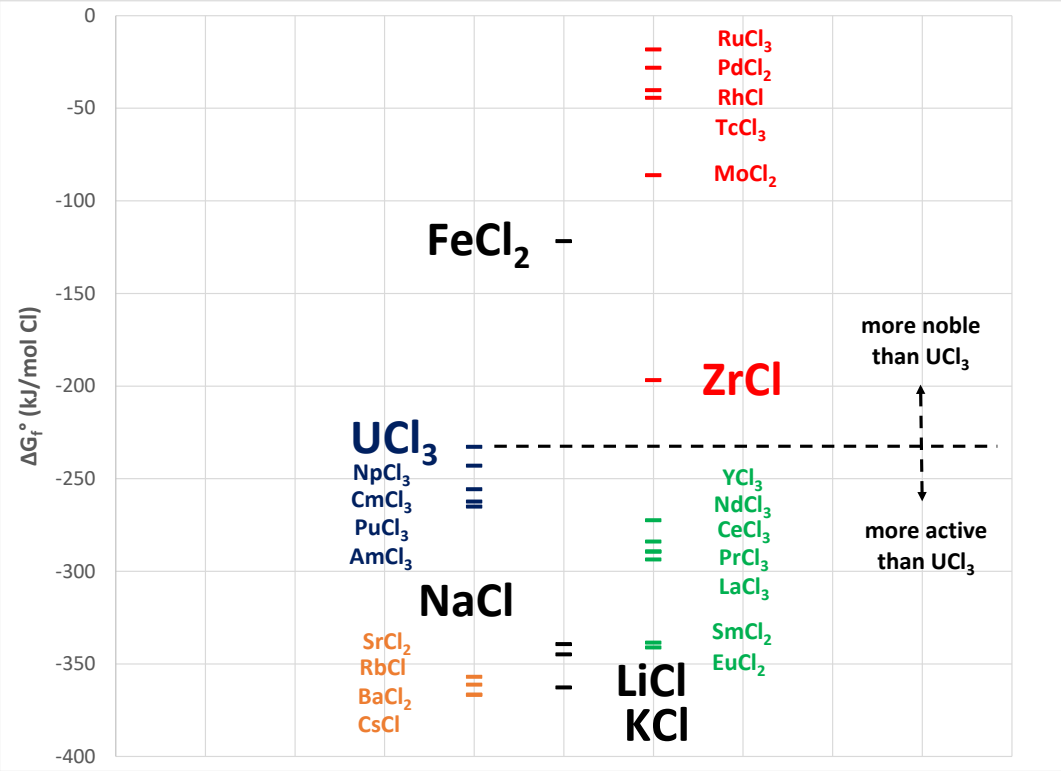

Figure 2.8. Plot of Gibbs free energies of formation for select fuel constituent chlorides. (Note: Major salt and fuel constituents are in large font.)

In brief, the EMT process receives used sodium-bonded nuclear fuel and produces three product streams – LEU metal, a metal waste form, and a ceramic waste form. The

process fulfills DOE's objectives of (1) deactivating the pyrophoric nature of sodium-bonded used nuclear fuel by converting active components into stable chlorides and (2) removing a proliferation threat by converting HEU into LEU. Furthermore, fission products (including TRU constituents) and fuel hardware are placed into robust, leach-resistant waste forms, suitable for a geological repository. After an initial three-year demonstration of the EMT process with EBR-II driver and blanket fuel, the National Research Council concluded that "the committee has found no significant barriers in the use of electrometallurgical technology to treat EBR-II spent fuel, and the EMT therefore represents a potentially viable technology for DOE spent nuclear fuel treatment." [12, 36-37] The EMT process continues to operate to date at INL's FCF to treat use sodium-bonded fuel within the DOE complex.

2.4 Extension of Electrometallurgical Treatment Process to Other Research Reactor Fuels

An EMT process can be extended to other research reactor fuels, including used nuclear oxide fuels and aluminum matrix fuels within the DOE complex. Indeed, the extension of EMT to such fuels was addressed in DOE's EIS and Record of Decision for sodium-bonded fuels. Specifically, these documents state that modifications to the EMT process could be used for the treatment of spent oxide, nitride, and carbide fuels. [12, 36] Additionally, the National Research Council's review of the EMT process identified its possible extension to aluminum matrix fuels. [37] These extensions may be accomplished by appropriate head-end operations to (1) convert oxide fuels to metal prior to electrorefining and (2) separate aluminum from aluminum matrix fuels prior to EMT. The following addresses extension of EMT to used nuclear oxide and aluminum matrix fuels.

2.4.1 Used Nuclear Oxide Fuels

In conjunction with development of an EMT process for used sodium-bonded fuel, researchers at ANL developed a lithium-based metallothermic process to reduce uranium oxide to uranium metal as a head-end step to uranium electrorefining. [38-41] This form of an oxide reduction process consisted of contacting uranium oxide particulate or pellets with molten lithium chloride that was saturated with lithium metal at 650°C, yielding the following reaction.

$$4\ Li + UO_2 \rightarrow U + 2\ Li_2O \qquad (2.25)$$

Because a metallic reducing agent (lithium metal) is used to form a metal product (uranium), the Gibbs free energy of reaction becomes the difference between the Gibbs free energies of formation for lithium oxide and uranium oxide. From Table 2.3, lithium oxide is more stable than uranium oxide by a margin (accounting for 2 moles of oxygen) of -26.2 kJ/mol at 650°C, i.e., the Gibbs free energy of reaction for Eq. (2.25). (Note: An operating temperature of 650°C is used for sufficient operating margin above the 610°C melting point of lithium chloride.) While the thermodynamic stabilities of select oxides in Table 2.3 show the ability of lithium metal to reduce uranium oxide, the reduction of oxides more stable than lithium oxide requires non-unit activities of lithium oxide (i.e., sub-saturated lithium oxide concentrations in lithium chloride).

From Table 2.3, it is evident that a calcium-based metallothermic reduction of metal oxides would be a stronger reducing system, owing to the higher thermodynamic stability of a calcium oxide product. Accordingly, a calcium-based metallothermic reduction process would be capable of reducing to metal nearly all the select metal oxides in Table 2.3

(excepting yttrium oxide) at unit activities. A calcium-based metallothermic reduction process was investigated by researchers at ANL as an alternative to a lithium-based process. However, the calcium-based process was dismissed in favor of a lithium-based process due to (1) a lower operating temperature for a lithium-based system (i.e., 650°C) compared to a calcium-based system that would operate in excess of 800°C (owing to a 772°C melting point for $CaCl_2$), and (2) the less consequential impact of material carryover from a lithium-base reduction system to a LiCl-KCl-based electrorefining system than that from a calcium-based reduction system.

The reducing agent and associated oxide product in a metallothermic reduction system are best suited for operation in their companion salt, e.g., lithium/lithium oxide in lithium chloride or calcium/calcium oxide in calcium chloride, due to the higher solubilities of the reducing metals and their respective oxides in their companion salts. Specifically, the solubility of lithium oxide in lithium chloride at 650°C is 8.7 wt% [38], whereas the same in LiCl-KCl eutectic at 500°C is 0.8 wt%. [42] Furthermore, the introduction of lithium metal into LiCl-KCl can lead to fuming potassium metal. [39] Consequently, researchers at ANL initially settled on a lithium-based metallothermic form of an oxide reduction process in lithium chloride at 650°C.

A lithium-based metallothermic reduction process for uranium oxide yielded a buildup of lithium oxide product concentration in the salt pool that corresponded to the extent of reaction. However, elevated lithium oxide concentrations in contact with reduced uranium metal were a detriment to subsequent salt distillation and/or uranium electrorefining operations, causing reduced uranium to revert to uranium oxide. Furthermore, the lithium oxide-laden lithium chloride salt following a metallothermic reduction required a separate

electrowinning step to recover lithium metal via decomposition of lithium oxide in the salt per half-cell and full-cell reactions outlined in Eqs. 2.16 – 2.18.

These drawbacks to a lithium-based metallothermic reduction of uranium oxide became an impetus to improve the oxide reduction process. Consequently, researchers at ANL introduced an electrolytic reduction form of an oxide reduction process, which essentially combined the lithium reduction and electrowinning steps by configuring a uranium oxide-loaded steel basket as a cathode along with an inert metal anode (e.g., platinum) in an electrolyte of lithium chloride – 1 wt% lithium oxide electrolyte at 650°C. [43] A simplified electrochemical cell diagram for a lithium-based electrolytic reduction process is shown in Figure 2.9.

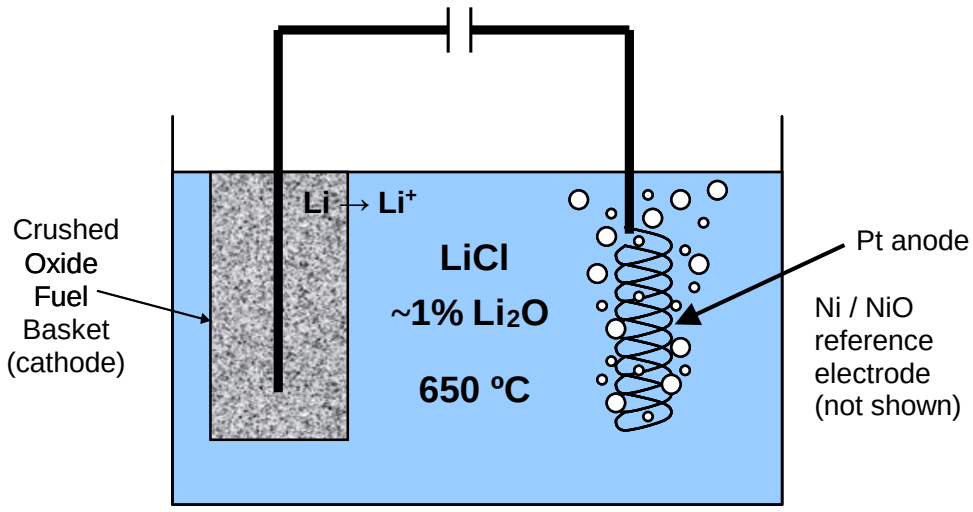

Figure 2.9. Simplified electrochemical cell diagram for an electrolytic reduction process.

The standard potentials (E°) for the primary constituent reactions in a lithium-based electrolytic reduction process at 650°C are found in Tables 2.2 and 2.3, as shown below.

$UO_2 \rightarrow U + O_2(g)$, $E° = 2.40$ V (2.26)

$Li_2O \rightarrow 2\ Li + ½\ O_2(g)$, $E° = 2.47$ V (2.27)

$LiCl \rightarrow Li + ½\ Cl_2(g)$, $E° = 3.46$ V (2.28)

The above standard potentials show a relatively large electric potential window between lithium oxide and lithium chloride (i.e., 1 V) in which an electrolytic reduction cell can operate to effect reduction of uranium and lithium oxides without decomposition of the base lithium chloride salt. However, operation of the cell at an electric potential between that of uranium oxide and lithium oxide, even at non-unit activities, would be challenging. Consequently, the lithium-based electrolytic reduction process typically operates at an electric potential to reduce both uranium and lithium ions at a cathode and simultaneously oxidize oxygen ions in the salt at an anode per the following half-cell and full-cell reactions. The electrolytically produced lithium metal (see Eq. 2.34) chemically reduces uranium oxide to uranium metal (see Eq. 2.25).

Cathode: $UO_2 + 4\ e^- \rightarrow U + 2\ O^{2-}$ (2.29)

Anode: $\underline{2O^{2-} \rightarrow O_2(g) + 4\ e^-}$ (2.30)

Full cell: $UO_2 \rightarrow U + O_2(g)$ (2.31)

Cathode: $4\ Li^+ + 4\ e^- \rightarrow 4\ Li$ (2.32)

Anode: $\underline{2O^{2-} \rightarrow O_2(g) + 4\ e^-}$ (2.33)

Full Cell: $4\ Li^+ + 2\ O^{2-} \rightarrow 4\ Li + O_2(g)$ (2.34)

Since the advent of a lithium-based electrolytic reduction process, a wide variety of experimental studies regarding its application to uranium and actinide metal oxides by

various academic and national laboratory researchers within the U.S. [44-54], Japan [55-63], Republic of Korea [64-103], and India [104] have been performed. These studies can be divided primarily into their focus areas with particular emphases on cathodic reactions [44-49, 54-56, 60, 64-69, 72-76, 79-81, 88-89, 94, 98, 100, 103], anodic reactions [52-53, 71, 78, 82-84, 87, 90, 92-93, 95-96, 101, 104], the electrolyte [57-58, 62, 77, 99, 102], and integration with other pyroprocesses [50-51, 59, 61, 63, 70, 85-86, 91, 97]. Experimental studies on electrolytic reduction of used nuclear oxide fuel have been limited to those at INL, which highlighted extents of uranium reduction as well as the distribution of fission products in the reduction process. [44-47, 50-51] In brief, extents of uranium reduction in used uranium oxide fuels typically exceeded 98%, while those from used MOX fuel were lower. Group 1, 2, 16, and 17 fission products (including cesium, rubidium, barium, strontium, tellurium, and iodine) partitioned from the used fuel and accumulated in the lithium chloride salt phase, while reduced uranium, transuranic constituents, and the balance of fission products remained in the cathode basket.

The distribution of fuel constituents in an electrolytic reduction process is readily determined by elemental and isotopic analysis of salt and reduced fuel samples. However, the chemical forms of the fuel constituents in the reduced fuel are less known. An analytical technique using bromine to dissolve and separate a metal phase from a metal / metal oxide mixture can be used to differentiate metallic and oxidized uranium (the primary component in used fuel) in a reduced fuel sample. [105-106] In fact, this technique has been used to determine extents of uranium reduction in reduced used uranium oxide fuels. [44-46, 50-51]. The bromine dissolution technique has been validated with pure uranium metal and uranium oxide sources. The same technique should apply to other metal and metal oxide species

within used fuel, including TRU and lanthanide fission products; however, the bromine dissolution technique has not been validated for these other metal and metal oxide species as it has with uranium metal and uranium oxide. Consequently, the application of this technique to other metal and metal oxide species within used fuel can only be considered approximations.

The distinction between metal and oxide phases and the concentrations of residual oxides in a reduced fuel product are critical in assessing the performance of the product in subsequent pyroprocesses. Specifically, the subjection of a basket of reduced fuel to elevated temperature and reduced pressure to remove occluded salt following an oxide reduction process introduces changes to the thermodynamic stabilities and associated chemical activities between fuel constituents and a volatile salt phase. Consequently, reduced metal species (M) can revert to oxide species under these vacuum distillation conditions, including lanthanide, TRU, and uranium constituents, per the following generalized reaction.

$$M + Li_2O \rightarrow M_xO_y + Li \uparrow \qquad (2.35)$$

The introduction of a basket of reduced fuel to a uranium electrorefining system (with or without distillation of adhering oxide reduction salt) would invariably introduce some oxide species along with the bulk metal phase into the latter system, possibly including lanthanide, TRU, uranium, and lithium oxides. The bulk uranium metal phase can be electrorefined, as described previously (see Eqs. 2.19 and 2.20). Other metals, including TRU and lanthanides, can enter an electrorefining salt phase in one of two ways: (1) by anodic dissolution, like that of uranium as shown in Eq. 2.19; or (2) by chemical reaction with uranium trichloride in an electrorefining salt via the following generalized reaction mechanism.

$$3/z\ M + UCl_3 \rightarrow 3/z\ MCl_z + U \qquad (2.36)$$

Where: M = active metal phase constituent

The latter mechanism applies to those fuel constituents in a metal phase, which are more active than uranium trichloride in a chloride phase, as illustrated in Figure 2.8. The fate of oxides that are introduced into a uranium electrorefining system is less known. In previous studies which showed relatively high extents of uranium, TRU, and lanthanide reduction along with corresponding partitioning of these constituents into an electrorefining salt system, the fate of trace quantities of unreduced active metal oxides was summarily described by the following generalized reaction mechanism. [50-51]

$$M_xO_y + UCl_3 \rightarrow MCl_z + UO_2 \qquad (2.37)$$

While the above mechanism holds relatively little significance regarding the fate of minor concentrations of active metal oxide species in well-reduced used oxide fuel, its significance warrants further investigation for low-reduced, or even unreduced, used oxide fuel systems. For example, an electrolytic reduction run with used MOX fuel in a previous study yielded substantially lower extents of uranium, TRU, and lanthanide oxide reduction, i.e., 29%, 16%, and 2%, respectively. Regardless of the low extents of reduction, nearly all the TRU and lanthanide constituents partitioned to the electrorefining salt phase. [51] **This observed phenomenon warranted further investigation into the dissolution of used nuclear oxide fuel constituents in molten salt systems, which was a primary objective of this study.** Specific objectives of this aspect in this study included what reaction mechanisms might be occurring and how these mechanisms might be enhanced.

Experimental observations of used nuclear oxide fuel dissolution in molten chloride salt systems are described in Section 4 of this study.

2.4.2 Used Aluminum Matrix Fuels

Aluminum matrix fuels are widely used in materials testing reactors throughout the world, including ATR at INL. ATR is fueled with a total of 40 HEU driver elements that are uniquely arranged into a four-leaf-clover shape to facilitate concentrated neutron densities within designated regions of the core, as illustrated in Figure 2.10. [107] Each individual driver element is composed of 19 curvilinear fuel plates of different widths, isometric and cross-sectional views of which are also shown in Figure 2.10. [108]

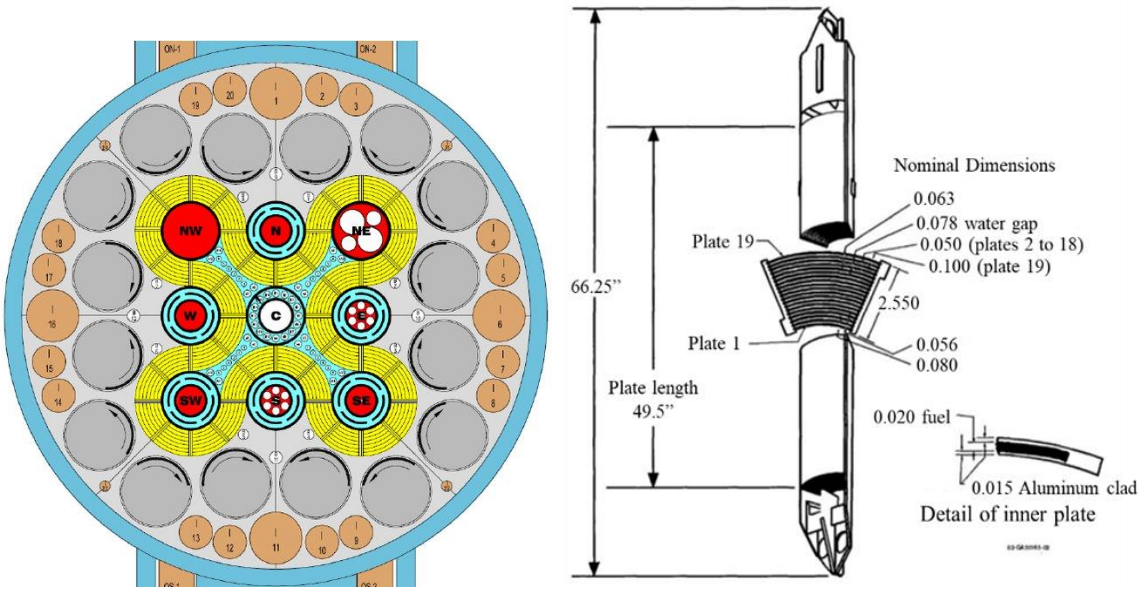

Figure 2.10. Cross-sectional view of the ATR core (left) and combined isometric / cross-sectional view of an individual ATR fuel element (right).

The fuel in each of the curvilinear plates is a uranium aluminide-aluminum dispersion matrix. Specifically, HEU metal and aluminum metal are melted, cast, and sized into a uranium aluminide powder, typically consisting of UAl_3 (63 wt%), UAl_4 (31 wt%), and UAl_2 (6 wt%) and commonly referred to as UAl_x. [109] The uranium aluminide powder is dispersed in aluminum metal powder and clad with 6061 aluminum alloy in a hot roll-bonding process. During the hot rolling and associated annealing steps, almost all the UAl_2 reacts with excess aluminum from the matrix to form UAl_3 and some UAl_3 reacts to form UAl_4. Consequently, the UAl_x in the final ATR fuel matrix consists of UAl_3 (60 wt%) and UAl_4 (40 wt%) with uranium densities up to 1.7 g/cc. [110]

The typical burnup of ATR HEU fuel is 40% [111], which for nominal ATR operations results in the generation rate of 30 or more used ATR fuel elements per year. [112] Used ATR fuel elements are temporarily stored in underwater racks near the reactor site, while awaiting an ultimate disposition path that may include reprocessing (e.g., at the U.S. DOE Savannah River Site's H-canyon facility) or disposal in a repository. [112] To date, thousands of used ATR fuel elements have accumulated in wet and dry storage areas at INL.

As a metal fuel, used ATR fuel would appear to be well-suited for EMT. Indeed, extension of an EMT process has been proposed for used ATR fuel [37]. However, the extension of EMT to used ATR fuel is complicated by the presence of aluminum in a uranium electrorefining system. Specifically, uranium and aluminum form stable intermetallic compounds, as indicated by elevated melting points in an Al-U binary phase diagram (Figure 2.11) and the following formation reactions. [33]

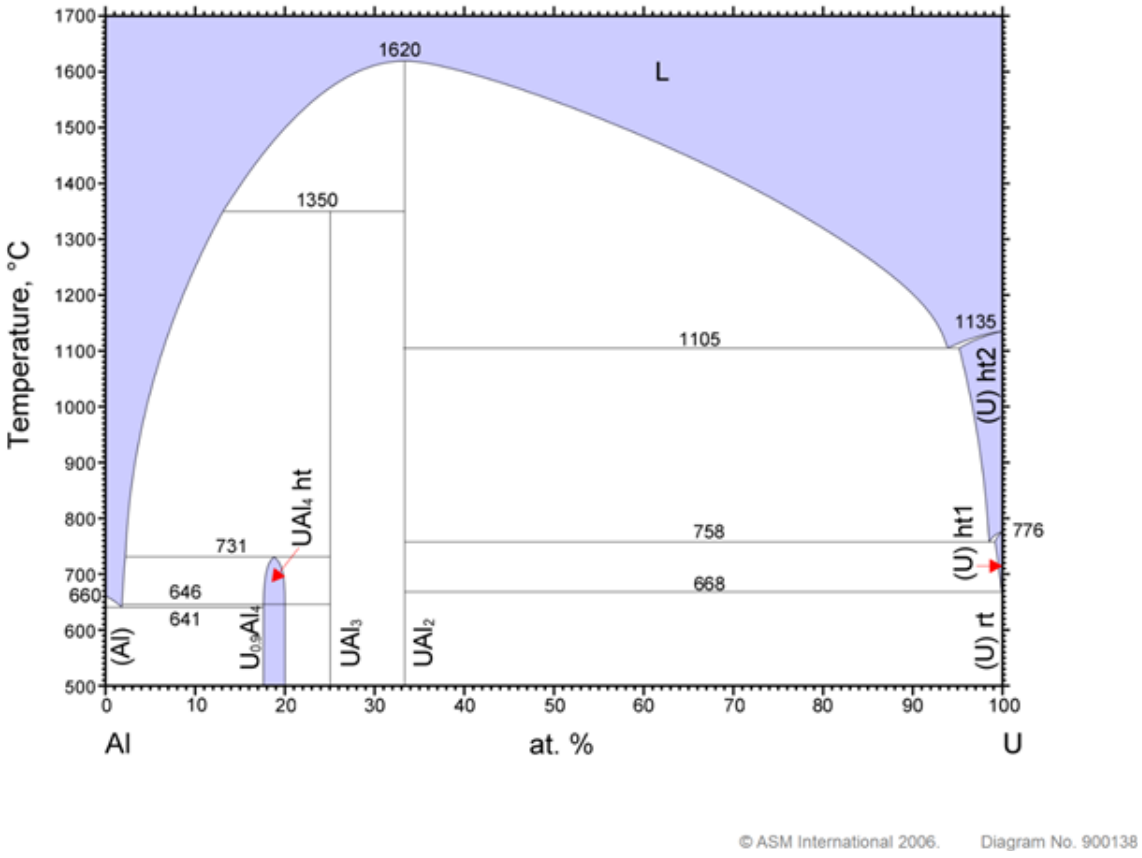

Figure 2.11. Uranium-aluminum binary phase diagram. [113]

$$U + 2\ Al \rightarrow UAl_2 \qquad \Delta G_f\ (500C) = -91.203\ kJ/mol \qquad (2.38)$$

$$U + 3\ Al \rightarrow UAl_3 \qquad \Delta G_f\ (500C) = -104.656\ kJ/mol \qquad (2.39)$$

$$U + 4\ Al \rightarrow UAl_4 \qquad \Delta G_f\ (500C) = -129.587\ kJ/mol \qquad (2.40)$$

The high thermodynamic stabilities of uranium aluminide compounds result in overpotentials that are needed to effect their anodic dissolution in an EMT uranium electrorefining system. Conversely, a uranium cathode would create an underpotential for aluminum metal deposition in the same system. Consequently, uranium and aluminum would tend to co-dissolve at the anode and co-deposit at the cathode in a uranium electrorefining system, as defined for the EMT process. Indeed, the co-dissolution of

uranium-aluminum and consequent inability to separate uranium from aluminum in a uranium electrorefining system was observed in an experimental study. [114]

To effectively separate and recover HEU from used ATR fuel in an EMT process, it is generally understood that a headend step is required to first remove the aluminum component. Researchers at ANL proposed and demonstrated an approach to remove aluminum from a uranium-aluminum alloy by (1) adding silicon to the alloy, (2) selectively electrorefining away aluminum in a fluoride electrolyte, and (3) recovering uranium via electrorefining in a separate electrorefiner with a different fluoride electrolyte. [115-118] Results from this demonstration were limited to the aluminum electrorefining step, where uranium concentrations in the aluminum cathode product ranged from 0.05 – 6 wt% and aluminum concentrations in the original U-Al-Si alloy ranged from 5.2 – 14.7 wt%.

While not related to EMT of used ATR fuel, researchers from the European Union (EU) used aluminum as a cathode in a uranium electrorefiner to exploit the thermodynamic stability and associated co-deposition of not only uranium but also TRU metals onto an aluminum metal cathode in a chloride electrolyte. [119-122] The use of an aluminum cathode to form actinide-aluminum alloys in a uranium electrorefiner has an advantage in improved separation of actinides from lanthanides over other reactive cathodes, such as a liquid cadmium cathode. However, an additional step is required to separate and recover actinides from the actinide-aluminum alloy, which the same EU researchers demonstrated by chlorination. Experiments were conducted with uranium-aluminum alloys that were exposed to pure chlorine gas [119-121] and hydrogen chloride gas [122]. Specifically, several experiments with chlorination of gram and sub-gram quantities of pulverized UAl_3/UAl_2 with

varying extents of excess pure chlorine gas were conducted in a temperature range of 150-170°C, yielding a UCl_4/UCl_3 and $AlCl_3$ product per the following reaction mechanisms.

$$U + x/2\ Cl_2(g) \rightarrow UCl_x \quad (2.41)$$

$$Al + 3/2\ Cl_2(g) \rightarrow AlCl_3 \quad (2.42)$$

Under these conditions, extents of U-Al chlorination approaching 99.8% were achieved over a 40-hour exposure period in a pass-through system. Operations at 150°C were preferred to preclude the formation of unwanted volatile UCl_5, traces of which were observed at 170°C. Once the alloy was chlorinated, the mixed UCl_x-$AlCl_3$ product could be heated above 180°C, at which temperature $AlCl_3$ sublimes and separates from the UCl_x.

Similar studies by some of the same EU researchers using HCl gas were conducted, based on the following reaction mechanisms.

$$U + x\ HCl(g) \rightarrow UCl_x + x/2\ H_2(g) \quad (2.43)$$

$$Al + 3\ HCl(g) \rightarrow AlCl_3 + 3/2\ H_2(g) \quad (2.44)$$

The use of HCl gas to chlorinate UAl_3/UAl_2 afforded higher operating temperatures (300 – 400°C), as the hydrogen gas product suppressed the formation of unwanted volatile UCl_5 or UCl_6. Also, chlorination at 300 – 400°C resulted in simultaneous sublimation of $AlCl_3$. Essentially complete UAl_3/UAl_2 chlorination and $AlCl_3$ sublimation was observed at 300°C, while less favorable results were observed at 350 and 400°C.

The favorable results achieved by EU researchers with chlorination and separation of aluminum from actinides in the proposed use of an aluminum cathode in a uranium electrorefiner suggest that such an approach could be applicable to used aluminum matrix

fuels, including used ATR fuel. Indeed, researchers at the Comision Nacional de Energia Atomica (CNEA) of Argentina proposed chlorination of used aluminum-uranium fuel in their country with chlorine gas as high as 500°C to convert all constituents in the used fuel to their respective chlorides and to separate volatile aluminum chloride. [123] However, their proposal and accompanying theoretical study have not been validated experimentally. Furthermore, the open literature appears to be lacking in experimental studies regarding chlorination of used aluminum matrix fuels. **Thus, a focus of this study was to perform experimental scoping studies applicable to dissolution of used ATR fuel in molten salt systems.** Specifically, a Nd-Al system was used as a non-radioactive surrogate for U-Al to perform dissolution studies in chloride and bromide media. Observations from the dissolution experiments are described in Section 5 of this study.

2.5 Deactivation of Sodium Metal via Dissolution in a Molten Salt System

The use of sodium metal in nuclear reactors is a double-edged sword. As a nuclear reactor coolant, sodium metal has a substantially higher thermal conductivity than pressurized water, and it functions at ambient pressure. However, its reactive and pyrophoric nature introduces hazards that require mitigation while in use, including isolation from air and water, and suitable deactivation prior to disposal. Sodium metal is renowned for its reactivity with air (i.e., oxygen in air) and water per the following reactions, respectively.

$$4\ Na + O_2(g) \rightarrow 2\ Na_2O \qquad \Delta H_{Rx,25C} = -830\ kJ \qquad (2.45)$$

$$2\ Na + 2\ H_2O \rightarrow 2\ NaOH + H_2(g) \qquad \Delta H_{Rx,25C} = -280\ kJ \qquad (2.46)$$

After ignition, sodium metal burns readily in air with sufficient heat generation to volatilize the metal and expand its capability to oxidize in the vapor phase forming a sodium

oxide aerosol. If the aerosol were properly contained and directed to a wet scrubber, the sodium oxide would react with water to form a sodium hydroxide solution per the following reaction.

$$Na_2O + H_2O \rightarrow 2\ NaOH \qquad \Delta H_{Rx,25C} = -151\ kJ \qquad (2.47)$$

In fact, the above approach was used for deactivation of a portion of the NaK coolant from EBR-I. Specifically, the NaK was burned in air and the resultant aerosol was collected in a wet scrubber, forming a hydroxide solution that was subsequently carbonated with carbon dioxide gas and solidified into a cementitious mixture. [124] (Note: The reactions of potassium metal in NaK occurred analogously to those identified for sodium metal in Eqs. 2.45 and 2.47.)

The reaction of sodium directly with water could lead to a violent reaction, if the generated hydrogen gas subsequently ignited in air by the heat evolved from the sodium/water reaction leading to the following explosive hydrogen/oxygen reaction.

$$2\ H_2(g) + O_2(g) \rightarrow 2\ H_2O \qquad \Delta H_{Rx,25C} = -572\ kJ \qquad (2.48)$$

If air were excluded from a sodium/water reaction, then the explosive hydrogen/oxygen reaction could be eliminated. The resulting sodium/water reaction would still be considered vigorous with sufficient heat evolved to boil the sodium hydroxide solution. However, if sodium metal and water were metered into a concentrated sodium hydroxide solution under a nitrogen atmosphere, the deactivation of sodium to sodium hydroxide could proceed in a controlled fashion. As a matter of fact, the above approach was used to deactivate and dispose of 87,000 gallons and 13,000 gallons of sodium metal primary and secondary coolant, respectively, from EBR-II in what was termed a caustic-injection process. [125]

The above-described methods for deactivation of bulk NaK and sodium metal coolants occurred in separate facilities dedicated to these types of alkali metal treatments. Even though the NaK and sodium coolants were slightly radioactive, the treatment equipment was manually operated and did not require radiological shielding. In contrast, bond sodium from EBR-II driver and blanket fuel is in contact with nuclear fuel and some migration of fission products, particularly cesium-137, into the sodium has occurred. Thus, deactivation of separated bond sodium would most likely need to be accomplished remotely, due to elevated radioactivity levels. Currently, portions of the bond sodium in used EBR-II fuel are deactivated upon immersion of the chopped fuel elements in uranium electrorefining salt via reaction with uranium trichloride, as shown in Eq. 2.36 and as illustrated in Figure 2.8. However, depletion of uranium trichloride in a uranium electrorefiner electrolyte is undesirable, as it requires periodic replenishment. Furthermore, sodium chloride formation in the electrolyte impacts the melting point and consequent useful lifetime of a uranium electrorefiner electrolyte. Therefore, deactivation of plenum sodium (i.e., bond sodium above the fuel column in an EBR-II driver fuel element that is not included in the uranium electrorefining process) requires a separate deactivation method. Researchers at INL have investigated deactivation options for bond sodium, including reaction with metal chlorides. [126] **A focus of this study was to investigate the deactivation of bond sodium using metal and non-metal chlorides.** Specifically, the deactivation of sodium metal with iron (II) chloride and ammonium chloride, each forming sodium chloride, was investigated. Experimental observations of sodium metal deactivation are described in Section 6 of this study.

2.6 Synthesis of High-Purity Uranium Trichloride for Use in Molten Salt Dissolution Studies

Synthesis of uranium trichloride can be performed by a variety of methods, particularly if uranium tetrachloride is formed as a precursor. Uranium tetrachloride can be prepared with a uranium feed as metal, oxides, hydrides, nitrides, carbides, and sulphides under the reaction of various chlorinating agents, including thionyl and carbon chlorides. Once formed, uranium tetrachloride can be reduced by a variety of metals to form uranium trichloride, per the following reaction. [127]

$$x\ UCl_4 + M \rightarrow MCl_x + x\ UCl_3, \text{ where M = reducing metal} \quad (2.49)$$

To limit the number of constituents (and possible contaminants) involved with uranium trichloride synthesis and to simply the process, methods of reacting uranium metal with metal chlorides have been pursued, several of which have been reported in the literature. Theoretically, any metal chloride that is less thermodynamically stable (i.e., has a less negative Gibbs free energy of formation) than uranium trichloride, examples of which are listed in Table 2.2, could form uranium trichloride upon reaction with uranium metal per the following generalized reaction mechanism.

$$3/x\ MCl_x + U \rightarrow UCl_3 + 3/x\ M, \text{ where M = metal} \quad (2.50)$$

However, some metal chlorides could lead to uranium tetrachloride formation, which is undesirable in the molten salt systems described in this study due to its corrosive nature with metal containment systems. Furthermore, the use of metal chlorides would require an additional step to separate the metal product from uranium trichloride.

For example, the uranium trichloride used in the EMT process was synthesized by researchers at ANL by preparing a vessel with molten cadmium below a pool of LiCl-KCl eutectic salt at 600°C. A porous basket containing uranium metal was suspended in the salt and rotated. Gaseous chlorine was injected into the cadmium pool, forming cadmium chloride ($CdCl_2$). The cadmium chloride rose through the cadmium layer and into the molten salt pool, where the chloride reacted with uranium in the basket to form uranium trichloride per Eq. 2.50. The cadmium metal from the reaction with uranium sank back into the cadmium pool. After the desired concentration of uranium trichloride was achieved, the reaction was stopped, and the salt product was pressure siphoned out of the vessel. [128] In spite of the separate cadmium and salt layers in this process, the LiCl-KCl-UCl_3 product still contained a low concentration of cadmium.

Other examples of metal chloride reactions with uranium metal to form uranium trichloride in molten salts have been reported in the literature, including copper chloride [129], bismuth chloride [130], and zinc chloride [131].

Pure forms of uranium chloride could be synthesized by contacting uranium metal directly with chlorine or hydrochloric gas, per the following generalized reaction mechanisms.

$$U + x/2\ Cl_2(g) \rightarrow UCl_x \qquad (2.51)$$

$$U + x\ HCl(g) \rightarrow UCl_x + x/2\ H_2(g) \qquad (2.52)$$

A challenge with the former mechanism is that chlorine gas can produce tri-, tetra-, penta-, and hexachloride forms of uranium. [33] Furthermore, the corrosive nature of chlorine could introduce contaminants into the product from interaction with materials of construction. The

formation of a reducing hydrogen gas in the latter mechanism precludes the formation of penta- and hexachloride forms of uranium; however, it does favor chlorination of uranium trichloride to the tetrachloride. [33]

Delivery of hydrogen chloride in a solid form to uranium metal can be accomplished with ammonium chloride, which sublimes at 338°C into gaseous ammonia and hydrogen chloride. This approach has a potential advantage of not requiring a gas sparging system to introduce gaseous hydrogen chloride. Researchers at Korea Atomic Energy Research Institute (KAERI) contacted uranium metal pellets with ammonium chloride under heat and observed a mixed uranium tri- and tetra-chloride product with unreacted uranium metal, despite applying a super stoichiometric amount of ammonium chloride for the given metal mass. [132] Additionally, researchers at Oregon State University and ANL contacted uranium metal with an excess of ammonium chloride to produce uranium tetrachloride. [133] The tetrachloride was separately blended with uranium metal and heated to reduce the tetrachloride to uranium trichloride per the following reaction mechanism. [33]

$$3\ UCl_4 + U \rightarrow 4\ UCl_3 \qquad \Delta G_{Rx,550C} = -410\ kJ \qquad (2.53)$$

Uranium trichloride in the EMT process and in the dissolution of used nuclear oxide fuel in molten salt systems for this study did not require isolated uranium trichloride, but rather uranium trichloride in lithium-potassium chloride eutectic or other metal chlorides. **Consequently, an objective in this study was to synthesize high-purity uranium trichloride in LiCl-KCl eutectic and sodium chloride media for use in molten salt dissolution experiments.** Specifically, uranium metal or uranium hydride were contacted with ammonium chloride in one of the identified metal chloride media under heat to produce

a molten salt solution containing uranium trichloride. Experimental observations of uranium trichloride synthesis are described in Section 7 of this study.

3. Experimental Aspects

The dissolution of nuclear research reactor fuel constituents in molten salt systems outlined in this dissertation consisted of a suite of experimental studies, each involving specialized equipment and materials suited for performance of the experiments and characterization of the products. The following highlights the primary equipment, materials, and characterization techniques used in the described foci of this study.

3.1 Equipment

3.1.1 Hot Fuel Dissolution Apparatus in the Main Cell of HFEF

A Hot Fuel Dissolution Apparatus (HFDA) was used to study the dissolution of used nuclear oxide fuels in molten salt systems. The HFDA operates in INL's Hot Fuel Examination Facility (HFEF), which is the Laboratory's premier facility for handling and examining various types of used nuclear fuels throughout the DOE complex, including research and commercial fuels. The main cell of HFEF is a rectangular shielded hot cell with an argon atmosphere, a bird's eye view of which is shown in Figure 3.1.

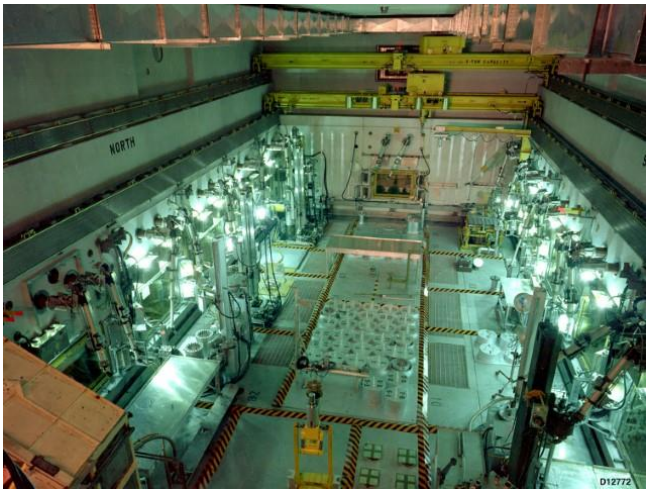

Figure 3.1. Bird's eye view of the main cell in HFEF.

The main cell of HFEF is configured with 15 workstations positioned around the perimeter of the cell's 4-ft thick concrete walls and leaded glass windows. Each workstation includes a window, two master-slave manipulators, and various electrical and gas line penetrations through the cell wall to operate equipment inside the cell. Within the main cell are overhead manipulators and cranes for material and equipment handling throughout the cell. The argon atmosphere in the cell is configured with heat removal and purification systems that maintain ambient temperature in the cell at a nominal range of 25 – 30°C with oxygen and moisture concentrations at 60 ± 40 ppm. The inert argon atmosphere facilitates the handling of pyrophoric materials, including sodium-bonded metallic fuels.

The HFDA is an existing piece of equipment located in the HFEF main cell at workstation 9M. It consists of a vertical cylindrical resistance-heated furnace that is enveloped by a steel containment with a top-loaded operating head. A picture and cross-sectional view of the HFDA are shown in Figure 3.2. A crucible assembly is positioned within the furnace to contain the molten salt. Directly above the furnace is an operating head that is fitted with five ports and a suspended set of heat shields with matching ports. The center port is fitted with a stainless-steel thermocouple well and thermocouple to monitor the melt temperature within the crucible assembly. The other four ports are configured 90 degrees apart and are available to access the melt, as needed. The right- and left-hand ports are configured with motors and rotating clamps to facilitate rotation of inserted probes or electrodes. When not in use, each of the four ports – front, back, right-hand, and left-hand – is fitted with a closed-end ceramic tube as a thermal shield plug. The outer steel containment is fitted with a gas line to provide a continuous cover of pure argon gas on the system. The HFDA is equipped with cables for connections to electrodes in each of the four ports, e.g.,

anode, cathode, reference, working, and/or counter electrodes. Electrode connections to the HFDA are accessible to instrumentation outside the HFEF main cell at workstation 9M.

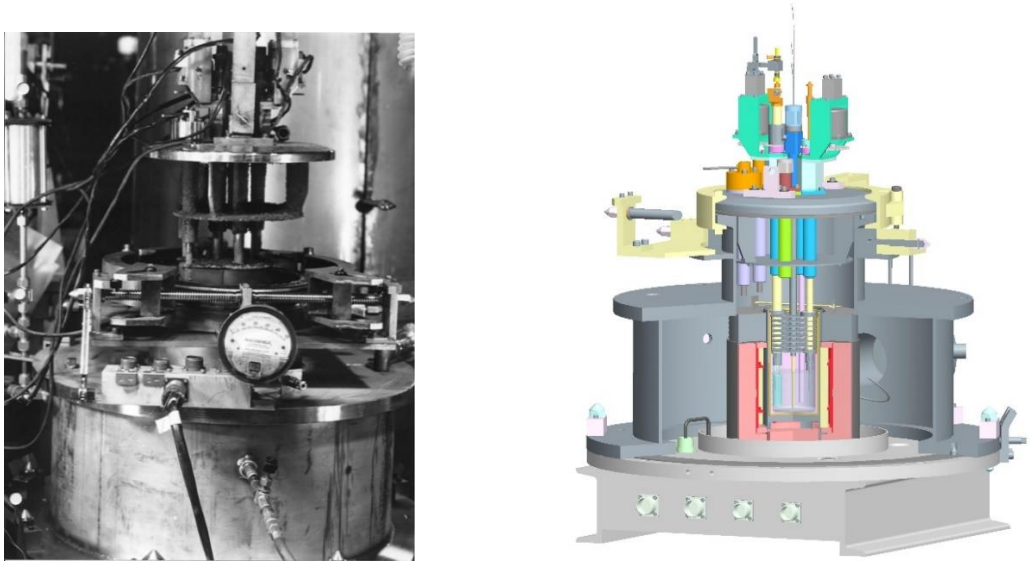

Figure 3.2. HFDA at HFEF workstation 9M (left) and sectional view (right).

Furnace, motor, electrochemical control, and data acquisition equipment for operations with the HFDA are shown in Figure 3.3. An existing instrumentation and control cabinet was used to control the HFDA furnace and rotating port motors. Electrode connections from the HFDA were wired to an electrical panel outside the HFEF 9M workstation, to which either power supplies or potentiostats were connected. A Solartron (model 1285) potentiostat was connected to the HFDA electrodes via the electrical panel to perform cyclic voltammetry. A power supply (KEPCO Bipolar Operational Power Supply / Amplifier, ±20 V ±20 A) was connected to the electrical panel for current driven operations in the HFDA. A data logger (HP 34970A, Data Acquisition / Switch Unit) and accompanying software were used to monitor and record open- and closed-circuit potentials and currents. Analytical (Mettler Toledo, PR503) and kg-scale balances were located at HFEF workstation 10M to facilitate in-cell weighing of materials.

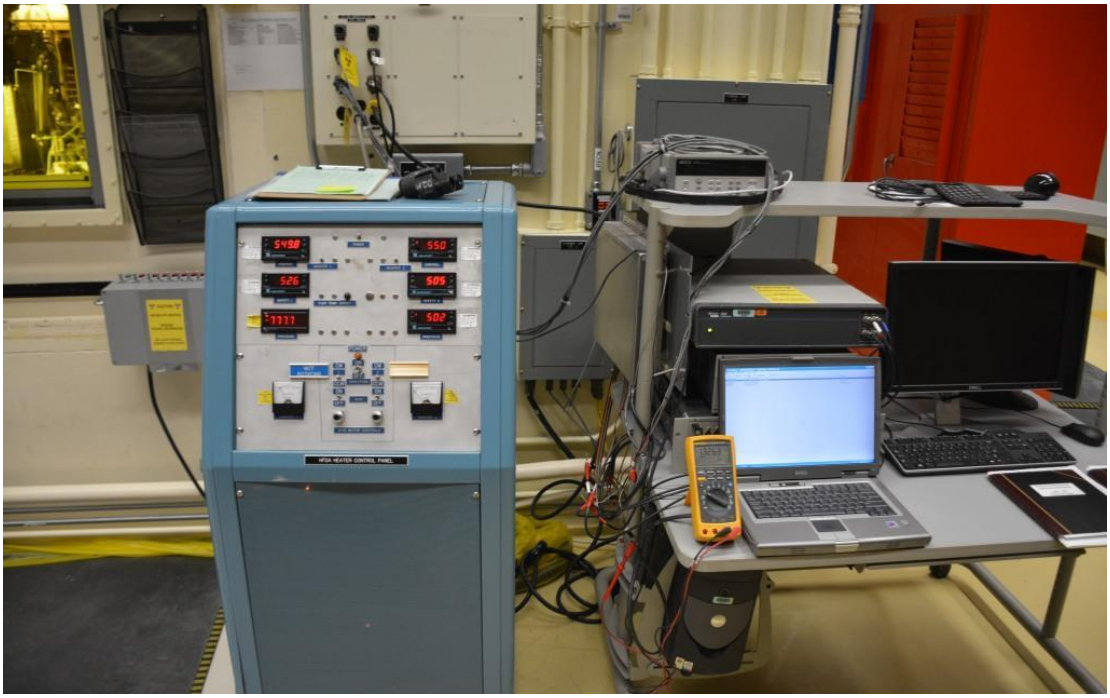

Figure 3.3. Instrumentation, control, and data acquisition equipment for HFDA operations at HFEF workstation 9M.

3.1.2 Radiological Gloveboxes

Radiological gloveboxes at INL's Fuel and Applied Science Building (FASB) and FCF were used to support the synthesis of uranium trichloride in molten salt systems. Each of these gloveboxes and their associated equipment are described below.

3.1.2.1 Fuels and Applied Science Building Glovebox

A radiological glovebox (VAC Controlled Atmosphere Systems, Vacuum Atmospheres Co.) is installed and functional in FASB for the handling of unirradiated uranium metal and other pyrophoric materials. It operates with an argon atmosphere and a purification system to maintain oxygen and moisture typically below 10 ppm. It was equipped with a horizontal tube furnace (Lindberg/Blue) and associated gas and vacuum lines to facilitate the production of uranium metal powder and uranium hydride powder from

bulk uranium metal, which were used as feed materials for the synthesis of uranium trichloride. A picture of the glovebox in FASB with the horizontal tube furnace is shown in Figure 3.4. The glovebox also contains an analytical balance (Mettler Toledo, XP1203S) for weighing materials.

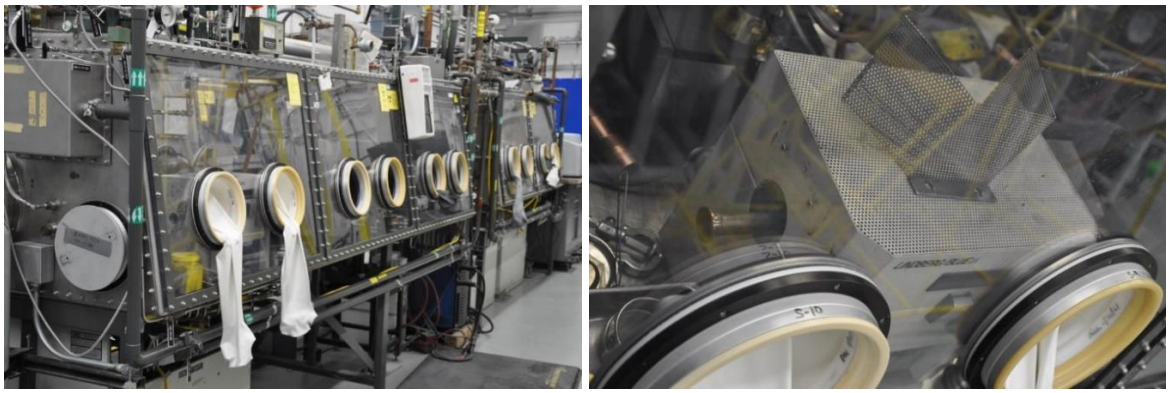

Figure 3.4. Radiological glovebox in FASB (left) with horizontal tube furnace (right) at left end of box.

3.1.2.2 Fuel Cycle Glovebox

The Fuel Cycle Glovebox (FCG) is a radiological glovebox (MBRAUN, LABmaster pro dp) that operates in FCF with an argon atmosphere and purification system that maintains oxygen and moisture typically below 20 ppm. It is equipped with a bench-top furnace (Kerr, Auto Electro-Melt Furnace, Maxi 3kg) and an analytical balance (Mettler Toledo XS1203S). The furnace is a resistance-heated jeweler-type furnace with a temperature rating of 1120°C. It contains a graphite crucible with an internal volume of 300 ml and removable insulated lid. The FCG and Kerr furnace were used in the synthesis of uranium chloride in molten salt systems. A picture of the FCG is shown in Figure 3.5.

Figure 3.5. Fuel Cycle Glovebox in FCF with bench-top furnace (right end of box).

3.1.3 Non-Radiological Gloveboxes

Two non-radiological gloveboxes were used to support this study. One glovebox (MBRAUN LABmaster dp) operates in the Water Chemistry Laboratory (WCL) at INL. It contains an argon atmosphere and purification system that maintains oxygen and moisture typically below 10 ppm. The glovebox was equipped with a box furnace (Thermo Scientific, Thermolyne) that was used for drying salts in this study. The glovebox is also equipped with an analytical balance (Mettler Toledo, ME) for weighing materials. Pictures of the WCL glovebox and box furnace are shown in Figure 3.6.

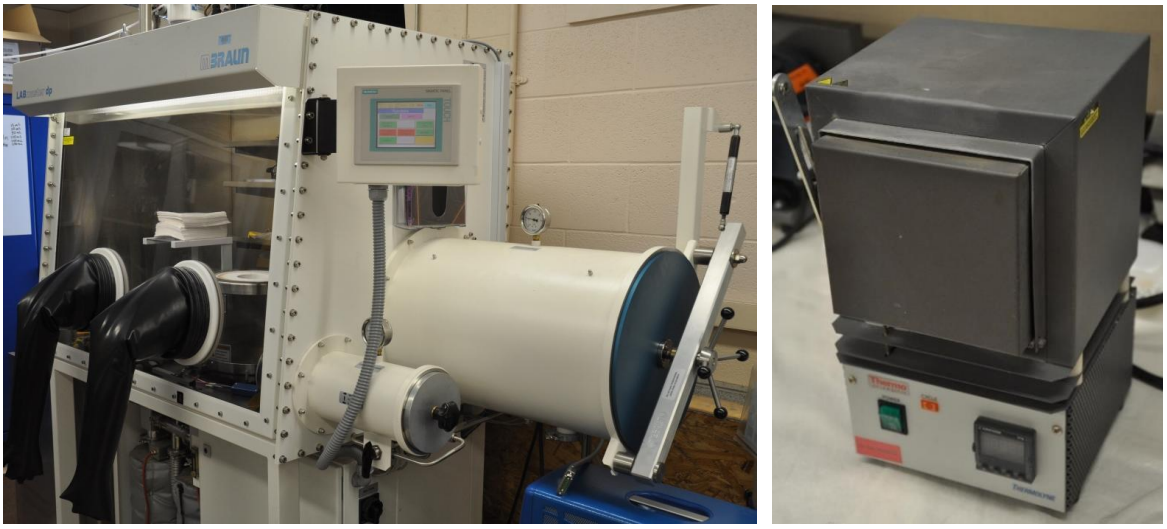

Figure 3.6. Non-radiological glovebox (left) and box furnace (right) in WCL.

The other non-radiological glovebox (MBRAUN LABmaster dp) used in this study operates in the Engineering Development Laboratory (EDL). It contains an argon atmosphere and has a purification system that maintains oxygen and moisture nominally below 20 ppm. The glovebox is equipped with a hot plate (Cole Parmer, StableTemp) and box furnace (Thermo Scientific, Thermolyne), which were used in the study on sodium deactivation. The glovebox is also equipped with a bench-top furnace (Kerr, Auto Electro-Melt Furnace, Maxi 3kg), which was used in the study on dissolution of surrogate aluminum matrix fuels. An analytical balance (Mettler Toledo, XPE1203S) is positioned in the glovebox for material weighing. A picture of the EDL glovebox and associated equipment are shown in Figure 3.7.

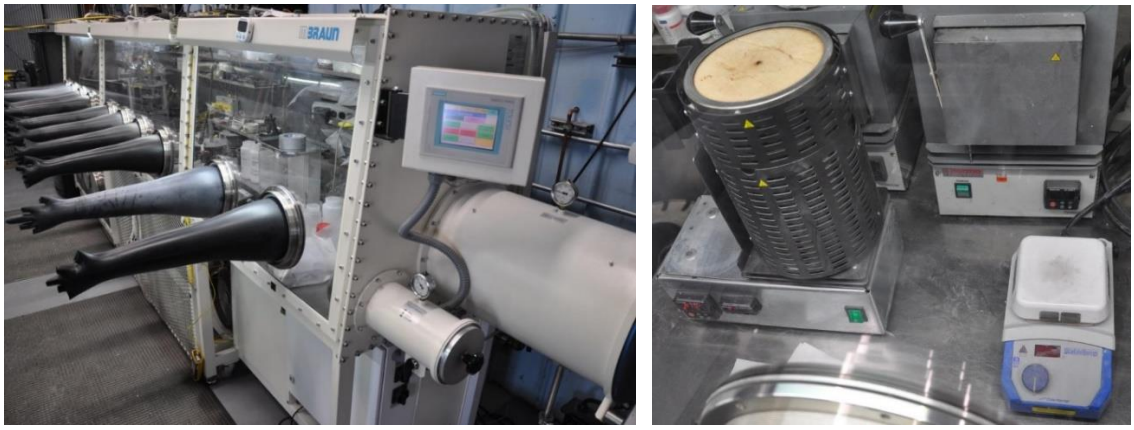

Figure 3.7. Non-radiological glovebox (left) in EDL and installed equipment (right).

3.2 Materials

As this study involves the dissolution of nuclear research reactor fuel constituents in molten salt systems, the primary materials include the solutes (fuel constituents) and solvents (salts). Each is described in turn as they apply to the different foci of this study.

3.2.1 Used Research Reactor Fuel Constituents

3.2.1.1 Degraded Experimental Breeder Reactor-II Fuel

Over the course of EBR-II's operating history, select used fuel elements from the reactor were transferred to an Alpha-Gamma Hot Cell Facility (AGHCF) at ANL for post-irradiation examinations. These examinations were destructive, involving cutting, breaching, and preparing segments of the elements for microscopic analyses. These activities were performed under a nitrogen atmosphere in the AGHCF due to the pyrophoric nature of the sodium-bonded metal fuels. Often the used EBR-II elements were cut to remove a small section of the fuel element for analysis, leaving behind an accumulated storage of exposed end pieces that required proper management. After the need for post-irradiation examinations of EBR-II fuel at the AGHCF had subsided, and after occasional losses of

atmospheric purification in the AGHCF over years of operation, inadequately sealed containers of breached EBR-II fuel were exposed to an oxidizing atmosphere. Consequently, some of the breached EBR-II degraded, likely forming oxides of uranium per the following reactions. [33]

$$U + O_2(g) \rightarrow UO_2 \qquad \Delta G_{f,25C} = -1032 \text{ kJ} \qquad (53)$$

$$3\ UO_2 + O_2(g) \rightarrow U_3O_8 \qquad \Delta G_{f,25C} = -274 \text{ kJ} \qquad (54)$$

Upon decommissioning of the AGHCF at ANL, the inventory of used EBR-II fuel stored there was shipped to INL for disposition, including the degraded (i.e., oxidized) portions. Indeed, the degraded portions were transferred to the main cell of HFEF, where they were used in the initial testing of used oxide fuel dissolution studies in molten chloride salts. A picture of the contents of one such storage container is shown in Figure 3.8.

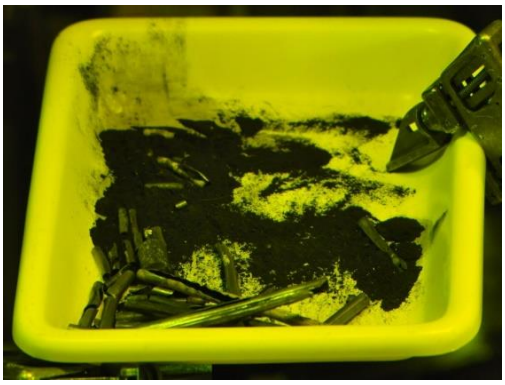

Figure 3.8. Degraded EBR-II fuel elements from AGHCF.

3.2.1.2 Belgium Reactor 3 Fuel

Belgium Reactor 3 (BR3) was the first PWR in western Europe, operating as a test reactor for prototype nuclear fuels. It was also a demonstration unit for an industrial power station and served as an education and training center for operating personal in nuclear power

plants. BR3 began operations in 1962, and it was the first PWR in Europe to be shut down in 1987. Furthermore, the reactor is the first to be decommissioned in Europe, which is ongoing and expected to be complete by the end of 2023. [134]

Over a hundred used oxide fuel elements from BR3 were acquired by the U.S. DOE for programmatic testing in the mid-1980s at INL. All but eight of the elements were used in the programmatic testing. The remaining eight elements were transferred to the main cell of HFEF, where some of the elements supported the development of the electrolytic reduction process for used oxide fuels. [44-47, 50] A typical used BR3 fuel element consisted of a 100-cm-tall UO_2 fuel column in a 0.95-cm diameter Zircaloy-4 cladding. The fuel was initially enriched in uranium-235 to 8.3 wt% and was irradiated to a mean specific burnup of 36 GWd/t. The fuel was removed from BR3 in the 1979-1980 timeframe. The make-up of a typical used BR3 fuel element is shown in Table 3.1.

Table 3.1. Constituent concentrations of typical used BR3 fuel. [50]

Rare Earths (ppm)		**Uranium/TRU (ppm)**		**Noble Metals (ppm)**		**Salt-Soluble (ppm)**	
Nd	4200	U-total	838000	Zr	3300	Cs	2500
Ce	2600	% U-234	<0.04	Mo	2600	Ba	2200
La	1300	% U-235	4.33	Ru	1200	Sr	790
Pr	1200	% U-236	0.82	Tc	540	Rb	530
Sm	830	% U-238	94.81	Pd	470	Te	490
T	560	Pu-total*	6060	Rh	280	I	indeterminate
Gd	60	Np-237	421	Cd	70	Eu	100
Dy	10	Am-241	230	Ag	45		
*Pu-total includes Pu-238, Pu-239, Pu-240, Pu-241, and Pu-242.							

Other BR3 fuel elements were subjected to a Decladding by Oxidation (DEOX) process. [135] This process involved cutting and exposing clad segments of the used BR3 fuel to oxidizing conditions at elevated temperature, i.e., 500 – 1250°C, resulting in oxidation and consequent pulverization of the UO_2 fuel matrix to U_3O_8 fine particulate, which separated readily from the cladding. The process effected the (1) decladding of a UO_2 fuel matrix from its cladding, (2) reduction of the fuel matrix particle size, and (3) separation of some volatile fission products, including iodine, ruthenium, cesium, and technetium to varying extents.

Both the UO_2 and U_3O_8 forms of used BR3 fuel were available and used in this study on dissolution of used nuclear oxide fuel in molten salt systems. In either case the BR3 fuel was separated from its cladding, crushed (or otherwise sized) as needed, and sieved, to acquire the desired particle size for dissolution testing. Pictures of a cut and declad BR3 fuel element after crushing and after a DEOX process are shown in the main cell of HFEF in Figure 3.9.

Figure 3.9. Cut (upper left) and declad BR3 fuel element by crushing (upper right) and by DEOX process (bottom).

3.2.1.3 Surrogate Materials for Used Advanced Test Reactor Fuel

As a scoping study, the dissolution of use ATR fuel was limited to non-radiological surrogates to focus on the effectiveness of removing aluminum from uranium. Specifically, neodymium metal was used as a surrogate for uranium, as it forms similar intermetallics with aluminum to that of uranium. Thus, neodymium metal powder (Alfa Aesar, 99.9%, -200 mesh, packaged under argon) was used as a surrogate for uranium metal powder in ATR fuel. Aluminum metal powder (Alfa Aesar, 99.97%, -100 mesh, +325 mesh) and foil (Alfa Aesar, 99.99%, 0.25 mm thick) were used as surrogates for the fuel matrix and cladding,

respectively. Pictures of the feedstock materials for the aluminum-matrix fuel dissolution study are shown in Figure 3.10.

Figure 3.10. Neodymium and aluminum feedstock materials for aluminum-matrix fuel dissolution study.

3.2.1.4 Bond Sodium Metal

Bond sodium in EBR-II fuel is highly radioactive from direct activation of sodium and from fission product migration into the bond sodium. Specifically, in a fast reactor natural sodium (i.e., sodium-23) undergoes two primary types of neutron activation reactions, including (n, γ) to form sodium-24 and (n, 2n) to form sodium-22. The former is short-lived with a 15-hr half-life, while the later has a 2.6-yr half-life. However, the bigger impact to radioactivity in the bond sodium is fission product migration, especially from cesium, as cesium-137 and its daughter product barium-137m are strong beta/gamma emitters with a 30-yr half-life. Thus, due to elevated radioactivity levels in bond sodium from used EBR-II fuel, non-radioactive sodium metal (Alfa Aesar, 99.8%) was used in this study for deactivation in molten salt systems. A picture of the sodium metal feed stock used in this study is shown in Figure 3.11.

Figure 3.11. Sodium metal used in deactivation study.

3.2.2 Salts

The salts used in the various experiments of this study are divided between reactant and non-reactant salts. The reactant salts are those that participate in the primary reactions of a given experiment, while the non-reactant salts do not. However, the non-reactant salts function as reaction media, diluents, and/or melting point suppressants. The following describes the reactant and non-reactant feedstock salts used in this study.

3.2.2.1 Reactant Salts

The reactant salt for dissolution of used nuclear oxide fuels in a molten salt system was a ternary salt of lithium chloride / potassium chloride eutectic (44/56 wt%) with uranium trichloride. The ternary salt was synthesized by researchers at ANL in a process using chlorine gas, cadmium metal, and uranium metal in the lithium chloride / potassium chloride eutectic salt, as described in section 2.6. The product was a ternary salt with a uranium mass fraction of roughly 50 wt%. The synthesized ternary salt was triple distilled to remove excess cadmium. Nevertheless, the cadmium content in the ternary salt feedstock for this

study was approximately 1 wt%. A picture of synthesized ternary salt used in this study is shown in Figure 3.12.

Figure 3.12. Ternary salt used in the molten salt dissolution of used nuclear oxide fuels.

The primary reactant salt in the aluminum-matrix fuel dissolution study, the sodium deactivation study, and the uranium trichloride synthesis study was ammonium chloride (Alfa Aesar, 99.999%, Puratronic). Ammonium chloride is hygroscopic and was not offered in an anhydrous form from the supplier. Consequently, the ammonium chloride was dried and sieved to the desired particle using a box heater in the WCL glovebox. Specifically, the ammonium chloride was loaded into trays and heated to 140°C for at least one overnight period prior to crushing and sieving. Pictures of ammonium chloride loaded in trays before and after drying are shown in Figure 3.13 along with equipment used for grinding and sieving. Ammonium bromide was also used as a reactant salt in the aluminum-matrix fuel dissolution study. It was dried, crushed, and sieved similarly.

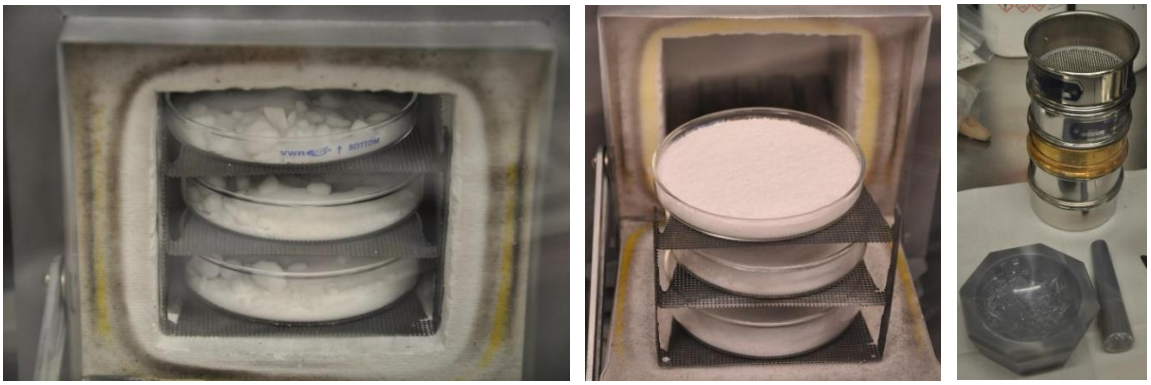

Figure 3.13. Ammonium chloride before (left) and after (center) drying in box furnace with grinding and sieving equipment (right).

Iron (II) chloride (Sigma Aldrich, 99.99%, anhydrous, -10 mesh beads, ampouled under argon) was a reactant salt used in the deactivation of sodium metal. Because the iron chloride was purchased as anhydrous and was packaged under argon, drying of the salt prior to use was not necessary. A picture of iron chloride used in the deactivation of sodium metal is shown in Figure 3.14.

Figure 3.14. Anhydrous iron chloride used in sodium metal deactivation study.

3.2.2.2 Non-Reactant Salts

Non-reactant salts used in the oxide fuel dissolution study included lithium chloride – potassium chloride eutectic (Sigma Aldrich, 99.99%, anhydrous, -10 mesh beads, ampouled under argon). Those used in the aluminum-matrix fuel dissolution study included lithium chloride (Alfa Aesar, 99.9%, ultra-dry) and lithium bromide (Alfa Aesar, 99.9%, ultra-dry). The same lithium chloride – potassium chloride eutectic salt used in the oxide fuel dissolution study was also used in the uranium trichoride synthesis study along with sodium chloride (Sigma Aldrich, 99.999%, anhydrous, -10 mesh beads, ampouled under argon). Each of these non-reactant salts was purchased in an anhydrous form and packaged in glass ampoules under argon gas, as shown in Figure 3.15 for the described sodium chloride. Thus, no additional drying of these non-reactant salts was necessary.

Figure 3.15. Anhydrous sodium chloride used in synthesis of uranium trichloride.

3.3 Characterization Techniques

Characterization of the different experiments and products in this study included electrochemical and material characterization techniques. The former provided real-time characterization of the in situ process, while material characterizations techniques applied to intermediate and final products. The following further describes aspects of these techniques and how they were applied in this study.

3.3.1 Electrochemical Techniques

The primary electrochemical or electroanalytical techniques used in this study were cyclic voltammetry, chronoamperometry, and chronopotentiometry. All were applied with a potentiostat and an electrochemical cell consisting of a working electrode, a counter electrode, and a reference electrode in contact with an electrolyte. For cyclic voltammetry, the potentiostat was programmed to ramp the potential between a working electrode and reference electrode from an open circuit potential to a selected switching potential or peak potential at a specified constant rate, called a sweep rate. The direction of potential was then reversed and returned to its starting (i.e., open circuit) potential. The initial potential can be anodic or cathodic, depending on the system and desired output. A typical time trace of potential for a simple cyclic voltammetry run is depicted in Figure 3.16. The current that is generated from the cyclic voltammetry cell is plotted against the potential to generate a cyclic voltammogram. A typical cyclic voltammogram for a reversible reaction in a simple electrochemical cell is shown in Figure 3.17. Cyclic voltammetry is useful in determining potentials at which electrochemical reactions occur and comparing them to those expected from Nernst equation. [32]

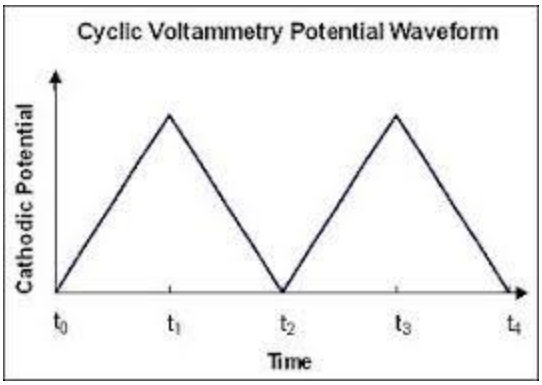

Figure 3.16. Time trace of potential in a cyclic voltammetry run.

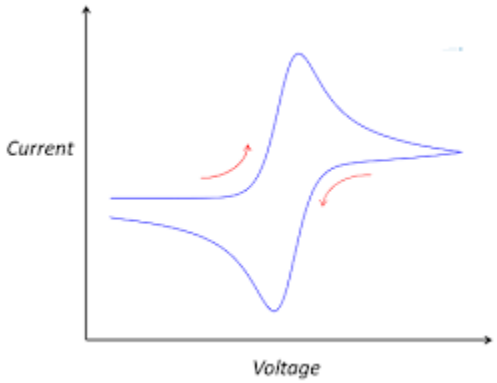

Figure 3.17. A prototypic cyclic voltammogram for a reversible reaction in a simple electrochemical cell.

Chronopotentiometry is performed using a similar electrochemical arrangement as that described for cyclic voltammetry, except that the cell is stepped to a specified potential as opposed to a sweep rate. The developed current is monitored over time. Analogously, chronopotentiometry is applied by stepping the cell to a specified current and monitoring the resultant potential over time. Chronopotentiometry and chronoamperometry are useful in observing changes in reactions occurring in an electrochemical cell over time. [32]

The described electrochemical techniques were used in the studies of oxide fuel dissolution in molten salt systems and the synthesis of uranium trichloride.

3.3.2 Material Characterization Techniques

3.3.2.1 Elemental and Isotopic Analyses in the Analytical Laboratory

The Analytical Laboratory (AL) at INL is equipped with instruments to perform elemental and isotopic analysis of radiological and non-radiological samples, including remotely handling samples. In fact, air-atmosphere hot cells are installed in AL to receive and handle highly radioactive samples from FCF via an underground pneumatic transfer system. HFEF is connected to FCF with a similar pneumatic transfer system. Thus, remotely handled samples from HFEF are transferred to the AL hot cells via FCF. In the AL hot cells, samples are weighed and dissolved, from which diluted samples are taken for elemental and isotopic analyses outside of the shielded cells.

Elemental analyses were performed via Inductively Coupled Plasma – Optical Emission Spectroscopy (ICP-OES). Isotopic analyses were performed via Inductively Coupled Plasma – Mass Spectroscopy (ICP-MS) and gamma spectroscopy. ICP-OES and ICP-MS both function by injecting a dissolved sample solution into an argon plasma. In the case of ICP-OES, outer shell electrons of sample elements are excited as they pass through the plasma and then return to ground state, which is accompanied by the emission of photons of light with energies characteristic of specific elements. In the case of ICP-MS, the ionized sample elements from the plasma are separated by mass-to-charge ratios via rapidly switched radiofrequency fields along a quadrupole detector. In the case of gamma spectroscopy, gamma ray intensities from radioactivity in a sample are measured according to their energies, which are characteristic of specific radioisotopes. Each of these techniques was applied to intermediate and final product samples from the used oxide fuel dissolution, aluminum-matrix fuel dissolution, and uranium trichloride synthesis studies.

3.3.2.2 X-Ray Diffraction

Two X-ray diffractometers were used for sample analysis – one in FASB for radiological samples and another in the Center for Advanced Energy Studies (CAES). X-ray diffraction (XRD) allows for rapid non-destructive analysis of a multi-component sample mixture with relatively easy sample preparation, producing distinctive diffraction patterns for comparison to extensive databases for crystalline phase identification. Radioactive samples of synthesized uranium trichloride were prepared in a FASB argon-atmosphere glovebox by placing crushed sample particles onto a tray that was sealed with a domed cover, thereby protecting the sample from moisture absorption. The tray was removed and placed in a PANalytical (AERIS) X-ray diffractometer in FASB, as shown in Figure 3.18. Non-radioactive samples from aluminum-matrix fuel dissolution and sodium deactivation experiments were subjected to XRD (Rigaku SmartLab) in CAES, as shown in Figure 3.18.

Figure 3.18. PANalytical X-ray diffractometer in FASB (left) and Rigaku X-ray diffractometer in CAES (right).

3.3.2.3 Transmission Electron Microscopy

A Titan Themis 200 Probe Cs Corrected FEG Scanning Transmission Electron Microscope (STEM) is installed and operated in the Irradiated Material Characterization Laboratory (IMCL) at INL. The microscope has a point resolution as low as 0.08 nm. It is also equipped with energy-dispersive x-ray spectroscopy (EDS) and electron energy loss spectroscopy (EELS), enabling mapping down to the atomic scale. The Titan STEM, which is shown in Figure 3.19, was used for imaging and spectroscopy of synthesized uranium trichloride samples in this study.

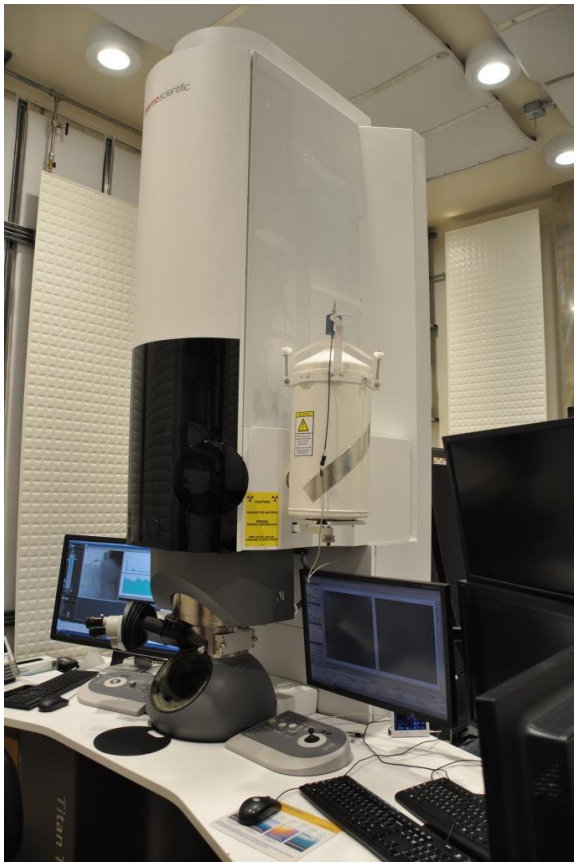

Figure 3.19. Titan STEM in IMCL for analysis of synthesized uranium trichloride samples.

4. Dissolution of Used Nuclear Oxide Fuels in Molten Chloride Salt Systems

Forthcoming in *Nuclear Technology*, "Parametric Study of Used Nuclear Oxide Fuel Constituent Dissolution in Molten LiCl-KCl-UCl_3"

4.1 Objectives

The objective of this study was to investigate the parameters and reaction mechanisms associated with dissolution of used nuclear oxide fuel constituents in LiCl-KCl-UCl_3. Specifically, a series of fundamental studies was performed with fast and thermal test reactor oxide fuels from EBR-II and BR3, respectively, to identify the effects of operating parameters on fuel constituent dissolution. The operating parameters included preconditioning and in situ conditioning of the oxide fuels, along with temperature and composition of the molten salt.

4.2 Experimental Aspects

4.2.1 Approach

The approach for this work involved a series of three bench-scale experimental studies with each building progressively upon results from its predecessor study. First, a scoping study was performed to investigate the successive dissolution of constituents from three different forms of used oxide fuels in a common pool of LiCl-KCl-UCl_3 at 500°C. After identifying the impacts of oxide fuel preconditioning and a reduced phase in the fuel matrix on rate and extent of fuel constituent dissolution from the scoping study, a second study was performed to investigate an electrolytic approach for generating reducing conditions in the fuel matrix and its consequent effect on dissolution of fuel constituents. The effects of system temperature and uranium trichloride concentration on fuel constituent

dissolution were also included in the electrolytic dissolution study. A third study was then performed to investigate a chemical-seeded approach to fuel constituent dissolution by loading uranium metal particulate directly into oxide fuel particulate to achieve reducing conditions in the fuel matrices. Investigation into the effect of system temperature on fuel constituent dissolution continued in the chemical-seeded study.

Each study involved preparing a 400 – 500 ml pool of LiCl-KCl-UCl_3. For each study, permeable steel baskets containing uranium metal, or a tantalum rod to which uranium metal was electrotransported, were immersed in the salt pool to ensure reducing conditions in the salt system. Separate permeable steel baskets, containing used oxide fuel particulate, were also immersed in the salt pool from the first two studies, initiating the dissolution process. The baskets in the third study contained used oxide fuel in combination with uranium metal particulate. An Ag/AgCl reference electrode was suspended in the salt pool, against which open-circuit and closed-circuit potentials of the baskets and other working electrodes were measured. Salt samples were taken at specified time intervals following immersion of an oxide fuel basket and after various parameter adjustments including basket rotation, electrical contacting, temperature changes, uranium trichloride concentration changes, and chemical seeding. After each study, the baskets were removed and subjected to reduced pressure and elevated temperature to distill away salt adhering to the fuel. Samples of the post-test fuel were taken and subjected to analysis along with pretest fuel samples and salt samples from each study to determine the extent of fuel constituent dissolution and the effects of parameter adjustments. Salt and fuel samples were subjected to elemental and isotopic analyses via ICP-OES, ICP-MS, and gamma spectroscopy. Table 4.1 shows a summary of test conditions for the series of progressive studies.

Table 4.1. Summary of test conditions for series of progressive studies.

run	[U] as UCl_3 in LiCl-KCl	Fuel loading		DU metal mass	Temp.
	(wt%)	type	mass (g)	(g)	(°C)
1. Scoping Study					
1.1	9	Oxidized EBR-II fuel	24.7	50	500
1.2		BR3 fuel	28.3		
1.3		Voloxidized BR3 fuel	28.7		
2. Electrolytic Dissolution Study					
2.1	6, 19	Pre-heated BR3 fuel	30.6	59.9	500, 650
3. Chemical-Seeded Dissolution Study					
3.1	19	Pre-heated BR3 fuel + uranium metal particulate	24.4 (oxide) 16.5 (metal)	Seeded in each fuel loading, then deposited on Ta rod	650, 725, 800
3.2			20.2 (oxide) 14.3 (metal)		
3.3			13.1 (oxide) +16.5 (metal)		

4.2.2 Test Specific Equipment

The series of three studies was performed in the HFDA with accompanying instrumentation and controls (see Section 3.1.1). Figure 4.1 shows a simplified electrochemical cell configuration for the series of fuel dissolution studies. Unless stated otherwise, electric potentials are reported relative to an Ag/AgCl reference electrode.

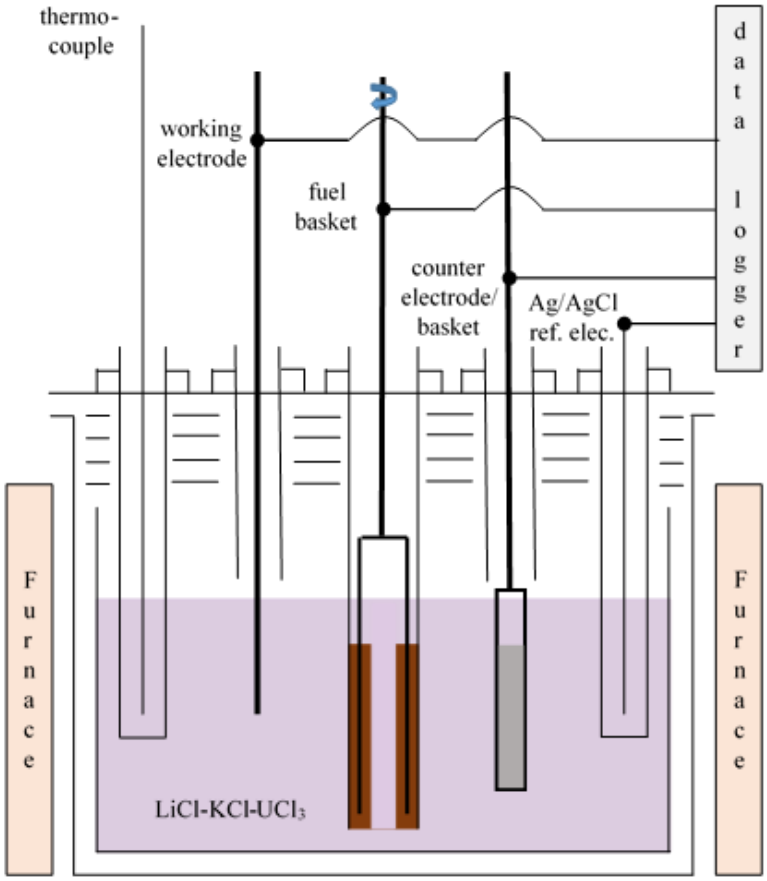

Figure 4.1. Simplified electrochemical cell configuration for series of fuel dissolution studies.

In this series of studies, two distillation apparatuses were used for the post-dissolution baskets. Each involved sealing a set of baskets inside a retort assembly, which was then positioned inside of a clamshell furnace. One of the furnaces was capable of operations to 1350°C and the other to 1100°C. The retort assembly was connected to a TriScroll (Agilent) vacuum pump, which was capable of lowering pressure below 100 mTorr.

4.2.3 Test Specific Materials

Driver fuel elements from EBR-II fuel consisted primarily of a binary metal alloy rod of high-enriched uranium-10% zirconium that was bonded with sodium metal to steel

cladding. Over the operating life of EBR-II, numerous driver fuel elements were breached to sample and examine post-irradiated fuel specimens (upwards of 20% burnup) using a variety of methods within various facilities. Many of the breached elements were consequently exposed to oxidizing atmospheres over time, causing the fuel to degrade and form a dark finely divided particulate that readily separated from the cladding. Degraded EBR-II driver fuel was collected and transferred to the HFEF main cell, where portions were sieved and particles greater than 0.045 mm were used in the initial scoping study. A picture of the degraded EBR-II driver fuel is shown in Figure 4.2.

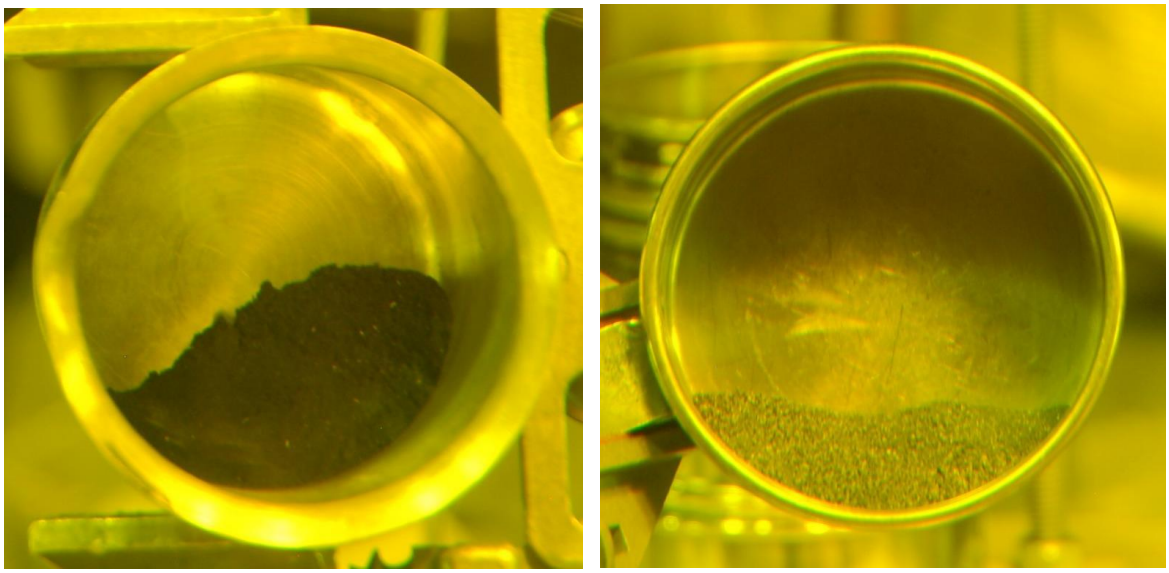

Figure 4.2. Pictures of crushed and sieved oxidized EBR-II driver fuel (left) and BR3 fuel (right) used in fuel dissolution studies.

Fuel elements from BR3 were also used in this study. The BR3 fuel was a low-enriched UO_2 fuel from a PWR, as described in Section 3.2.1.2. Some of the BR3 fuel elements were previously subjected to a DEOX process, pulverizing the UO_2 fuel matrix into U_3O_8 fine particulate which separated readily from the cladding. [135]

Both the UO_2 and U_3O_8 forms of used BR3 fuel were used in the scoping study. To acquire the desired particle size for the study, both forms of BR3 fuel were separated from their respective cladding, crushed (as needed), and sieved. Prior to sieving, other portions of BR3 fuel were preheated to 1200°C to agglomerate the material and acquire particles greater than 0.045 mm for the electrolytic and chemical-seed dissolution studies. Figure 4.2 shows a picture of crushed and sieved BR3 fuel.

The uranium trichloride used in this series of studies was synthesized as a ternary salt mixture with lithium chloride – potassium chloride eutectic by ANL researchers, as described in Section 2.6. [128] The mass fraction of uranium, as UCl_3, in the synthesized ternary salt mixture was approximately 50 wt%. The synthesized ternary salt was blended with anhydrous lithium chloride – potassium chloride eutectic (Sigma Aldrich, 99.99%, 44 wt% LiCl) to prepare the desired uranium concentration for the runs (see Table 4.1).

Depleted uranium metal was used in various forms to establish reducing conditions within the salt systems and oxide fuel loadings (see Table 4.1). Specifically, uranium metal dendrites were used in the initial scoping study, while a combination of dendrites and chopped uranium metal rod was used in the electrolytic dissolution study. For the final study, uranium metal particulate was used as a chemical seed in the fuel matrix. The uranium metal particulate was prepared by a hydride-dehydride process and sieved below a 50-mesh particle size.

4.3 Calculations

The dissolution of used nuclear oxide fuel constituents in LiCl-KCl-UCl_3 involves a complex mixture of multiple species and phases, including oxides, chlorides, metals, and combinations thereof. Thus, a chemical equilibrium model based on thermodynamic

stabilities was created to assess product compositions as a function of temperature for a given quantity of feed materials. Commercially available software, HSC Chemistry 8, [33] was used to perform such calculations with a Gibbs energy minimization model, which is based on prior work by White et al. [136] The model was applied separately to predominant alkali, alkaline earth, lanthanide (III), and transuranium (III) metal oxides in used nuclear fuel and assumed unit activities and ideal mixing. (Note: Trivalent lanthanide and transuranium metal oxides, as opposed to tetravalent metal oxides, were used in the model, because the trivalent forms are more stable in the reducing conditions imposed on the system.) Each model run identified the preferential formation of uranium (III) oxychloride in the presence of excess uranium trichloride to facilitate dissolution of the select fuel constituent groups. Accordingly, Table 4.2 shows the postulated reaction mechanisms and associated Gibbs free energies of reaction as a function of temperature for dissolution of select groups of fuel constituents.

Table 4.2. Postulated reaction mechanisms and Gibbs free energies of reaction for dissolution of representative fuel constituents in LiCl-KCl-UCl_3. [33]

Eq.	Reaction Mechanism	Gibbs Free Energy of Reaction (kJ)			
		500°C	650°C	725°C	800°C
4.1	$Cs_2O + UCl_3 \rightarrow UOCl + 2\ CsCl$	-504	-501	-503	-505
4.2	$BaO + UCl_3 \rightarrow UOCl + BaCl_2$	-266	-265	-264	-264
4.3	$Nd_2O_3 + 3\ UCl_3 \rightarrow 3\ UOCl + 2\ NdCl_3$	-159	-156	-154	-157
4.4	$Pu_2O_3 + 3\ UCl_3 \rightarrow 3\ UOCl + 2\ PuCl_3$	-142	-139	-138	-141

4.4 Results and Discussion

4.4.1 Scoping Study

For the scoping study, a molten pool of LiCl-KCl-UCl_3 at 500°C with a uranium mass fraction of 9 wt% was prepared in an alumina crucible inside the HFDA. Depleted uranium metal dendrites were loaded into an annular permeable stainless-steel basket. The basket was formed from perforated 6-mm and 19-mm diameter tubes wrapped with 325 x 325 stainless-steel mesh and welded to a steel bottom ring. The upper end of the basket was open for material loading and configured to an extension rod for suspension in the salt pool. Cyclic voltammetry was performed on the pretest salt with a 1-mm diameter stainless-steel wire suspended in the salt as the working electrode, the uranium metal loaded basket as the counter electrode, and an Ag/AgCl reference electrode. Cyclic voltammetry identified a relative uranium reduction potential of -1.32 V and stainless-steel oxidation above -0.6 V.

Degraded EBR-II driver fuel was loaded into another permeable annular basket, immersed in the salt, and periodically rotated at ~120 rpm to facilitate salt flow through the

fuel bed. Salt samples were taken before and 1, 3, and 9 hours after immersion of the basket, which exhibited a steady open-circuit potential of -1.2 V. The fuel basket was then electrically connected to the uranium metal loaded basket for an overnight period, during which time the fuel basket and uranium metal basket potentials slowly merged at approximately -1.3 V. An induced current of several milliamperes was observed, yielding a total integrated current of 0.15 ampere hours. After electrically connecting the baskets for a total of 24 hours, a final salt sample was taken, and the basket was removed.

A similar approach was used on the second annular basket loaded with crushed BR3 fuel. Salt samples were taken 1, 3, and 9 hours after immersion of the basket, which exhibited a steady open-circuit potential of -0.8 V. The fuel basket was then electrically connected to the uranium metal loaded basket for an overnight period, during which time the fuel basket and uranium metal basket potentials slowly merged at approximately -1.3 V. An induced current of several milliamperes was observed, yielding a total integrated current of 0.18 ampere hours. After electrically connecting the baskets for a total of 24 hours, another salt sample was taken. An additional salt sample was taken after 120 hours of accumulated run time with intermittent electrical connections between the baskets.

The third run was performed similarly to the previous run with voloxidized BR3 fuel in lieu of crushed fuel. Notable differences were the open and closed-circuit responses. The open circuit potential of the fuel basket was approximately -0.4 V over the first 9 hours. The closed circuit exhibited an initial current spike of nearly 500 milliamperes, which gradually subsided to several milliamperes, yielding a total integrated charge of 0.56 ampere hours. Salt samples were taken 1, 3, 9, 24, 32, and 50 hours after basket immersion. Figure 4.3 shows the post-dissolution baskets.

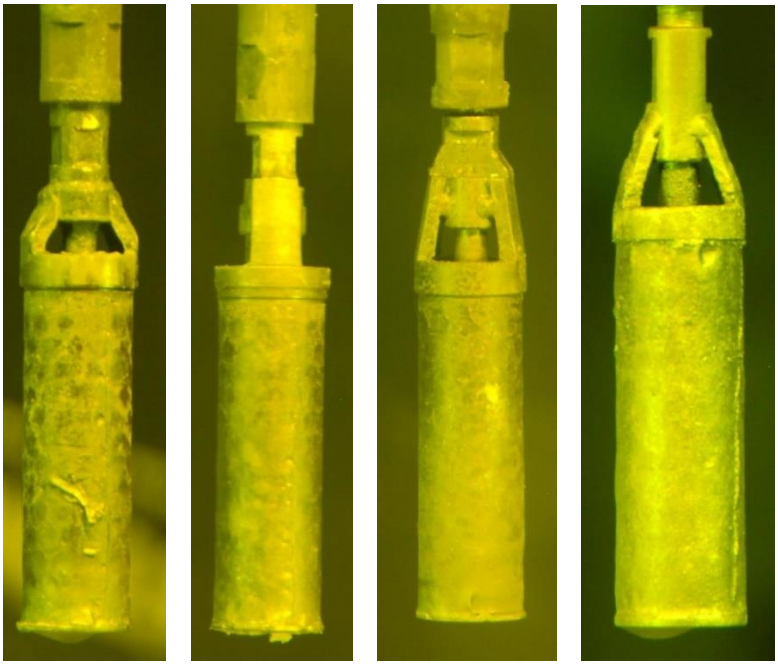

Figure 4.3. Post-dissolution baskets (left to right) for runs 1.1, 1.2, and 1.3, and uranium metal basket.

The post-test oxide fuel baskets were collectively subjected to 1350°C and a reduced pressure below 100 mTorr in a distillation apparatus to distill away salt from the baskets and fuel. The fuel was separated from each basket, and random grab samples were taken for analysis. Table 4.3 shows salt sample analysis results for the series of three runs, and Table 4.4 shows the pretest and post-test fuel samples. For brevity, the salt and fuel sample analysis results are grouped into alkali (Cs-133/135/137 and Rb-85/87), alkaline earth (Ba and Sr), lanthanide (m/z-139 – 154), and transuranium (m/z-237, 239 – 244) constituents in addition to total uranium (U-234/235/236/238) and the U-235 fraction.

Table 4.3. Consolidated results of salt sample analyses for runs 1.1, 1.2, and 1.3.

Sample		**Alkali (ppm)**	**Alkaline earth (ppm)**	**Lanth -anide (ppm)**	**Trans-uranium (ppm)**	**U (ppm)**	***U-235 (%)***
hour	**description**						
Run 1.1							
0	Pre-test	15	26	22.3	15.6	98300	*0.356*
1	Basket rotation	97.7	85.2	261	98.1	99700	*6.28*
3	Basket rotation	98.3	97	302	176	106000	*8.92*
9	Basket rotation	96.5	81.5	291	117	95800	*5.96*
24	Cross-connect	130	85.8	283	110	91200	*5.08*
33	Cross-connect	95.8	95.8	325	151	96900	*7.42*
Run 1.2							
1	Basket rotation	104	94.5	312	144	95100	*7.39*
3	Basket rotation	102	93.6	304	131	90900	*6.38*
9	Basket rotation	97.9	96.5	313	144	92700	*6.93*
24	Cross-connect	107	93.4	321	150	91700	*6.80*
33	Cross-connect	106	96.9	307	140	91700	*7.04*
120	Cross-connect	114	102	321	152	90000	*7.06*
Run 1.3							
1	Basket rotation	126	113	330	172	108000	*10.5*
3	Basket rotation	138	132	322	159	95800	*8.00*
9	Basket rotation	136	133	326	169	103000	*8.98*
24	Cross-connect	147	143	329	158	94400	*7.27*
32	Cross-connect	147	144	340	169	92700	*7.50*
50	Cross-connect	146	145	362	194	102000	*9.45*

Table 4.4. Consolidated results of fuel sample analyses for runs 1.1, 1.2, and 1.3.

ppm	**Run 1.1**		**Run 1.2**		**Run 1.3**	
	Pre-test	**Post-test**	**Pre-test**	**Post-test**	**Pre-test**	**Post-test**
Alkali	2815	13	3100	2430	1019	63.9
Alkaline earth	2295	149	3580	2720	2150	875
Lanthanide	9910	600.9	11970	10300	7310	6297
Transuranium	6820	577	8060	6500	5340	4680
Uranium	758000	759000	846000	862000	805000	864000
U-235 (iso%)	*57.4%*	*30.2%*	*3.39%*	*4.42%*	*4.93%*	*5.50%*

The peak and integrated currents generated by electrically cross-connecting the first oxide fuel basket with the uranium metal basket suggested that there may have been some higher uranium oxides (i.e., UO_{2+}) present in the degraded EBR-II fuel. Similar currents were observed in the second run, while those in the third run were substantially higher owing to a predominant presence of U_3O_8 in the voloxidized BR3 fuel. The observed currents were consistent with the change in uranium fractions for the pretest and post-test fuels (see Table 4.4), which exhibited modest increases for the first two runs and a substantial increase in the third.

The fuel sample analysis results (see Table 4.4) revealed a stark contrast in the extents of fuel constituent dissolution, determined by ratioing the differences in pretest and post-test constituent concentrations to those in the respective pretest fuels. Table 4.5 shows the extents of alkali, alkaline earth, lanthanide, and transuranium constituent dissolution in molten salt for runs 1.1, 1.2, and 1.3.

Table 4.5. Extents of alkali, alkaline earth, lanthanide, and transuranium constituent dissolution in molten salt from runs 1.1, 1.2, and 1.3.

	Run 1.1	**Run 1.2**	**Run 1.3**
Alkali	99.5%	21.6%	93.7%
Alkaline earth	93.5%	24.0%	59.3%
Lanthanide	93.9%	14.0%	13.9%
Transuranium	91.5%	19.4%	12.4%

The changes in U-235 fractions in the pretest and post-test fuel samples were astonishing, dropping from 57.4% to 30.2% in the EBR-II fuel. This drop in U-235 fraction for the EBR-II fuel corresponded to an increase of the U-235 fraction in the salt from 0.356% to 7.42%. Accordingly, the U-235 fractions in the crushed and voloxidized BR3 fuels from the second and third runs rose from 3.39% to 4.42% and 4.93% to 5.50%, respectively.

The salt sample analysis results (see Table 4.3) were consistent with the pretest and post-test fuel sample analyses, where the dissolution of fuel constituents from the respective fuels was manifest by rising constituent concentrations in the salt phase. The salt sample analysis results also provided information regarding the rate of fuel constituent dissolution. Figure 4.4 shows a plot of fuel constituent concentrations in the common salt pool as a function of accumulated run time for the three runs. The dissolution of fuel constituents from the degraded EBR-II fuel appeared to stabilize after 3 hours, whereas the same exhibited a gradual increase over their respective 120-hour and 50-hour run times for the crushed and voloxidized BR3 fuels, respectively.

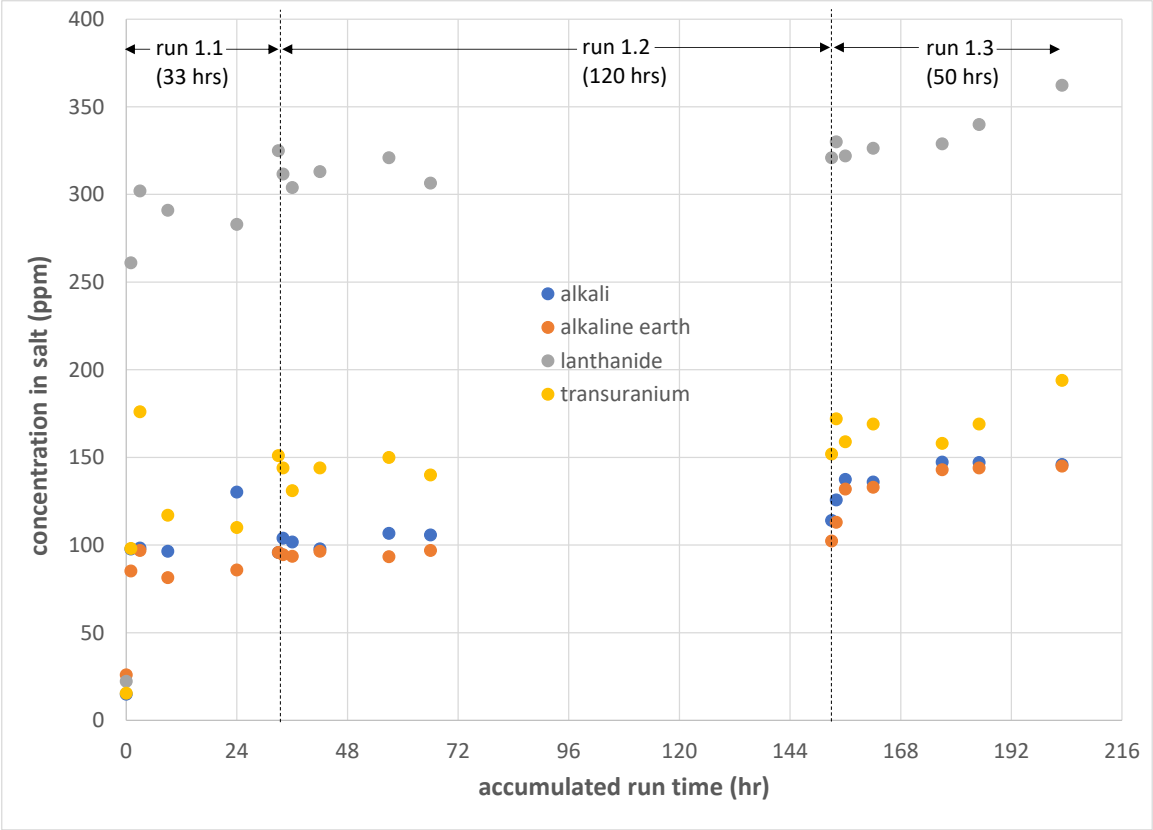

Figure 4.4. Plot of fuel constituent concentration in salt phase versus accumulated time for runs 1.1, 1.2, and 1.3.

At the beginning of the first run, the open circuit potential (-1.2 V) of the degraded EBR-II fuel was substantially more cathodic than those (-0.8 V and -0.4 V, respectively) for the second and third runs. This observation led our team to question the assumption that the degraded EBR-II fuel was fully oxidized. Consequently, an additional sample of the degraded EBR-II fuel feedstock was taken and subjected to metal and oxide phase separation by contacting the fuel sample with elemental bromine in an ethyl acetate medium. The bromine dissolved the metals in the fuels sample, leaving the oxide compounds in an insoluble solid phase. The insoluble solids were separated from the ethyl acetate solution by multiple centrifuging, decanting, and washing evolutions. Each phase was then analyzed separately for constituent inventories. Researchers at ANL developed the technique to

separate metal and oxide phases in a fuel sample, based on previous work by Brunzie et al. and Ashbrook et al. [105-106] The technique has been validated in a hot cell analytical laboratory at INL for the separation of uranium metal and uranium oxide, and it has been used in previous studies to assess the extent of uranium oxide reduction in reduced fuel samples. [44-46, 49-51] When the prescribed technique was applied to the degraded EBR-II fuel sample, it yielded a uranium metal fraction of 31%.

The uranium metal fraction of the degraded EBR-II fuel was remarkably similar to the 29% uranium metal fraction in the previously cited study with MOX fuel. [51] In both cases, more than 90% of the alkali, alkaline earth, lanthanide, and transuranium constituents dissolved into their respective pools of molten LiCl-KCl-UCl_3. The substantial presence of uranium metal in the fuel matrix played a prominent role in fuel constituent dissolution, based on observations from the partially reduced MOX and degraded EBR-II fuel runs, which stood in stark contrast to crushed and voloxidized BR3 fuels. This prompted a closer look at reaction mechanisms between the oxide, chloride, and metal phases of uranium.

Uranium dioxide was not expected to interact appreciably with uranium trichloride. Chemical equilibrium modeling of a LiCl-KCl-UCl_3-UO_2 system revealed some formation of uranium oxide chlorides under ideal conditions per the following mechanism, but it is not a thermodynamically spontaneous reaction. [33]

$$UO_2 + UCl_3 \rightarrow UOCl + UOCl_2 \qquad \Delta G_{Rx,500C} = +45.1 \text{ kJ} \qquad (4.5)$$

In contrast, chemical equilibrium modeling of a LiCl-KCl-UCl_3-UO_2-U system revealed the formation of uranium (III) oxychloride per the following thermodynamically favored mechanism. [33]

$$3\ UO_2 + 2\ UCl_3 + U \rightarrow 6\ UOCl \quad \Delta G_{Rx,500C} = -26.2\ kJ \qquad (4.6)$$

The above mechanism creates a system in which uranium in the salt phase (UCl_3) has the same valency as the uranium in the solid oxychloride phase (UOCl), making it more susceptible to uranium ion exchange between the phases than if the two phases exhibited different valencies. Thus, the mechanism in Eq. 4.6 provides a reasonable explanation for the appreciable blending of uranium isotopes between the degraded EBR-II fuel and the molten salt in the first dissolution run. Furthermore, the mechanism in Eq. 4.6 could explain the more rapid and appreciable dissolution of fuel constituents from the fuel matrix to the salt phase, as a UO_2 matrix becomes more diffusive in the presence of excess uranium trichloride and uranium metal, per the mechanism in Eq. 4.6, as opposed to less diffusive in the absence of uranium metal per the mechanism in Eq. 4.5.

Synthesis of uranium (III) oxychloride from a stoichiometric composition of uranium (IV) oxychloride, uranium dioxide, and uranium metal by Levet and Noel identified the difficulty in preparing the compound in a pure form, as it was invariably accompanied by uranium trichloride and uranium dioxide. [137] This suggests that the mechanism in Eq. 4.6 is readily reversible. Indeed, the reverse of mechanism in Eq. 4.6 is thermodynamically favored above 1190°C. [33] Thus, the distillation of salt from the dissolution baskets for the first three runs at 1350°C should have converted any uranium (III) oxychloride to gaseous uranium trichloride, solid uranium dioxide, and uranium metal. In fact, additional analyses of the post-test fuels from the second and third runs were performed for chlorine via ICP-MS using high-purity (i.e., chlorine-free) dissolution acid, which yielded non-detectable concentrations of chlorine-35 (i.e., <400 and <500 ppm, respectively). Based on these

results, there was no appreciable concentration of salt constituents, including uranium (III) oxychloride, in the post-test fuels.

In short, the initial scoping study identified the predominant effect of uranium metal in the fuel matrix on the dissolution of fuel constituents in LiCl-KCl-UCl_3, as well as the blending of uranium isotopes in this system. The electrical contact of uranium metal in the salt system with the BR3 fuels exhibited reduction of higher uranium oxides (i.e., UO_{2+}) to uranium dioxide; however, the extents and rates of BR3 fuel constituent dissolution were substantially lower and slower, respectively, than those exhibited by the degraded EBR-II fuel with a 31% uranium metal fraction in the fuel matrix. Between the two BR3 fuel forms, the voloxidized fuel exhibited substantially higher alkali and alkaline earth dissolution, which could be attributed to breakdown of the UO_2 matrix from voloxidation and possible increased exposure of these fuel constituents to uranium trichloride. Consequently, the subsequent two studies focused on different means to introduce uranium metal to voloxidized BR3 fuel. Because the available voloxidized BR3 fuel had been subjected to different operating temperatures, it was preheated to 1200°C to provide a common form of the fuel feed for the subsequent studies.

4.4.2 Electrolytic Dissolution Study

For the electrolytic dissolution study, depleted uranium metal dendrites were loaded into a permeable stainless-steel basket, as shown in Figure 4.5. The basket was formed from a perforated 19-mm diameter tube wrapped with 325 x 325 stainless-steel mesh and welded to a stainless-steel bottom disc. The upper end of the basket was open for material loading and configured to an extension rod for suspension in the salt pool. A fuel basket assembly was prepared as shown in Figure 4.5. It consisted of three concentric stainless-steel tubes (a

19-mm diameter outer tube, a 13-mm diameter middle tube, and a 6-mm diameter inner tube). The bottom 76 mm of the inner and outer tubes were perforated, wrapped with 325 x 325 stainless-steel wire mesh, and welded to a bottom stainless-steel ring forming an annular basket. The outer tube was open above the perforated region on two sides, creating a 25-mm tall opening for loading fuel particulate into the basket. The bottom 64 mm of the middle tube was perforated and suspended 3 mm above the bottom of the annular basket and concentric to the inner and outer tubes. The middle tube was electrically isolated from the annular basket and fitted with a rotating electrical connector at the top end. The annular basket was electrically isolated from the HFDA. Thus, when loaded with fuel and suspended in the salt pool, the fuel bed was in electrical contact with the middle tube as a working electrode (see Figure 4.1).

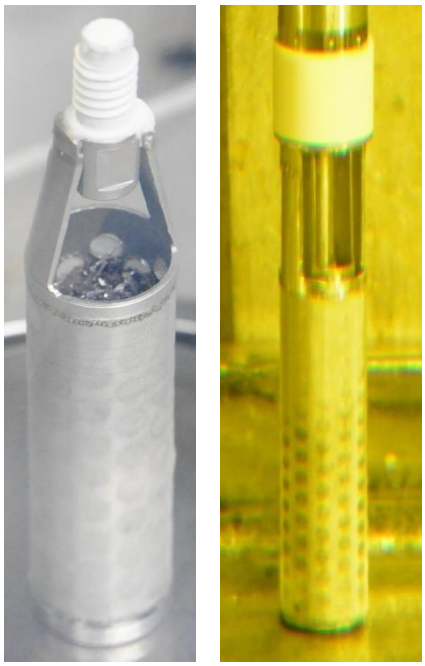

Figure 4.5. Permeable stainless-steel baskets loaded with uranium metal dendrites (left) and preheated BR3 fuel (right).

A molten pool of LiCl-KCl-UCl_3 at 500°C with a uranium mass fraction of 6 wt% was prepared in an alumina crucible inside the HFDA. A new Ag/AgCl reference electrode was suspended in the pool. Cyclic voltammetry was performed on the pretest salt with a 0.8-mm diameter stainless-steel wire suspended in the salt as the working electrode, the uranium metal loaded basket as the counter electrode, and the Ag/AgCl reference electrode. Cyclic voltammetry identified a relative uranium reduction potential of -1.33 V, as shown in Figure 4.6. A pretest salt sample was taken, after which the fuel basket, loaded with preheated and sieved (+325-mesh) BR3 fuel particles, was suspended in the salt pool. The basket soaked for 19 hours (i.e., overnight) under static conditions, after which a salt sample was taken. The open circuit potential of the basket dropped from -0.04 V to -0.4 V during the soak, while that of the uranium metal basket was steady at -1.32 V. The basket was then rotated intermittently for several hours for another overnight period, during which time the open circuit potential of the basket gradually lowered to -0.73 V. A post-basket rotation salt sample was taken, then the basket was electrically connected to the uranium metal basket and rotated intermittently for another overnight period. An initial current spike of 125 milliampere was observed, which quickly subsided to several milliampere. The cross-connection between the two baskets was opened, and a salt sample was taken. Cyclic voltammetry was then performed on the fuel basket. Figure 4.6 shows cyclic voltammograms of a stainless-steel wire and fuel basket in the salt pool.

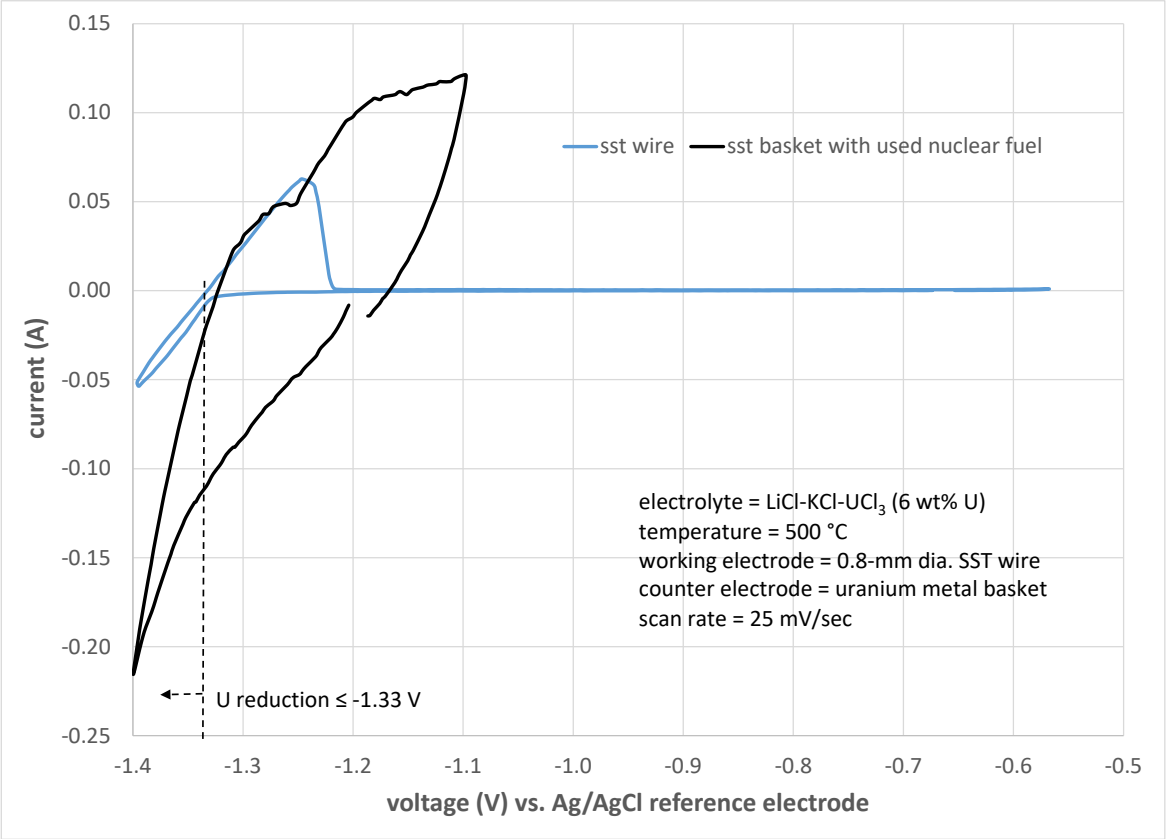

Figure 4.6. Cyclic voltammograms of stainless-steel wire and oxide fuel basket as working electrodes in LiCl-KCl-UCl_3 at 500°C.

A series of alternating uranium electrotransports from the uranium metal basket to the fuel basket (cathodic dissolution) and back (anodic stripping) was then performed at (1) 500°C, (2) 650°C, and (3) 650°C with a 19 wt% uranium fraction in the salt phase. The first cathodic dissolution involved electrotransporting an equivalent charge (~7 ampere hours) to convert the assumed U_3O_8 fuel loading to UO_2 and then to UOCl, as in Eq. 4.6. Subsequent anodic stripping and cathodic dissolution operations involved electrotransporting an equivalent charge (~4 ampere hours) to accommodate the reverse and forward direction, respectively, of reaction in Eq. 4.6. The first cathodic dissolution was accompanied by an unanticipated 8-day pause midway through the operation due to facility limitations, during which time additional uranium metal pellets were added to the uranium basket. Cathodic

dissolution currents ranged from 44 – 66 milliampere, while those for anodic stripping ranged from 21 – 195 milliampere. Salt samples were taken after each cathodic dissolution and anodic stripping operation totaling to 11 samples.

The post-test fuel basket was truncated and subjected to 1100°C with reduced pressure below 100 mTorr in a distillation apparatus to distill away salt from the fuel and basket. The fuel was separated from the basket and random grab samples were taken for analysis. Table 4.6 shows salt sample analysis results for this study, and Table 4.7 shows the pretest and post-test fuel sample results, along with extents of dissolution from the weighted average fuel sample results. For brevity, the salt and fuel sample analysis results were similarly grouped into alkali, alkaline earth, lanthanide, and transuranium, as in the previous study, with the exception that alkaline earths in this study were comprised of Ba-136/137/138 and Sr-86/88.

Table 4.6. Consolidated results of salt sample analyses for run 2.1.

Sample		**Alkali (ppm)**	**Alkaline earth (ppm)**	**Lanth-anide (ppm)**	**Trans-uranium (ppm)**	**U (ppm)**	***U-235 (%)***
hour	**description**						
0	Pre-test	8.93	9.58	37.5	43.7	64500	*0.333*
19	Static soak	54.4	64.9	100	94.5	63600	*0.349*
41	Basket rotation	58.8	66.3	104	81.2	64300	*0.359*
64	Cross-connect	59.5	75.0	119	90.3	59300	*0.422*
330	Cathodic-mid	55.0	73.1	148	101	62800	*0.394*
378	Cathodic-final	56.6	69.6	134	98.7	61900	*0.375*
402	Anodic stripping	59.1	67.0	148	101	62400	*0.373*
497	Cathodic dissol.	59.0	63.6	207	124	61300	*0.445*
568	Anodic stripping	57.5	73.0	202	139	64000	*0.580*
666	Cathodic dissol.	45.9	71.7	211	117	200000	*0.416*
717	Anodic stripping	45.0	72.0	192	119	201000	*0.435*

Table 4.7. Consolidated results of fuel sample analyses for run 2.1.

ppm	**Pre-test**		**Post-test**		**Extent of Dissolution (%)**
	Sample A	**Sample B**	**Sample A**	**Sample B**	
Alkali	1251	1169	4.77	4.36	99.6
Alkaline earth	1960	1972	347	340	82.6
Lanthanide	7860	7880	2718	2623	66.2
Transuranium	5150	5200	1960	1920	62.6
Uranium	791000	778000	804000	791000	n/a
U-235 (iso%)	*5.17*	*5.18*	*3.20*	*3.24*	*n/a*

The extents of oxide fuel constituent dissolution in the subject salt system from this study trended with the Gibbs free energies of reaction for the listed mechanisms, as shown in Table 4.2. Specifically, the more thermodynamically favored reaction of monovalent oxides with uranium trichloride exhibited the highest extent of dissolution followed by those of the divalent and trivalent oxides.

The results of the salt sample analyses elucidated the effectiveness of the various parameter adjustments in this study. Figure 4.7 shows a time plot of fuel constituent mass (as opposed to concentration to accommodate the mass addition of salt in the transition to a 19 wt% uranium fraction) by functional group. This plot identifies how the alkali metal constituents dissolved almost entirely into the salt pool by the first salt sample after 19 hours of oxide fuel basket soaking under static conditions. Following electrical cross-connection of the oxide fuel basket with the uranium metal basket, the alkaline earth constituents reached a

plateau by the 64-hour salt sample; however, the alkaline earth inventory did exhibit a slight increase after raising the uranium concentration in the salt to 19 wt%. Only small fractions of the lanthanide and transuranium constituents dissolved into the salt pool after the first three salt samples. However, their inventories increased successively following electrolytic dissolution operations at (1) 500°C and 6 wt% uranium concentration in the salt phase, (2) a temperature increase to 650°C, and (3) a salt phase uranium concentration increase to 19 wt%.

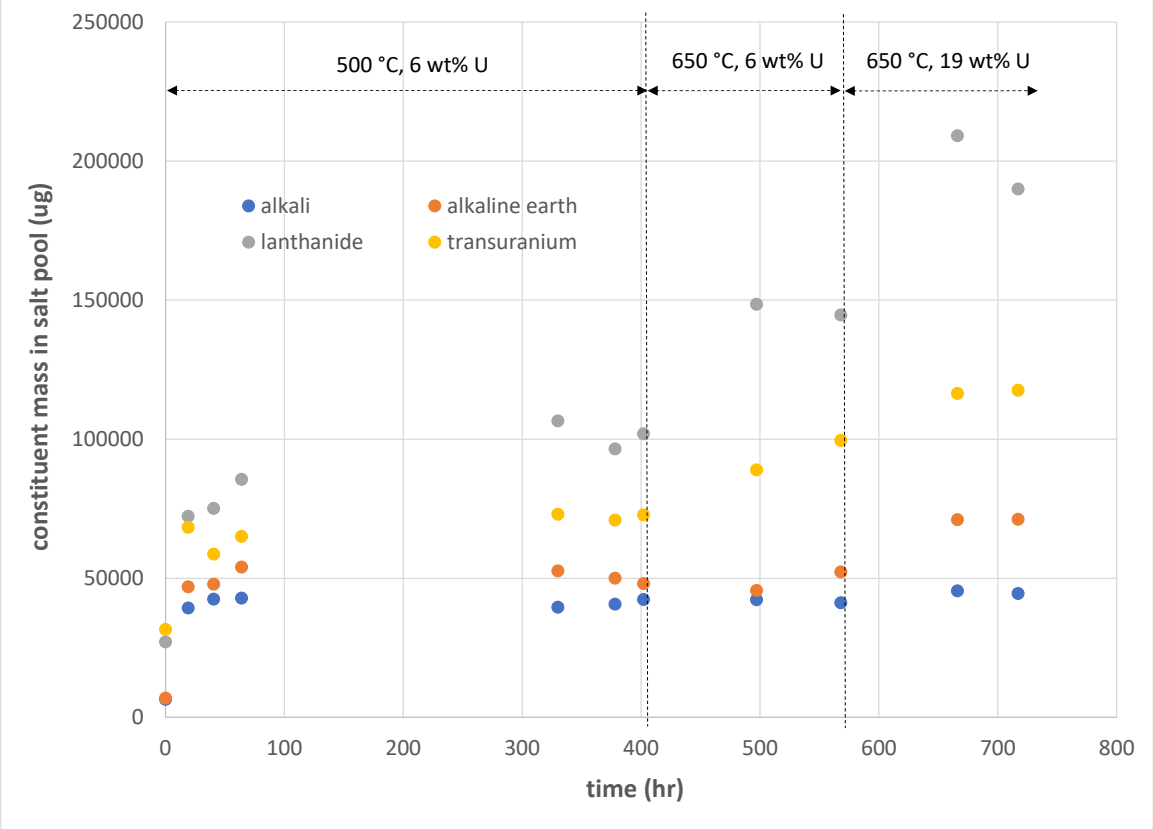

Figure 4.7. Time plot of fuel constituent mass in salt pool for run 2.1.

For this study, the run time was 717 hours, substantially longer than in the scoping study. This was due in part to an unanticipated 8-day pause in operations, as well as low imposed currents during electrolytic dissolution operations to avoid bulk deposition of

uranium metal on the oxide fuel basket. Nevertheless, the extents of oxide fuel constituent dissolution in this study (run 2.1) were substantially higher than those in the previous study with voloxidized BR3 fuel (run 1.3). This indicated the promoting effects of uranium metal transport to and from the oxide fuel basket, along with successive increases in temperature from 500 to 650°C and uranium concentration in the salt from 6 to 19 wt%. However, the extents of dissolution in this study were lower than those observed in degraded EBR-II fuel from the previous study (run 1.1).

4.4.3 Chemical-Seeded Dissolution Study

For the chemical-seeded dissolution study, three new permeable stainless-steel basket assemblies were prepared. Each assembly consisted of a 19-mm diameter closed-end stainless-steel tube and an accompanying auger, as shown in Figure 4.8. The bottom 76 mm of the tube was sintered stainless-steel with a 0.01-mm nominal porosity. The tube was slotted immediately above the sintered portion to accommodate fuel particulate loading. A 130-mm long auger and accompanying extension rod were positioned concentric to the tube with the auger standing on the bottom of the closed end. The top of the auger extension rod was fitted with an electrical connection to facilitate uranium metal electrotransport while rotating the basket relative to a stationary auger.

A molten pool of LiCl-KCl-UCl_3 at 650°C with a uranium mass fraction of 19 wt% was prepared in a tantalum crucible that was inside of, and electrically isolated from, the HFDA steel crucible. A 6-mm diameter tantalum tipped extension rod (see Figure 4.8) was lowered into the salt pool and stood on the bottom of the tantalum crucible, such that the rod and crucible together functioned as a counter electrode. A pre-test salt sample was taken. As shown in Table 4.1, preheated BR3 fuel and uranium metal particulate were loaded into the

first basket assembly which was then suspended in the salt pool. Another salt sample was taken after rotating and soaking the basket for an overnight period.

Figure 4.8. Tantalum rod (left) and sintered stainless-steel tipped basket assembly (center and right) for oxide fuel loading in chemical-seed dissolution study.

The auger lead was configured as an anode, and the tantalum rod was configured as a cathode to a power supply, then 3.2 ampere hours were applied, sufficient to move an equivalent 9.5 g of uranium metal from the basket to the tantalum rod. Another salt sample was taken, after which the salt temperature was raised to 725°C. After several hours of soaking at 725°C, another salt sample was taken. The salt temperature was then raised to 800°C, and a salt sample was taken after soaking the basket for several hours. The basket was then removed from the HFDA and the salt temperature was lowered to 650°C. The same approach was taken for the second basket.

In the third run, only the BR3 fuel particles were loaded in the basket prior to immersion in the salt pool. Successive salt samples were taken after soaking the basket at 650, 725, and 800°C. The basket was then removed from the HFDA, and the prescribed amount of uranium metal particulate was added to the oxide fuel particulate in the basket. The basket was re-immersed in the salt pool, and the same procedure was applied as in the first two runs, including a 650°C soak, uranium electrotransport at 650°C, soak at 725°C, and soak at 800°C, followed by basket removal.

The fuel baskets were truncated from their assemblies and collectively subjected to 1100°C and a reduced pressure below 100 mTorr in a distillation apparatus to distill away salt from the fuel and baskets. Each batch of fuel was separated from its respective basket and auger, and a random grab sample was taken for analysis. Table 4.8 shows the salt sample analysis results for this study, and Table 4.9 shows the pre- and post-test fuel sample analysis results. For brevity, the salt and fuel sample analysis results were similarly grouped into alkali, alkaline earth, lanthanide, and transuranium, as in the previous study.

Table 4.8. Consolidated results of salt sample analyses for runs 3.1, 3.2, and 3.3.

Sample		Alkali (ppm)	Alkaline earth (ppm)	Lanth-anide (ppm)	Trans-uranium (ppm)	U (ppm)	*U-235 (%)*
hour	**description**						
Run 3.1							
0	Pre-test	1.7	23.1	52.4	14.9	198000	*0.336*
18	650°C soak	9.76	83.7	145	69.5	199000	*0.365*
161	Electrotransport	9.34	89.4	253	133	193000	*0.441*
168	725°C soak	11.1	112	293	159	196000	*0.475*
192	800°C soak	10.3	102	367	202	197000	*0.543*
Run 3.2							
21	650°C soak	8.98	174	427	277	197000	*0.608*
120	Electrotransport	9.54	155	583	328	197000	*0.672*
125	725°C soak	10.3	164	619	350	197000	*0.702*
148	800°C soak	11.6	178	666	374	198000	*0.723*
Run 3.3							
113	650°C soak	11.5	216	732	414	195000	*0.750*
120	725°C soak	13.2	232	758	409	194000	*0.754*
143	800°C soak	13.4	232	757	426	195000	*0.938*
167	650°C DU soak	12.1	235	771	431	196000	*0.766*
288	Electrotransport	12.0	223	781	438	198000	*0.748*
295	725°C soak	13.2	236	799	446	195000	*0.740*
319	800°C soak	12.2	228	792	448	195000	*0.760*

Table 4.9. Consolidated results of fuel sample analyses for runs 3.1, 3.2, and 3.3.

ppm	**Pre-test**		**Post-test**		
	Sample A	**Sample B**	**Run 3.1**	**Run 3.2**	**Run 3.3**
Alkali	100	114	0.23	0.17	<6
Alkaline earth	4810	5060	86.9	92.3	88.6
Lanthanide	11700	11600	928	645	637
Transuranium	6760	6690	723	503	504
Uranium	793000	787000	879000	880000	867000
U-235 (iso%)	*3.54%*	*3.56%*	*1.11%*	*1.09%*	*1.26%*

Sufficient uranium metal particulate was added to each basket to convert U_3O_8 to UO_2, as shown in the following reaction mechanism, with sufficient excess uranium to facilitate the reaction in Eq. 4.6. [33]

$$U_3O_8 + U \rightarrow 4\ UO_2 \qquad \Delta G_{Rx,650C} = -742\ kJ \qquad (4.7)$$

The available uranium metal was then electrotransported away from the basket, leaving UO_2 behind. Specifically, 16.5 g of uranium metal particulate was blended with 24.4 g of U_3O_8 in run 3.1, after which an equivalent 9.5 g of uranium metal was electrotransported from the basket to the tantalum rod. Of the remaining 7.0 g of uranium metal in the basket, 6.9 g were consumed in the conversion of U_3O_8 to UO_2, per Eq. 4.7. The fuel sample analyses revealed a uranium concentration in the post-test fuel (see Table 4.9) consistent with UO_2. Similarly, runs 3.2 and 3.3 yielded uranium concentrations in the post-test fuel samples consistent with UO_2. Accounting for the uranium mass addition to the fuel

samples to convert U_3O_8 to UO_2, the extents of fuel constituent dilutions for this study are shown in Table 4.10.

Table 4.10. Extents of alkali, alkaline earth, lanthanide, and transuranium constituent dissolution in molten salt from runs 3.1, 3.2, and 3.3.

	Run 3.1	**Run 3.2**	**Run 3.3**
Alkali	99+%	99+%	>92%
Alkaline earth	97.7%	97.6%	97.7%
Lanthanide	89.8%	92.9%	93.0%
Transuranium	86.2%	90.4%	90.4%

The fuel sample analysis results for this study are consistent with those from run 1.1, underscoring the capacity of uranium metal in the oxide fuel matrix to promote the dissolution of the subject fuel constituents. As in the previous two studies, the more thermodynamically favored reaction of monovalent oxides with uranium trichloride exhibited the highest extent of dissolution followed by those of the divalent and trivalent oxides. Also in this study, uranium isotope blending was observed, as the U-235 fraction in the BR3 fuel dropped from 3.5% to 1.1 – 1.3%. Accordingly, the U-235 fraction in the salt samples exhibited an increase.

The salt sample analyses identified the effects of parameter adjustments. Figure 4.9 shows a plot of grouped fuel constituent concentrations as a function of accumulated run time for the series of three dissolutions. Generally, the alkali and alkaline earth constituents dissolved almost entirely into the salt pool after the first salt sample was taken following the initial basket soak in each run. The lanthanide and transuranium constituent concentrations typically exhibited increases following uranium electrotransport, while temperature increases

tended to accelerate the dissolution rates. Although, the concentration increases were less pronounced in the third run, owing to the smaller fuel loading and a longer initial soak time. (Note: The temperature settings of 650, 725, and 800°C were selected to coincide with alpha, beta, and gamma phases of uranium metal.) The dissolution times in this study (148 – 319 hours) were longer than those in the scooping study (33 – 120 hours), but shorter than the 717 hours in the electrolytic dissolution study. The longer dissolution times in the chemical-seeded study were largely due to the low imposed currents of electrotransporting uranium from the fuel matrix without dissolving the stainless-steel baskets.

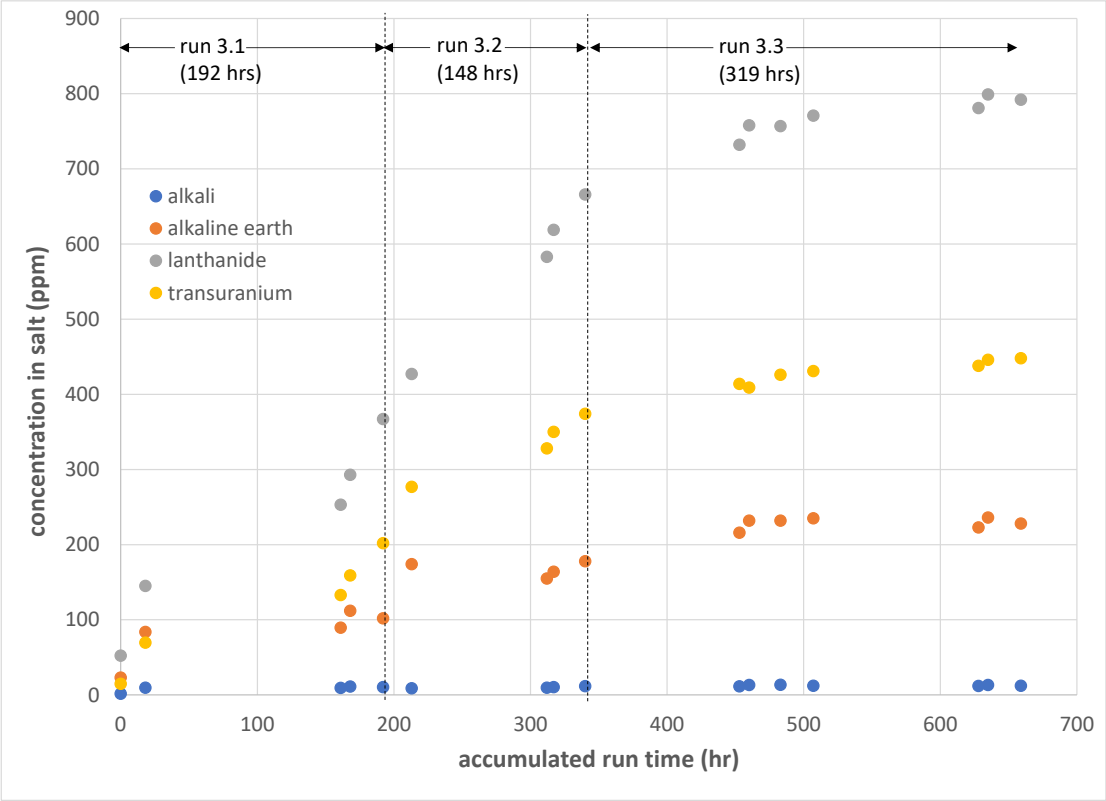

Figure 4.9. Plot of fuel constituent concentration in salt phase versus accumulated time for runs 3.1, 3.2, and 3.3.

4.5 Summary and Conclusions

Previous cited work identified extents of lanthanide and transuranium constituent dissolution greater than 90% from used fast reactor MOX fuel (containing a 29 wt% uranium metal fraction) in LiCl-KCl-UCl_3 at 500°C with a 9 wt% uranium fraction in the salt phase. The previous work prompted a series of three progressive studies (including an initial scoping study, an electrolytic dissolution study, and a chemical-seeded dissolution study) to further investigate parameters and possible reaction mechanisms pertaining to the dissolution of used nuclear oxide fuel constituents in molten LiCl-KCl-UCl_3.

An initial scoping study was performed by contacting oxidized fast reactor metal alloy fuel from EBR-II and forms (crushed and voloxidized) of pressurized water reactor fuel from BR3 successively in LiCl-KCl-UCl_3 at 500°C with a 9 wt% uranium fraction in the salt phase followed by salt removal from the oxide fuels via distillation. Based on pretest and post-test fuel compositions, the scoping study identified stark contrasts in the extents of alkali, alkaline earth, lanthanide, and transuranium constituent dissolution. Specifically, 91.5 – 99.5% of the subject constituents dissolved away from the EBR-II fuel in a 33-hour period, compared to 14.0 – 24.0% from the crushed BR3 fuel in 120 hours and 12.4 – 93.7% from the voloxidized BR3 fuel in 50 hours. The scoping study also identified significant uranium isotope blending, as the U-235 fraction in the EBR-II fuel dropped from 57.4% to 30.2%, while the same in the salt phase rose from 0.356% to 7.42%. The stark contrast in extents of constituent dissolution and uranium isotope blending over the given time periods were attributed to a 31% uranium metal fraction that was subsequently identified in the pre-test EBR-II fuel. The metal fraction in the fuel matrix likely facilitated thermodynamically favored reaction mechanisms that involved a solid uranium (III) oxychloride intermediate

with the same uranium valency as the uranium trichloride in the salt phase. This could have contributed to penetration of the fuel matrix for constituent dissolution and uranium isotope blending. The scoping study also identified a stark contrast in extents of alkali and alkaline earth constituent dissolution between the crushed and voloxidized BR3 fuel, suggesting that conversion of the UO_2 fuel to U_3O_8 disrupted the fuel matrix sufficiently to facilitate dissolution of these monovalent and divalent oxide groups. Despite a suspended source of uranium metal in the salt pool that was also in electrical contact with the fuel forms, the extents of lanthanide and transuranium constituent dissolution in the BR3 fuel forms were both lacking.

Building upon observations from the scoping study, an electrolytic dissolution study was performed which attempted to provide a uranium metal presence in a voloxidized BR3 fuel via electrotransport from a suspended uranium metal source in a molten pool of LiCl-KCl-UCl_3. Electrotransport of uranium metal to and from a BR3 fuel basket was performed successively at (1) 500°C and a 6 wt% uranium fraction in the salt, (2) 650°C and a 6 wt% uranium fraction, and (3) 650°C and a 19 wt% uranium fraction to investigate the impacts of temperature and uranium concentration in the salt phase on constituent dissolution. The extents of alkali (99.6%), alkaline earth (82.6%), lanthanide (66.2%), and transuranium (62.6%) constituent dissolutions were all higher in the electrolytic dissolution run compared to those with voloxidized BR3 fuel in the scoping study. The electrolytic dissolution study also identified accelerated dissolutions of lanthanide and transuranium constituents upon temperature increases from 500 to 650°C and uranium fractions in the salt phase from 6 to 19 wt%. However, the 717-hour period for the electrolytic dissolution study was excessive, which was due in part to low imposed currents on the fuel and uranium baskets to avoid bulk

uranium deposition on the fuel basket and to preclude dissolution of the stainless-steel fuel basket upon subsequent removal of uranium from the basket. The modest improvements in extents of fuel constituent dissolution over a substantially longer period led our team to question the validity of the electrolytic dissolution approach and whether uranium metal was forming within the fuel matrix or elsewhere on the fuel basket.

The chemical-seeded study built upon both the scoping and electrolytic dissolution studies by blending sufficient uranium metal particulate directly with voloxidized BR3 fuel to facilitate conversion of the U_3O_8 fuel form to UO_2 and promote uranium (III) oxychloride formation. Subsequent electrotransport removed remaining uranium metal from the fuel matrix. A series of three successive uranium-seeded fuel runs in a molten pool of LiCl-KCl-UCl_3 with 19 wt% uranium in the salt phase were performed at 650, 725, and 800°C. Extents of alkali (99+%), alkaline earth (97.6 – 97.7%), lanthanide (89.8 – 93.0%), and transuranium (86.2 – 90.4%) dissolutions were observed over periods ranging from 148 – 319 hours. These extents of dissolution were comparable to those of degraded EBR-II fuel in the scoping study, albeit over longer periods of time due to low imposed currents for uranium electrotransport out of the fuel baskets. This final study also identified accelerated rates of lanthanide and transuranium constituent dissolution upon temperature increases from 650 to 725°C and again from 725 to 800°C.

Collectively, the series of progressive studies identified increased rates and extents of used oxide fuel constituent dissolution in LiCl-KCl-UCl_3 by (1) imposing a uranium metal fraction of at least 25 wt% in an oxide fuel matrix, (2) preconditioning an oxide fuel via voloxidation and pre-heating to 1200°C, (3) increasing system temperature from 500 to 800°C, and (4) increasing the uranium fraction in the salt phase from 6 to 19 wt%.

Application of preferred parameters yielded extents of alkali, alkaline earth, lanthanide, and transuranium constituent dissolution above 90%.

This page intentionally left blank

5. Dissolution of Surrogate Advanced Test Reactor Fuel

Forthcoming in *Journal of Nuclear Science and Technology*, "Halogenation of Used Aluminum Matrix Test Reactor Fuel – A Bench-Scale Demonstration with Surrogate Materials"

5.1 Objectives

The objective of this study was to demonstrate a halogenation technique that could be applied to separate aluminum from the used aluminum matrix ATR fuel in molten-halide salt systems, as a head-end step to subsequent treatment and disposition of the fuel's uranium and fission products. To simplify the demonstration, neodymium metal was used as a non-radiological surrogate for uranium metal, and ammonium halides were used as the halogenating agents. Thus, forms of aluminum and neodymium metal were blended at bench scale with either ammonium chloride or bromide and lithium chloride or bromide, respectively, and heated. Under these conditions, ammonium chloride and bromide sublime at 338 and 396°C, respectively, decomposing into ammonia and hydrogen chloride and hydrogen bromide gases, respectively. The hydrogen halide gases react with aluminum and neodymium metal to form their respective halides. The overall generalized reaction mechanism is as follows.

$$M + 3\ NH_4X \rightarrow MX_3 + 3\ NH_3(g) + 3/2\ H_2(g) \qquad (5.1)$$

where M is aluminum or neodymium metal, and X is chlorine or bromine. As the aluminum halides form primarily above their respective sublimation point (180°C for aluminum chloride) and normal boiling point (255°C for aluminum bromide), they gasify and separate from the respective neodymium halides, which then fuse with their respective lithium halides. To determine the effectiveness of this halogenation technique, researchers analyzed the fused salt and distillate product samples, identifying the extents of aluminum

and neodymium separation. As the generated aluminum halide would require a separate disposal pathway, the aluminum chloride distillate from one of the runs in this demonstration was treated to form a more durable, less soluble product by reacting it with magnesium oxide to convert the aluminum chloride to an insoluble aluminum oxide. The treated aluminum chloride distillate is referred to here as a waste form.

5.2 Experimental Aspects

5.2.1 Approach

As aluminum matrix ATR fuel is formed from metal powders that are hot rolled with aluminum cladding, this demonstration used neodymium and aluminum metal powders as surrogate forms of feed materials in a series of halogenation experiments. Aluminum foil was also added to some of the runs, representing the form of cladding in used ATR fuel. Lithium chloride and bromide were used as the primary diluents in the salt phases of this demonstration. The experiments involved blending ten parts by mass of the select lithium halide to one part neodymium metal powder and one part aluminum metal powder and, for a subsequent run, one part aluminum metal foil at a scale of 50 g of lithium halide. Sufficient ammonium halide was added to each blend to accommodate a 10% excess stoichiometric amount of halogen for the given masses of neodymium and aluminum metals in a run. Accordingly, a nominal 50 g of lithium chloride was blended in a glass jar with 5 g of neodymium powder, 5 g of aluminum powder, and 39 g of ammonium chloride for the first run. The blend was then transferred into a glassy carbon crucible, which was covered with an off-gas trap and heated in a furnace to approximately 500°C at 10°C/hr to sublimate the ammonium chloride and thereby chlorinate the neodymium and aluminum metals per Eq. 5.1. The volatile aluminum chloride product was drawn into an off-gas trap, where it

condensed and was collected. The salt blend in the glassy carbon crucible was then heated to 700°C at 5°C/min, the cover was removed, and the salt was stirred momentarily with a glassy carbon rod to assure homogeneity. The furnace was de-energized, and the crucible was allowed to cool to ambient temperature. The salt ingot was removed from the glassy carbon crucible and crushed, from which random grab samples (referred to as bottoms) were taken for analysis. The off-gas trap was opened, and random grab samples (referred to as distillates) were taken for analysis.

The second run was a repeat of the first run, with the exception that a nominal 5 g of aluminum foil in 1 cm × 1 cm pieces was added to the blend along with an additional 33 g of ammonium chloride. The third and fourth runs mirrored the first two runs, with the exception that the chloride feed materials were exchanged for bromide feed materials and heating was limited to 650°C.

The crushed bottoms product from the first run was re-blended with additional ammonium chloride particulate and subjected to the same heating and sampling operations as the previous runs to assess the impact of additional excess ammonium chloride on the process. The same approach was applied to crushed bottoms product from the third run with additional excess ammonium bromide. Samples from each of these two repeat runs were subjected to the same analyses as the previous four runs.

A portion of the distillate product from run 2 was blended with magnesia powder and sodium chloride particulate and heated to 800°C to investigate a technique to process an aluminum chloride distillation product into a waste form as part of this series of experiments. A 10% stoichiometric excess of magnesia powder was added to react with the run 2 distillate

product, which was assumed to be pure aluminum chloride, per the reaction mechanism below. [33]

$$3\ MgO + 2\ AlCl_3 \rightarrow Al_2O_3 + 3\ MgCl_2 \quad \Delta G_{f,800C} = -311.976\ kJ/mol \qquad (5.2)$$

Sufficient sodium chloride was preloaded in the blend to form a eutectic mixture of sodium chloride with the produced magnesium chloride (i.e., NaCl – 41.5 mol% $MgCl_2$ with a binary eutectic melting point of 445°C). [138] After cooling to an ambient temperature, the consolidated product was crushed, and a random sample was taken for analysis. A summary of conditions for the series of experiments is shown in Table 5.1.

Table 5.1. Conditions for series of halogenation and waste form runs.

Run	Mixture Components	Heating Cycle	Samples
1	LiCl particulate, Nd metal powder, Al metal powder, NH_4Cl particulate	Ambient → 500°C at 10°C/hr 500°C → 700°C at 5°C/min	Crushed bottoms, distillate product
1.1	Crushed run 1 bottoms, additional NH_4Cl particulate		Crushed bottoms, distillate product
2	LiCl particulate, Nd metal powder, Al metal powder, Al foil, NH_4Cl particulate		Crushed bottoms, distillate product
3	LiBr particulate, Nd metal powder, Al metal powder, NH_4Br particulate	Ambient → 500°C at 10°C/hr 500°C → 650°C at 5°C/min	Crushed bottoms, distillate product
3.1	Crushed run 3 bottoms, additional NH_4Br particulate		Crushed bottoms, distillate product
4	LiBr particulate, Nd metal powder, Al metal powder, Al foil, NH_4Br particulate		Crushed bottoms, distillate product
5	Run 2 distillate, MgO powder, NaCl particulate	Ambient → 500°C at 10°C/hr 500°C → 800°C at 5°C/min	Crushed consolidated product

5.2.2 Test Specific Equipment

The primary pieces of equipment for the series of halogenation and waste form runs included a furnace and an off-gas trap assembly. A bench-top jeweler furnace (Kerr, Auto Electro-Melt Furnace, Maxi 3kg) was used to heat the mixtures of salts and metals. The furnace instrumentation was modified to facilitate ramp rate and cut-out temperature controls. The vendor-provided graphite crucible within the furnace was machined to accommodate a tapered glassy carbon crucible (SIGRADUR, GAT 32, 320 ml). The glassy carbon crucible was covered with an off-gas trap assembly that stood adjacent to the furnace. The off-gas trap assembly consisted of a 160-mm diameter by 220-mm tall stainless-steel can with a sealed removable upper flanged lid that was fitted with a 50-mm diameter inlet line and a 6-mm diameter outlet line. The can was configured with a set of stainless-steel heat shields that stood 50 mm off the bottom and 50 mm below the top of the can. The heat shields had a 55-mm diameter open center to accommodate a 50-mm diameter downcomer inlet tube that was fixed to the lid. The annulus between the heat shield and the downcomer tube as well as the annulus between the heat shields and the can were packed with steel wool to trap distillate product in the bottom of the can. The inlet line was fitted with two 90-degree elbow joints, the outer of which was fitted with a bell cap that flared to a 75-mm diameter scalloped open end, covering the top open end of the glassy carbon crucible in the furnace. The furnace and off-gas trap assembly were configured on a bench-top inside an argon atmosphere glovebox (MBRAUN LABmaster dp). The trap outlet was fitted with a flexible gas line that passed through a filter (MotorGuard, 0.01-micron filter element) and rotameter (Brooks Instrument) inside the glovebox, through the glovebox wall, and to a vacuum pump (Gast Manufacturing, model DOA-P704-AA) outside the glovebox. The off-

gas system facilitated a sweep gas across the open glassy carbon crucible to quench and direct volatile species into the off-gas trap. Pictures of the furnace and off-gas trap assembly are shown in Figure 5.1. A simplified sectional view of the furnace and off-gas trap assembly is illustrated in Figure 5.2.

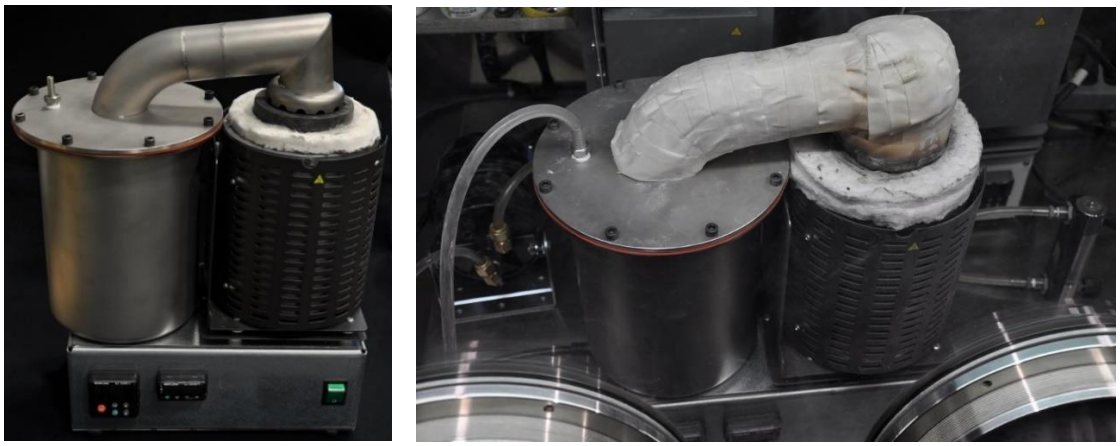

Figure 5.1. Furnace and off-gas trap assembly before (left) and after (right) installation in glovebox.

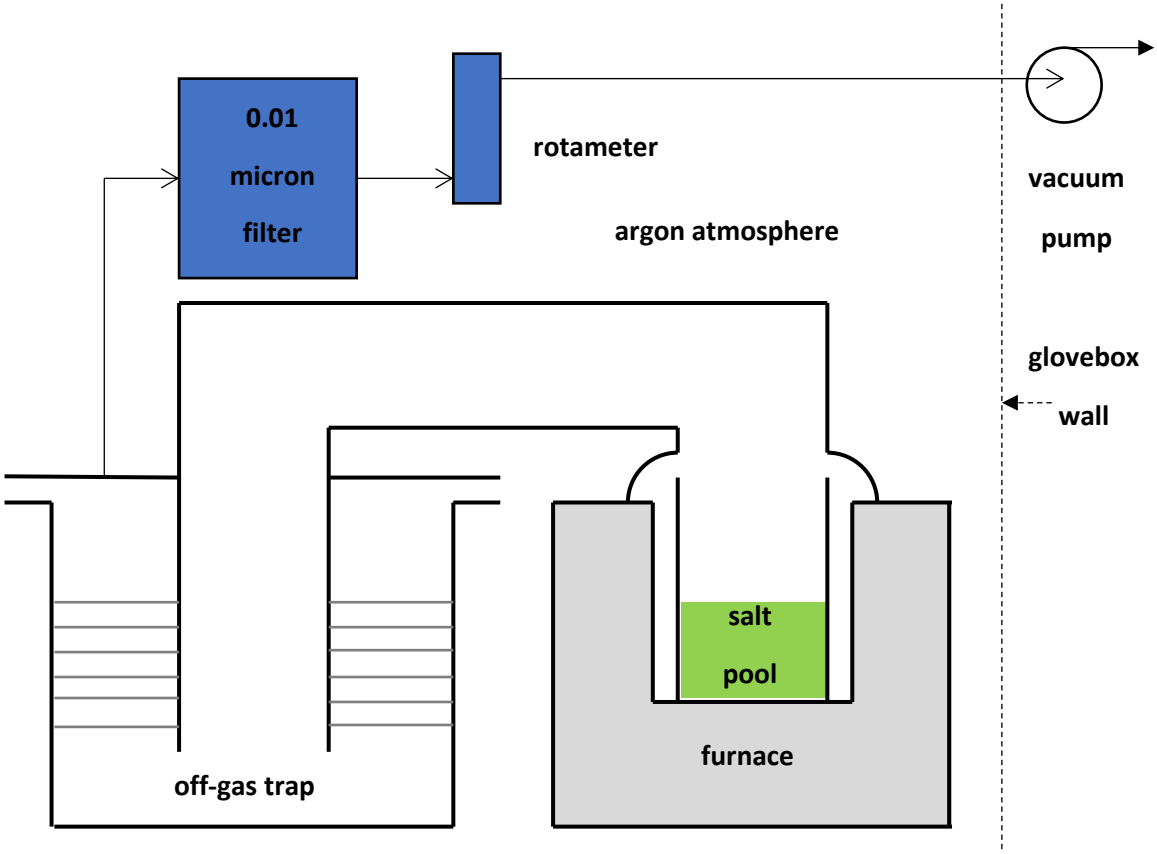

Figure 5.2. Simplified sectional view of furnace and off-gas trap assembly for series of halogenation and waste form runs.

5.2.3 Test Specific Materials

The primary materials for the series of halogenation and waste form runs consisted of reactive ammonium salts, reactive metals, diluent salts, and a neutralizing oxide. Ammonium chloride and ammonium bromide are hygroscopic materials and were not available in a high-purity anhydrous form from suppliers. Consequently, the ammonium chloride (Alfa Aesar, 99.999%, Puratronic) and ammonium bromide (Alfa Aesar, 99.999%, Puratronic) used in this study were dried, crushed, and sieved to the desired particle size using a bench-top box furnace in an argon atmosphere glovebox. Specifically, the procured granular ammonium salts were loaded into trays and heated to 120°C for at least 20 hours,

followed by heating at 140°C for at least four hours. The dried material was crushed and sieved to particle sizes below 30-mesh.

The reactive metals included neodymium metal powder (Alfa Aesar, 99.9%), aluminum metal powder (Alfa Aesar, 99.97%), and aluminum foil (Alfa Aesar, 99.99%, 0.25 mm thick). The metal powders are pyrophoric materials and were handled under an argon atmosphere. The neodymium metal powder was procured in nominal 5 g packages, each of which was used in its entirety in a halogenation run. The thickness of the aluminum foil added to the mixtures of runs 2 and 4 approximated that of used ATR cladding.

Diluent salts included lithium chloride (Alfa Aesar, 99.9%, ultra-dry), lithium bromide (Alfa Aesar, 99.97%, ultra-dry), and sodium chloride (Sigma Aldrich, 99.999%), each of which was procured as anhydrous -10 mesh beads packaged under argon. Each of these alkali-metal chlorides was crushed and sieved to particle sizes below 30-mesh. Magnesium oxide (J. T. Baker, powder) was used as a neutralizing oxide for the aluminum chloride distillate product from run 5 to form, along with sodium chloride, a consolidated waste form.

5.2.4 Sample Characterization

Product samples from the series of halogenation and waste form runs were halved, forming two sample sets for chemical and diffraction analyses. One set of product samples was characterized for elemental composition via ICP-OES. The other set of samples were ground into fine powders and characterized using XRD (Rigaku SmartLab, Cu Kα, 40 kV and 44 mA). The XRD data were collected between 10 – 80° with a step of 0.04° at 4° per min.

5.3 Calculations

The high surface area of neodymium and aluminum metal powder feed materials along with the multiple constituent phases that were expected in this series of runs created a complex set of conditions that warranted calculations prior to proceeding with the experiments. Specifically, a model was created to assess possible chemical equilibrium conditions and related reaction mechanisms to ensure that intended products under the design operating conditions would likely be formed. Chemical equilibrium calculations provide a straightforward means of assessing product compositions as a function of temperature for a given quantity of raw materials. Commercially available software [33] was used to perform such calculations with a Gibbs energy minimization model, which is based on prior work by others. [136] After inputting the defined feed materials for run 1 and assuming unit activities and ideal mixing, the model produced a plot of possible constituent equilibrium inventories as a function of temperature, as shown in Figure 5.3. Only the predominant compounds of 47 selected possible compounds are shown in Figure 5.3. A noteworthy finding from the model for run 1 is the decomposition of ammonia into nitrogen and hydrogen gases from possible intermediate interactions with neodymium and aluminum. Indeed, the model identifies the formation and enduring presence of aluminum nitride, which would preclude its separation from neodymium. Another finding from the model is the intermediate formation of lithium-aluminum chloride, which decomposes into lithium chloride and gaseous aluminum chloride at temperatures above the normal sublimination point (i.e., 180°C) of aluminum chloride.

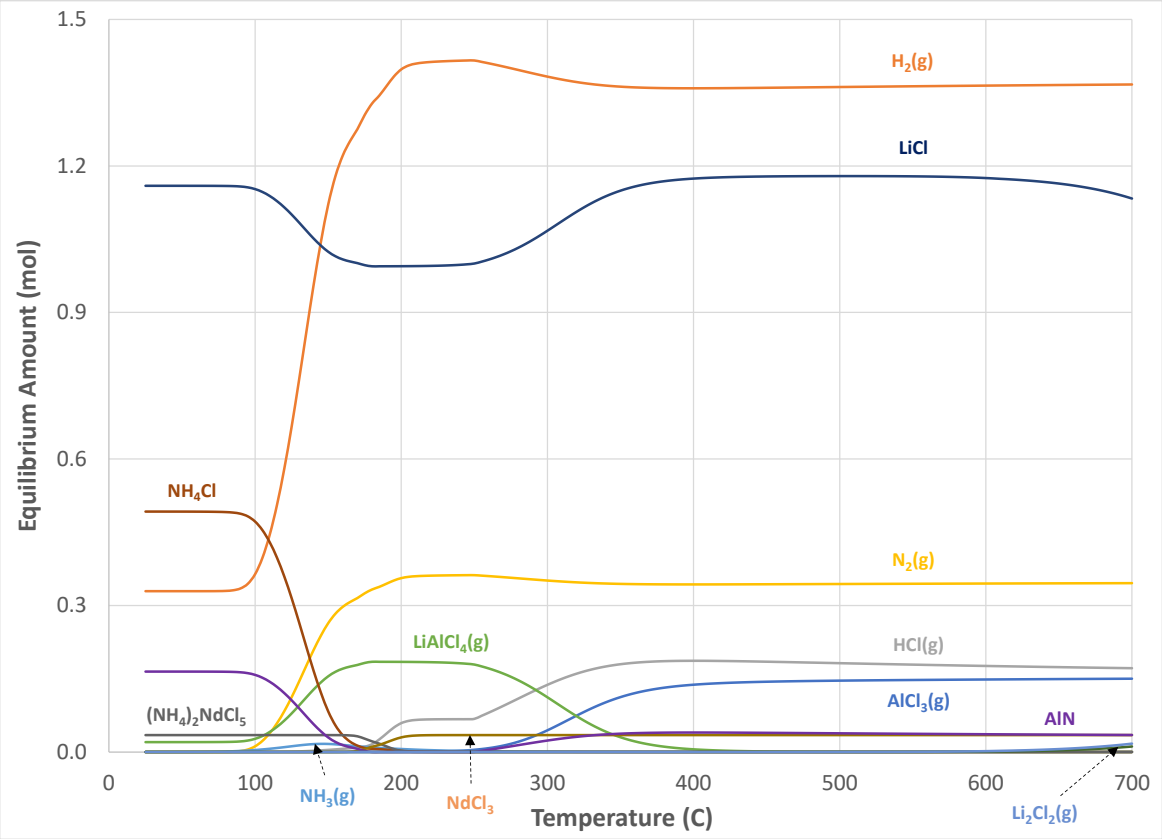

Figure 5.3. Modeled equilibrium molar contents versus temperature for halogenation run 1.

A similar model was created for run 3, which produced a nearly identical outcome except for the presence of bromide compounds in lieu of the companion chloride compounds. Another model was generated for run 5, which produced a plot of possible constituent concentrations as a function of temperature as shown in Figure 5.4. For modeling purposes, it was assumed that the 10% excess ammonium chloride from run 2 resided with the aluminum chloride distillate.

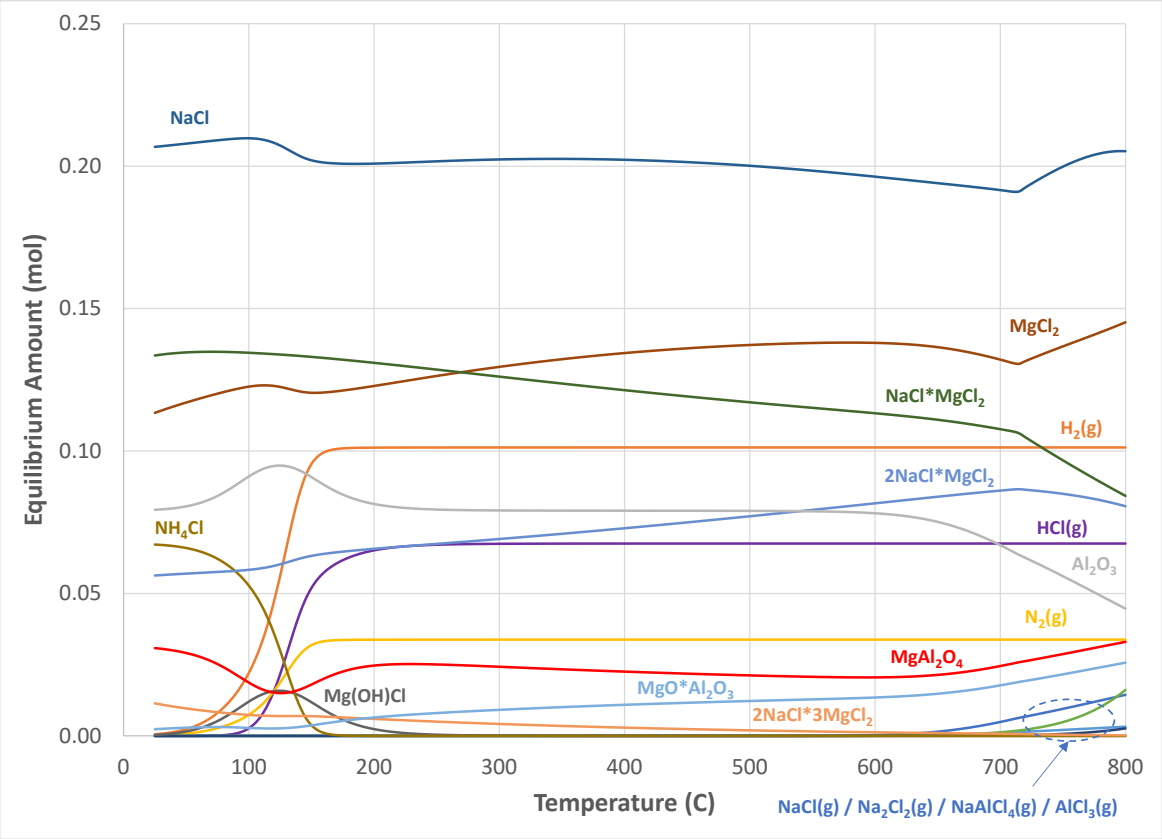

Figure 5.4. Modeled equilibrium molar contents versus temperature for run 5.

The primary finding from the model of run 5 is the conversion of magnesium oxide and aluminum chloride to aluminum oxide and magnesium chloride, the latter of which leads to a variety of mixed chloride compounds with sodium chloride. The model also shows excess magnesium oxide forming mixed magnesium and aluminum oxides. Excess ammonium chloride appears to be inconsequential in this model, as it decomposes into nitrogen, hydrogen, and hydrogen chloride gases.

5.4 Operations and Results

In the first run 5.081 g of neodymium metal powder, 5.023 g of aluminum metal powder, 39.084 g of ammonium chloride particulate, and 50.042 g of lithium chloride particulate were blended in a 250-ml glass jar, as shown in Figure 5.5. The mixture was transferred to a pre-weighed glassy carbon crucible, also shown in Figure 5.5. After heating the mixture to 700°C and removing the off-gas trap from atop the glassy carbon crucible, the molten solution was stirred with a glassy carbon rod and no solid phase was apparent. The furnace was de-energized, and the cooled salt ingot separated readily from the glassy carbon crucible. The ingot was halved, revealing an upper dark layer and lower light layer, as shown in Figure 5.6. The off-gas trap was opened, revealing a loose fine colorless powder, as shown in Figure 5.6.

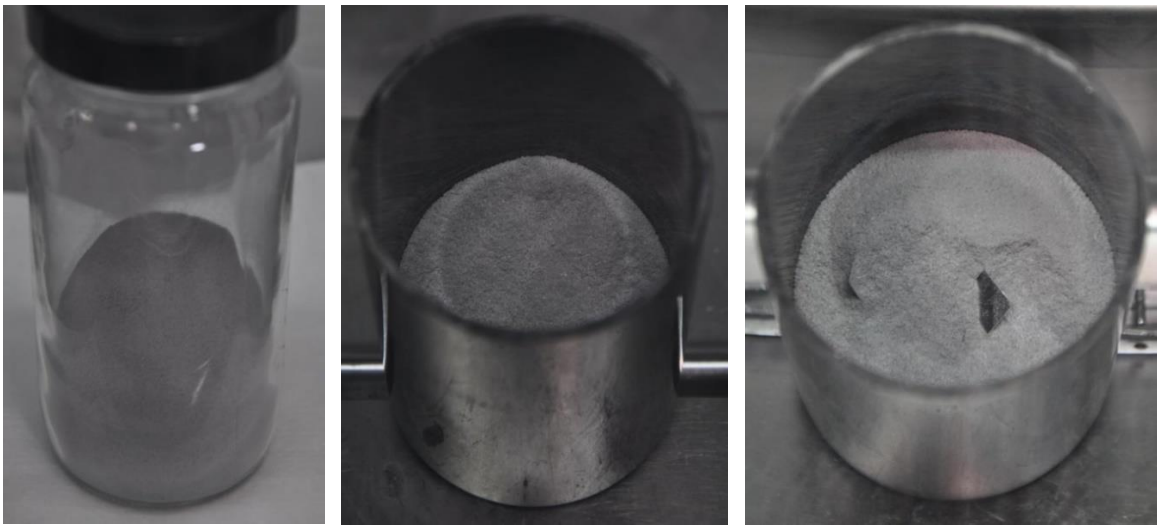

Figure 5.5. Neodymium metal powder, aluminum metal powder, ammonium chloride, and lithium chloride blend before (left) and after loading in glassy carbon crucible for run 1 (center) and the same blend with aluminum foil for run 2 (right).

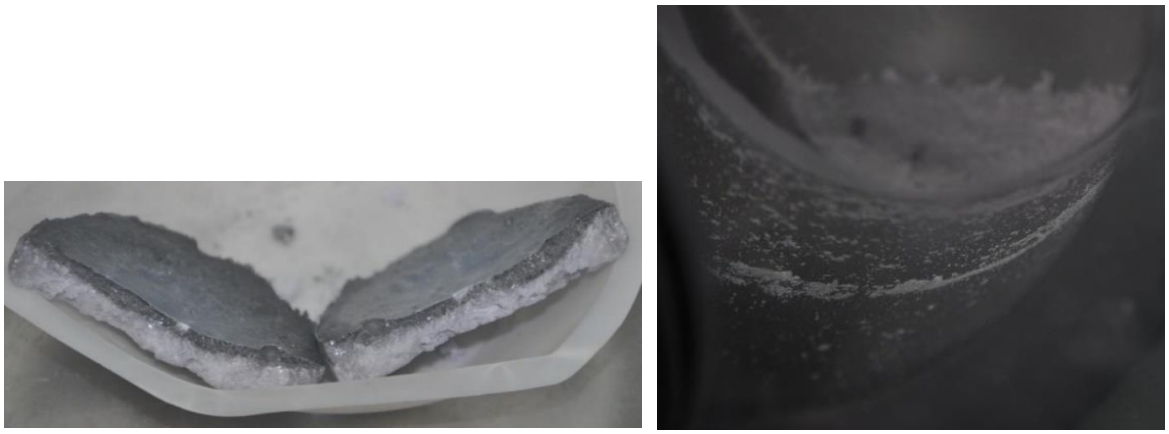

Figure 5.6. Bottoms (left) and distillate (right) products from run 1.

The procedure was repeated for runs 2 – 4, as outlined in Table 5.1. A picture of the loose blend of materials for run 2, including aluminum metal foil pieces, is also shown in Figure 5.5. The bottoms and distillate products for runs 2 – 4 exhibited similar colors and consistencies to those from the first run. No degradation or change in mass was observed in the glassy carbon crucible throughout the series of runs. Notable mass measurements for the halogenation runs are listed in Table 5.2.

Table 5.2. Summary of recorded masses from halogenation Runs 1–4.

Grams \ Run	1	1.1	2	3	3.1	4
Pre-run masses in glass jar						
Nd powder	5.081	—	5.005	5.116	—	5.000
Al powder	5.023	—	5.171	5.086	—	5.144
Al foil	—	—	5.002	—	—	5.086
NH_4Cl	39.084	16.116	72.682	—	—	—
NH_4Br	—	—	—	72.389	15.695	133.749
LiCl	50.042	—	50.012	—	—	—
LiBr	—	—	—	50.202	—	50.314
Crushed bottoms	—	54.593	—	—	59.318	—
Pre-run masses in crucible						
Total loose blend	99.233	70.709	137.894	132.746	74.970	199.300
Post-run product mass in crucible						
Bottoms	58.418	54.526	59.377	63.427	59.069	65.262

In the fifth run 30.000 g of distillate product from run 2 was blended with 14.963 g of magnesium oxide and 27.804 g of sodium chloride in a glass jar, of which 72.728 g was transferred to a glassy carbon crucible and heated as outlined in Table 5.1. At 800°C the off-gas trap was removed, and there was no visible collection of any off-gas particulate. The molten solution was stirred with a glassy carbon rod, exhibiting an off-white opaque slurry

consistency. The furnace was de-energized, and the cooled ingot separated readily from the glassy carbon crucible. The mass of the bottoms product was 62.527 g. The ingot was broken, revealing an off-white consistency throughout, as shown in Figure 5.7 along with the blend before and after consolidation. The bottoms product was crushed, from which a random grab sample was taken for XRD analysis.

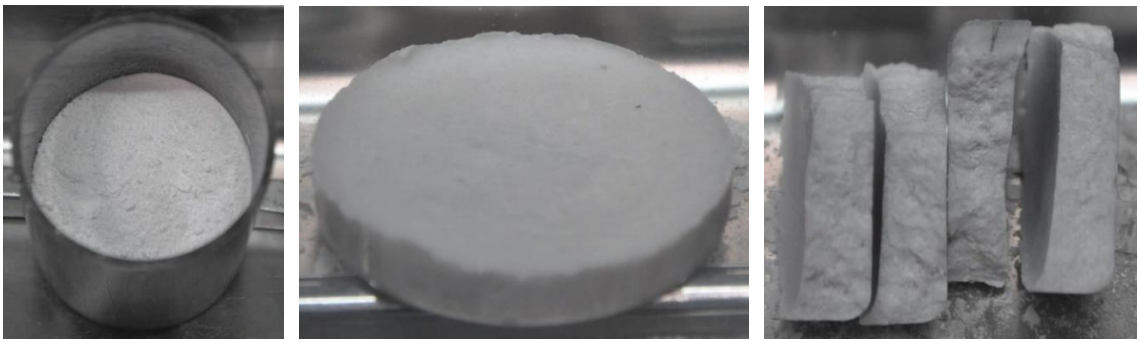

Figure 5.7. Waste-form blend before (left) and after (center) consolidation and breaking (right).

Each of the bottoms and distillate product samples was subjected to elemental analysis for neodymium, aluminum, and lithium via ICP-OES, the results of which with a margin of error of ± 5 – 15% at 2 sigma are shown in Table 5.3.

Table 5.3. Elemental analysis results for bottoms and distillate samples from runs 1 – 4.

ppm \ Run	1	1.1	2	3	3.1	4
Distillate						
Al	124,000	<1,100	125,000	74,400	5,730	61,900
Li	<330	<110	<280	<150	<110	<80
Nd	<5,300	<1800	<4,400	<2,300	<1,800	<1,300
Bottoms						
Al	<1,900	1,470	8,790	<2,500	1,490	12,600
Li	147,000	155,000	137,000	62,600	64,800	63,900
Nd	79,700	82,800	78,200	73,300	69,100	71,400

The bottoms and distillation samples from runs 1 – 5 were ground to a powder, from which XRD sample trays were prepared and analyzed. The XRD patterns for the samples of chloride bottoms products (runs 1, 1.1, and 2) were similar, revealing in order of prevalence LiCl and $NdCl_3$ in all three runs and possibly Nd in run 2. The XRD patterns for bottoms products from runs 1, 1.1, and 2 are shown in Figure 5.8.

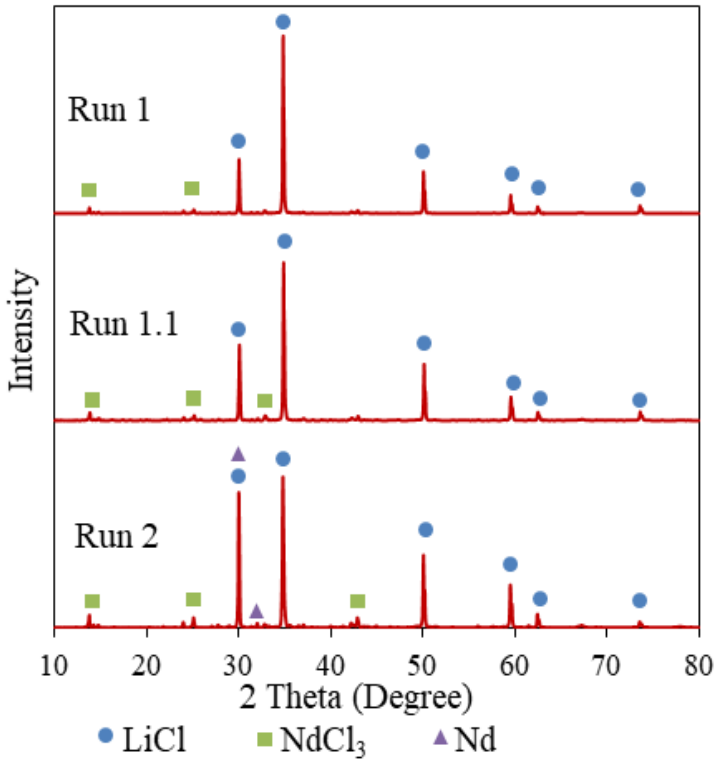

Figure 5.8. XRD patterns for chloride bottoms products from runs 1, 1.1, and 2.

The XRD patterns for the samples of bromide bottoms products (runs 3, 3.1, and 4) were similar, revealing in order of prevalence LiBr and $NdBr_3$ for each of these runs. The XRD patterns for bottoms products from runs 3, 3.1, and 4 are shown in Figure 5.9.

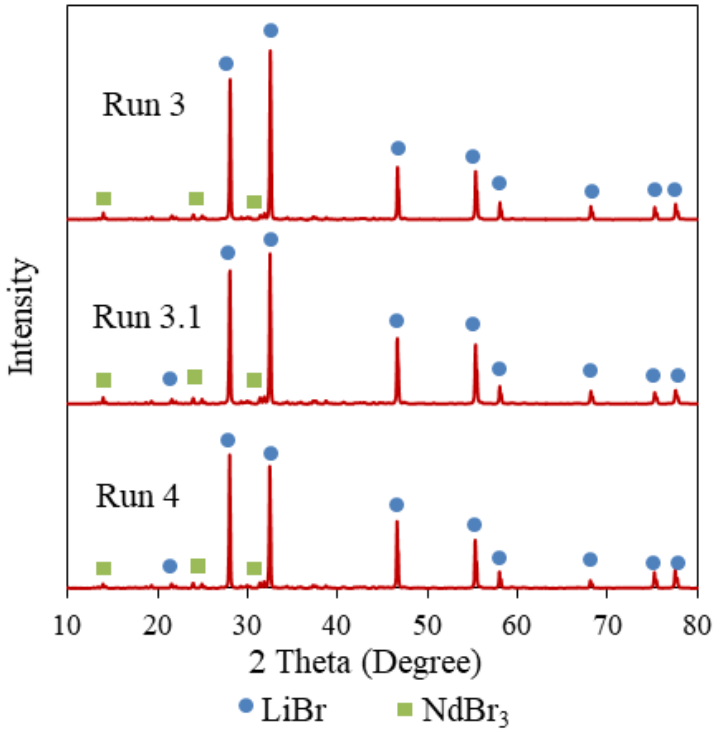

Figure 5.9. XRD patterns for bromide bottoms products from runs 3, 3.1, and 4.

The XRD patterns for chloride distillate products from runs 1 and 2 were similar, each revealing in order of prevalence NH_4Cl and $(Al(NH_3)_4Cl_2)(AlCl_4)$, while NH_4AlCl_4 was an additional compound identified in run 1. The XRD pattern for run 1.1 only revealed the presence of NH_4Cl. The XRD patterns for distillate products from runs 1, 1.1, and 2 are shown in Figure 5.10.

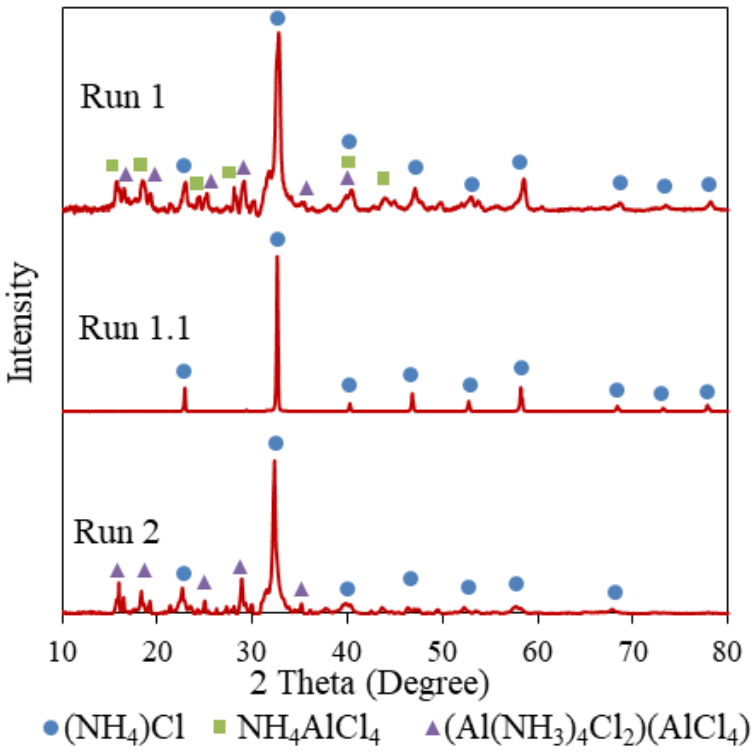

Figure 5.10. XRD patterns for chloride distillate products from runs 1, 1.1, and 2.

The XRD patterns for bromide distillate products from runs 3 and 4 were similar, each revealing in order of prevalence NH_4Br and $(AlBr_3)(NH_3)_5$. The XRD pattern for run 3.1 only revealed the presence of NH_4Br. The XRD patterns for distillate products from runs 3, 3.1, and 4 are shown in Figure 5.11.

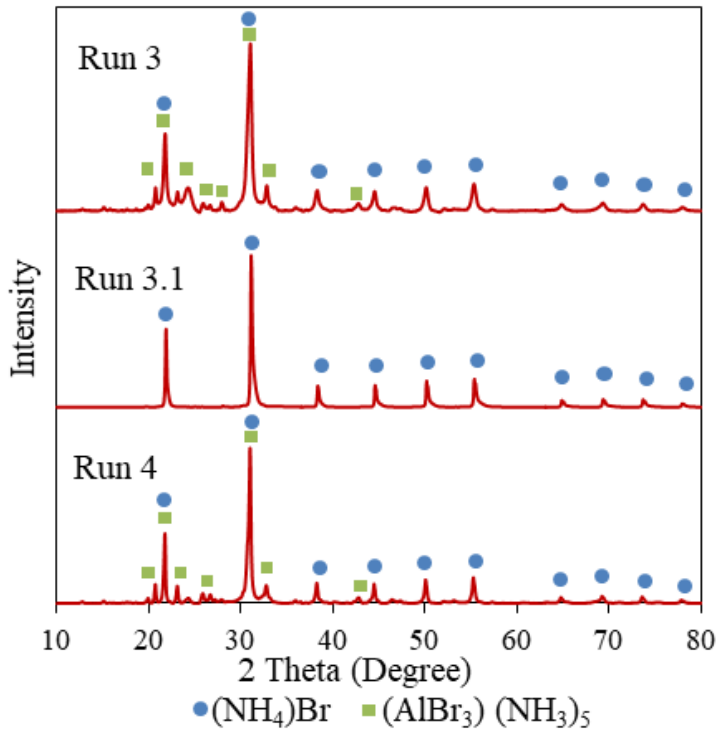

Figure 5.11. XRD patterns for bromide distillate products from runs 3, 3.1, and 4.

As a multicomponent material, the XRD patterns for the waste form product from run 5 identified a variety of compounds, including mixed sodium-magnesium chloride, sodium chloride, magnesium aluminate, magnesia, and possibly a mixed sodium-aluminum chloride. The XRD pattern for the product from run 5 is shown in Figure 5.12.

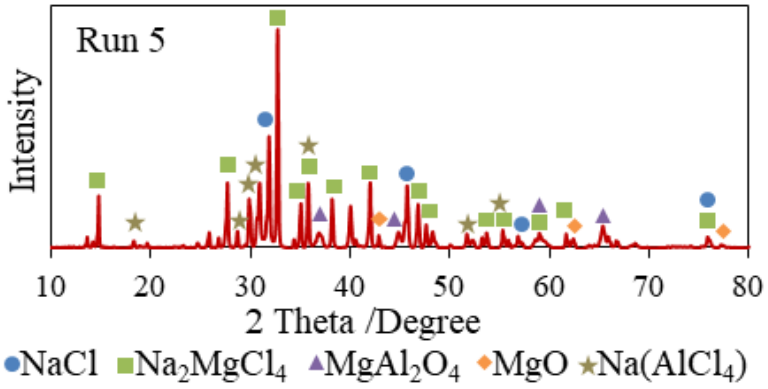

Figure 5.12. XRD pattern for waste form from run 5.

5.5 Discussion

The series of halogenation and waste form runs demonstrated specific dissolution and separation techniques using non-radiological materials and simplified approaches to address the following primary issues, which included (1) the extents of aluminum and neodymium separation as a function of metal feed forms (i.e., powder versus foil) and halogenating agents (chloride versus bromide) and (2) how to stabilize the generated aluminum halide distillate product. Another issue is how the techniques in this demonstration might apply to used ATR fuel.

The performance of this series of halogenation runs was consistent with the identified reaction mechanism in Eq. 5.1, as evidenced by material balances and characterized product compositions. The theoretical compositions of reaction products per Eq. 5.1 for the series of halogenation runs were calculated based on feed material inputs and the following assumptions. First, the prescribed blends of metal powders, aluminum foil, ammonium halide, and lithium halide in a new glass jar each run did not completely transfer to the glassy carbon crucible in all cases, as some residual powder adhered to the inner jar walls. It was assumed that the mixtures that were transferred to the glassy carbon crucible for each run contained the same proportions of materials that were initially loaded in the respective glass jars. Second, all the nitrogen and hydrogen from the ammonium halides, as well as any excess ammonium halide, separated from the bottoms as an off gas. Third, all the neodymium metal was converted to its respective halide upon reaction with ammonium halide and fused with its respective lithium halide. Fourth, all the aluminum metal was converted to its respective halide upon reaction with ammonium halide and volatilized away from the fused salt phase. Finally, the ammonium halide in contact with the crushed bottoms

products of runs 1.1 and 3.1 volatilized away from the fused salt and collected in the off-gas trap, leaving the mass of the bottoms unchanged. Accordingly, the calculated masses of the bottoms for each of the halogenation runs are compared with their respective measured masses from Table 5.2 for comparison in Table 5.4.

Table 5.4. Calculated versus measured masses of bottoms for runs 1 – 4.

grams \ Run	**1**	**1.1**	**2**	**3**	**3.1**	**4**
Measured	58.418	54.526	59.377	63.427	59.069	65.262
Calculated	58.845	54.593	58.717	63.797	59.318	63.625
Meas. / Calc.	99.3%	99.9%	101.1%	99.4%	99.6%	102.6%

A 99.3% ratio of measured to calculated mass of bottoms in run 1 suggests that essentially all the aluminum in the mixture reacted and separated from the bottoms, which is consistent with product characterization analyses. Specifically, aluminum in the bottoms fraction was below detection levels, and no lithium or neodymium was detected in the distillate fraction. Proportioning the mass of loaded aluminum in this run to that of neodymium correlates to an extent of aluminum removal of >97%. The XRD analysis of the distillate product for this run identified the presence of aluminum chloride in combination with ammonia and excess ammonium chloride in the forms of $(Al(NH_3)_4Cl_2)(AlCl_4)$ and NH_4AlCl_4, respectively. Additionally, a separate phase of excess ammonium chloride was identified in the distillate product.

In run 1.1, the bottoms mass was little changed from the loaded crushed product, suggesting that essentially all the aluminum metal from this batch had reacted and volatilized away from the bottoms in the first run. However, a larger sample size of the bottoms

revealed a detectable fraction of aluminum, correlating to 98.2% removal. The fact that additional excess ammonium chloride did little if anything to remove aluminum metal suggests that the aluminum in the bottoms fraction was no longer in a metallic state. The absence of aluminum chloride and the sole presence of ammonium chloride in the XRD analysis of the distillate fraction corroborates the absence of aluminum metal in the bottoms.

In run 2, a 101.1% ratio of measured to calculated mass in the bottoms suggests that a 10% excess of ammonium chloride was insufficient to react all the aluminum metal, which is likely due to the addition of aluminum foil. The aluminum content in the bottoms equated to a 94.5% extent of aluminum removal, while no lithium or neodymium was detected in the distillate fraction. Like run 1, the XRD analysis of the distillate product for run 2 identified the presence of aluminum chloride in combination with ammonia and excess ammonium chloride.

The bromination runs 3, 3.1, and 4 produced similar results to those of the corresponding chlorination runs. More than 95% of aluminum metal was removed from the loaded salt-metal blend in run 3, based on minimum detection levels of aluminum in the bottoms. Exposure of the bottoms from run 3 to additional excess ammonium bromide in run 3.1 yielded a detectable fraction of aluminum via ICP-OES in the distillate, even though only ammonium bromide was detected in the distillate via XRD. Aluminum at 1490 ppm was detected in the bottoms fraction of run 3.1, which equated to a 97.8% extent of removal. This extent of removal was nearly identical to that of the corresponding chlorination run despite additional loading of ammonium bromide, again suggesting that the remaining aluminum in the bottoms fraction was non-metallic. The extent of aluminum removal in run

4 was 91.4%, underscoring the more challenging removal of aluminum in a foil form as opposed to powder.

In bromination runs 3, 3.1, and 4 no lithium or neodymium was detected in the distillate fraction via ICP-OES or XRD. Ammonium bromide was identified in each of the distillate fractions, while aluminum bromide in combination with ammonia was the primary compound in the distillate fractions for runs 3 and 4.

In short, halogenation runs 1 – 4 with their accompanying repeat runs proceeded in accordance with the reaction mechanism identified in Eq. 5.1 with varying extents of aluminum removal. No lithium or neodymium halides were detected in any of the distillate products. The identification of ammonia compounds with aluminum chloride and bromide distillates in runs 1 – 4 suggests that ammonia did not appreciably decompose into nitrogen and hydrogen gases, as suggested by the equilibrium models (see Figure 5.3). Excess ammonium halides were identified in all the distillate products, showing how their sublimed decomposition products (i.e., hydrogen halide and ammonia gases) recombined in the off-gas system.

The fine, low bulk density particulate form of the distillate products is not a preferable form for direct disposal. Consequently, a separate run 5 was performed with aluminum chloride distillate from run 2 to demonstrate a preferable waste form. The run proceeded largely in accordance with the reaction mechanism identified in Eq. 5.2 and the equilibrium model from Figure 5.4. Specifically, magnesium oxide reacted with aluminum chloride to form stable magnesium aluminate, a compound of magnesia and alumina, and magnesium chloride. The magnesium chloride formed stable mixed chlorides with the loaded sodium chloride. The product also contained excess sodium chloride, magnesium

oxide, and possibly sodium-aluminum chloride. In short, run 5 demonstrated the conversion of a mobile, low bulk density aluminum chloride bearing powder into an immobilized, consolidated, solid waste form suitable for disposal.

Ammonium halides were used out of convenience in this series of halogenation runs to deliver a hydrogen halide gas to the reactive metals without installing a dedicated gaseous hydrogen halide system. In the halogenation of used ATR fuel, a gaseous halogenation system would be preferable. As such, ammonia gas would not be present in the off-gas system. While neodymium metal was used in this study as a surrogate for uranium metal, which was based on similar intermetallic formations with aluminum, neodymium halide formation is limited to the trivalent state, while uranium exhibits tetra- penta- and hexavalent chlorides. However, uranium in a bromide system would be largely limited to the tetrabromide, as uranium pentabromide decomposes to the tetrabromide and elemental bromine above 80°C. [139] Thus, bromination of used ATR fuel could be less likely to exhibit volatile uranium species than those from a chlorination system.

5.6 Summary and Conclusions

A series of experiments with surrogate materials was performed at bench scale, which successfully demonstrated and characterized a halogenation technique applicable to treatment of used aluminum matrix test reactor fuel. The demonstration utilized neodymium metal as a non-radiological surrogate for uranium metal along with aluminum metal powder and aluminum foil as the primary constituents of an aluminum matrix fuel. Ammonium chloride and bromide were effective at dissolving the metal matrix, causing the respective aluminum halide to gasify and separate from the formed neodymium halide, which then fused with its corresponding lithium halide as a non-reactive diluent. Specifically, a 10% stoichiometric

excess of ammonium chloride removed more than 97% of the aluminum metal in powder form, while the same removed 94.5% of the aluminum metal in a combined form of powder and foil. Similarly, ammonium bromide removed more than 95% of the aluminum metal in powder form, while the same removed 91.4% of the aluminum metal in a combined form of powder and foil. Additions of ammonium halide beyond the 10% stoichiometric value in repeat runs pushed the extents of aluminum removal to 98.2% and 97.8% for the chlorinating and brominating systems, respectively. No neodymium or lithium halides were detected in the off-gas products, which were limited to compounds of aluminum halide, ammonia, and excess ammonium halide. A separate experiment was performed with off-gas product from one of the chlorination runs, which successfully reacted and consolidated the fine, low bulk density material with magnesia and sodium chloride into a solid matrix of magnesium-aluminum oxides and sodium-magnesium chlorides. This study identified a viable technique for use with aluminum matrix test reactor fuels, including used ATR fuel. Demonstration of this technique with unirradiated aluminum matrix fuel to address the fate of uranium halides would be a logical next step.

6. Deactivation of Sodium Metal for Disposition of Bond Sodium from Used EBR-II Fuel

Forthcoming in *Journal of Nuclear Fuel Cycle and Waste Technology*, "Controlled Conversion of Sodium Metal from Nuclear Systems to Sodium Chloride"

6.1 Objectives

The objective of this study was to expand the investigation of deactivation methods for bond sodium by using a non-metal chloride in combination with, or separate from, a metal chloride. Specifically, the deactivation of molten sodium metal at bench-scale with ammonium chloride and ferrous chloride per the following reaction mechanisms was investigated. [33]

$$2\ Na + 2\ NH_4Cl \rightarrow 2\ NaCl + N_2(g) + 4\ H_2(g) \qquad \Delta H_{Rx,330C} = -208\ kJ \qquad (6.1)$$

$$2\ Na + FeCl_2 \rightarrow 2\ NaCl + Fe \qquad \Delta H_{Rx,330C} = -489\ kJ \qquad (6.2)$$

Once formed, the sodium chloride (melting point of 801°C) was consolidated "as is" or it was mixed with sufficient ferrous chloride to form a eutectic mixture of ferrous chloride and sodium chloride with a melting point of 374°C. [140]

6.2 Experimental Aspects

6.2.1 Approach

The approach for this experimental study was to load 1 g of sodium metal into a boron nitride crucible (Kurt J. Lesker Co.) and heat it on a hot plate (Cole Parmer, StableTemp) to a nominal temperature range of 300 – 330°C. Ammonium chloride or ferrous chloride particulate was incrementally added to the molten sodium on the hot plate

and stirred with a 6-mm diameter glassy carbon rod (SIGRADUR). Periodically the sodium-salt mixture was placed in a box furnace (Thermo Scientific, Thermolyne) for several minutes at 330°C. After an accumulated stoichiometric addition of ammonium chloride or ferrous chloride, the salt-metal mixture was placed in the furnace and heated to 400°C for approximately 30 minutes to gasify any remaining ammonium chloride (sublimation point of 338°C), as applicable. Additional ammonium chloride or ferrous chloride, amounting to 10% of the stoichiometric value for the initial sodium loading, was then stirred into the reaction product on the hot plate. The mixture was then placed in the furnace at 400°C for approximately 2 hours, after which the furnace was de-energized and allowed to cool to ambient. A mid-run sample of the loose particulate product was taken, after which sufficient ferrous chloride was added, as applicable, to the product and heated to 700°C to form a eutectic mixture with the generated sodium chloride. Otherwise, the loose particulate product was heated to consolidation at 850°C for approximately 1 hour. The consolidated products were allowed to cool to ambient, after which they were crushed and ground to a powder for sampling. The procedure was repeated for the series of three runs, as outlined in Table 6.1. The series of runs was performed in an argon atmosphere glovebox (MBRAUN LABmaster dp) with a purification system that maintained oxygen and moisture concentrations over the course of the experiments below 10 ppm and 0.1 ppm, respectively.

Table 6.1. Operating conditions for series of sodium metal deactivation runs.

Run	Mixture	Heating	Sampling
1	Na, NH_4Cl (100% of stoichiometric)	300 – 330°C, 400°C	n/a
	+ NH_4Cl (10% of stoichiometric)	400°C	mid-run sample of loose particulate product;
	+ $FeCl_2$ (for eutectic mixture with NaCl)	700°C	crushed final sample of consolidated product
2	Na, NH_4Cl (100% of stoichiometric)	300 – 330°C, 400°C	n/a
	+ NH_4Cl (10% of stoichiometric)	400°C	mid-run sample of loose particulate product;
	No addition	850°C	crushed final sample of consolidated product
3	Na, $FeCl_2$ (100% of stoichiometric)	300 – 330°C, 400°C	n/a
	+ $FeCl_2$ (10% of stoichiometric)	400°C	n/a
	+ $FeCl_2$ (for eutectic mixture with NaCl)	700, 850°C	crushed final sample of consolidated product

6.2.2 Test Specific Materials

The sodium metal loading for each deactivation run was cut from a block (Alfa Aesar, 99.8%) and further sized to remove oxidized surfaces, as shown in Section 3.2.1.4. Ammonium chloride is hygroscopic and was not available in a high-purity anhydrous form from suppliers. Consequently, the ammonium chloride (Alfa Aesar, 99.999%, Puratronic) used in this study was dried and sieved to a desired particle size using a bench-top box furnace in a separate argon atmosphere glovebox. Specifically, the procured granular ammonium chloride was loaded into trays and heated to 120°C for at least 20 hours, followed by heating at 140°C for at least four hours. The dried material was crushed and sieved to particle sizes below 20-mesh. Ferrous chloride (Sigma Aldrich, 99.99%) was procured as anhydrous -10 mesh beads packaged under argon. It was crushed to approximate the size of the ammonium chloride for sodium deactivation. Additional information on the preparation of ammonium chloride and ferrous chloride is described in Section 3.2.2.1.

6.2.3 Sample Characterization

Product samples from the series of deactivation runs were ground into fine powders and characterized using XRD (Rigaku SmartLab, Cu Kα, 40 kV and 44 mA). The XRD data were collected between 10 – 80° with a step of 0.04° at 4° per min.

6.3 Operations and Results

In the first run, sodium metal was loaded into a boron nitride crucible, heated, and deactivated as described. Initially, the molten sodium metal contacted the crucible bottom and wall. Upon addition of ammonium chloride particles to the surface of the sodium, no sputtering or other signs of a vigorous reaction were observed. Upon stirring, the ammonium

chloride particles moved through the sodium to the bottom of the crucible. Upon continued additions and stirring of ammonium chloride, the molten sodium metal soon formed a ball atop a bed of loose particulate reaction product. The ball of sodium gradually decreased in size upon continued ammonium chloride additions and stirring. No bulk sodium metal was observed after the last addition of ammonium chloride, leaving behind a loose particulate with a violet hue. However, the violet hue subsided after adding additional ammonium chloride (10% of stoichiometric) and heating the product at 400°C. The progression of sodium metal deactivation for run 1 is shown in Figure 6.1.

Figure 6.1. Progression of sodium metal deactivation for run 1 from left to right, top to bottom.

A mid-run sample of the loose fill product was taken, after which the product was blended with ferrous chloride and heated for consolidation. A molten product with slight, reddish-brown fuming was observed at 700°C, prior to de-energizing the furnace. After

cooldown, a consolidated product was observed that was fixed to the boron nitride crucible. Dark material was also observed adhering to the inner and outer walls of the crucible, as shown in Figure 6.2.

Figure 6.2. Final consolidated products for runs 1 – 3 from left to right.

The second run proceeded similarly to the first run with the exception that the mid-run product was transferred from the boron nitride crucible to a glassy carbon crucible (SIGRAGUR) for consolidation at 850°C. The consolidated product from run 2 separated from the crucible in translucent colorless shards, as shown in Figure 6.2.

Upon early additions and stirring of ferrous chloride in molten sodium in run 3, a dark precipitate formed, and the sodium metal pool took on a concave shape, wetting the walls of the boron nitride crucible. Midway through the incremental ferrous chloride additions, a slurry consistency formed. The mixture was placed in the furnace for several minutes. A temperature spike on the furnace control thermocouple was observed along with significant reddish-brown fumes. Upon returning the mixture to the hot plate, the sodium's metallic sheen was gone. Addition of the balance of ferrous chloride was difficult due to the increasingly hardened consistency of the product. Given the questionable homogeneity and

hardness of the product, no mid-run sample was taken. The eutectic addition of ferrous chloride was added to the product, but not well mixed before proceeding with consolidation. Some fuming of the product in the furnace was observed at 700°C, but the product was not completely molten. Consequently, the furnace temperature was raised to 850°C, at which point significant fuming was observed along with a molten product. The furnace was de-energized, and the product was allowed to cool to ambient. After cooldown, a dark consolidated product with some loose reddish-brown exfoliated material on the surface was observed. The product was fixed to the boron nitride crucible, and material was observed on the inner and outer walls of the crucible, as shown in Figure 6.2. A progression of the sodium deactivation for run 3 is shown in Figure 6.3. A summary of feed material masses for the series of runs is shown in Table 6.2.

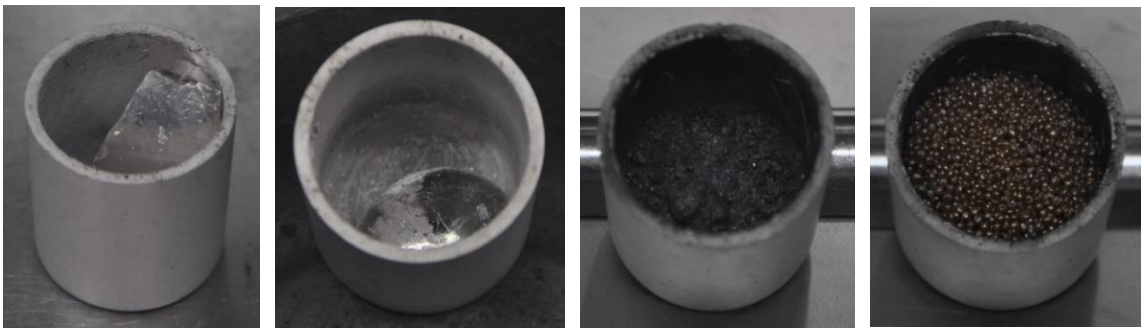

Figure 6.3. Progression of sodium metal deactivation for run 3 showing from left to right: cut sodium, molten sodium, mid-run product, and mixture before consolidation.

Table 6.2. Summary of feed material masses for series of deactivation runs.

Run	**Na (grams)**	**NH_4Cl (grams)**	**$FeCl_2$ (grams)**
1	1.003	2.387 + 0.265 = 2.652	4.022
2	1.012	2.355 + 0.266 = 2.621	n/a
3	1.002	n/a	2.762 + 4.599 = 7.361

The consolidated products for runs 1 and 3 were broken and separated from their respective boron nitride crucibles. The products from all three runs were crushed and ground to a powder, from which random grab samples of the homogenized materials were taken and analyzed via XRD. The XRD patterns for each of the sample products are shown as a combined plot in Figure 6.4. Identified compounds for the respective XRD patterns are summarized in Table 6.3.

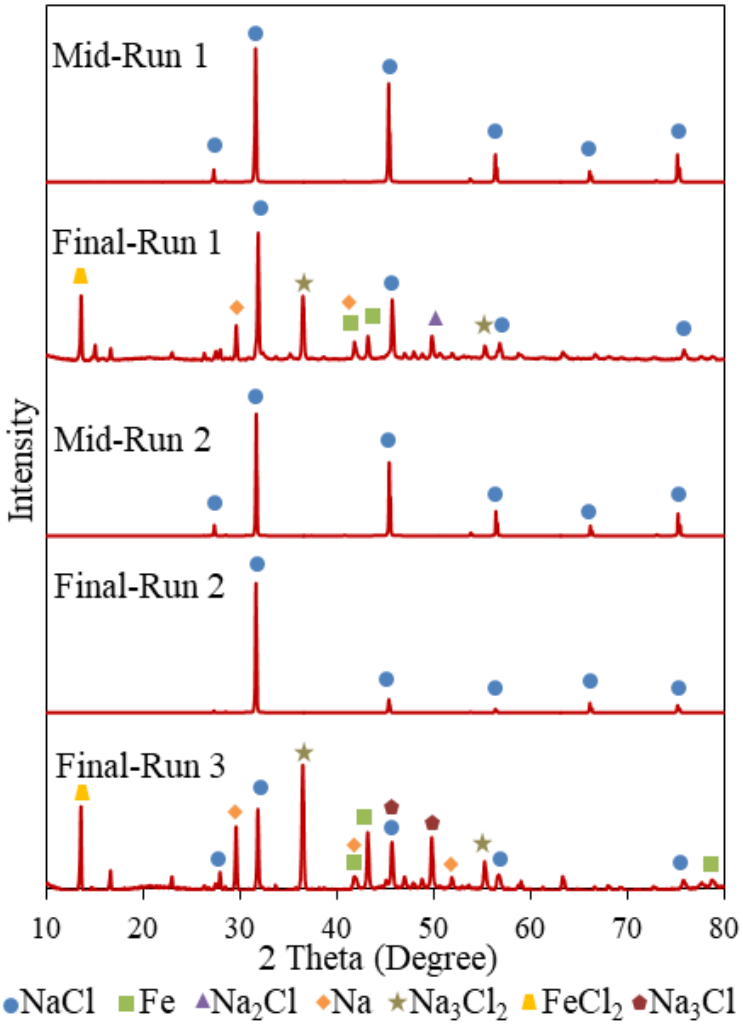

Figure 6.4. XRD patterns for sample products.

Table 6.3. Summary of identified compounds in product samples for series of deactivation runs.

Run	Sample	Identified Compounds
1	Mid-run	NaCl
	Final	NaCl, $FeCl_2$, Fe, Na, Na_3Cl_2, Na_2Cl
2	Mid-run	NaCl
	Final	NaCl
3	Final	NaCl, $FeCl_2$, Fe, Na, Na_3Cl_2, Na_3Cl

6.4 Discussion

Ammonium chloride decomposes upon reaching its sublimation point at 338°C into its component gases, hydrogen chloride and ammonia, via the following reaction.

$$NH_4Cl \rightarrow HCl(g) + NH_3(g) \quad (6.3)$$

In contact with sodium metal, hydrogen chloride reacts to form sodium chloride and hydrogen gas, while ammonia reacts to form sodium amide and hydrogen gas via the following reactions.

$$Na + HCl(g) \rightarrow NaCl + \tfrac{1}{2} H_2(g) \quad (6.4)$$

$$Na + NH_3(g) \rightarrow NaNH_2 + \tfrac{1}{2} H_2(g) \quad (6.5)$$

Sodium amide has some interesting properties with a reported melting point of approximately 200°C and decomposition to its elements above 400°C per the following reactions. [141]

$$NaNH_2\ (s) \xrightarrow{T=200\ ^\circ C} NaNH_2\ (l) \xrightarrow{T>400\ ^\circ C} Na\ (l) + H_2(g) + \tfrac{1}{2}\ N_2(g) \qquad (6.6)$$

Indeed, the cracking of ammonia gas in a sodium metal-sodium amide system per the following reaction mechanism has been proposed as a way of storing and delivering hydrogen for a hydrogen-based energy sector. [142]

$$2\ NH_3(g) \xrightarrow{Na+NaNH_2} N_2(g) + 3\ H_2(g) \qquad (6.7)$$

However, in the presence of hydrogen chloride gas, sodium amide reacts to form sodium chloride along with hydrogen and nitrogen gases per the following reaction.

$$2\ NaNH_2 + 2\ HCl(g) \rightarrow 2\ NaCl + N_2(g) + 3\ H_2(g) \qquad (6.8)$$

Given the formation of sodium amide as an intermediate compound in the reaction between sodium metal and ammonia chloride, combinations of Eqs. 6.3 – 6.8 sum to Eq. 6.1.

The deactivation of sodium metal (with a melting point of 98°C) in a temperature range of 300 – 330°C was selected to provide sufficient superheat for a molten sodium phase while precluding the flash sublimation of ammonium chloride. This operating temperature range along with a metered and stirred addition of ammonium chloride resulted in a controlled reaction of sodium metal per the foregoing reaction mechanisms. A subsequent addition of a 10% stoichiometric excess of ammonium chloride and exposure to 400°C produced a pure loose sodium chloride particulate, as evidenced by XRD analysis of the mid-run products for runs 1 and 2 (see Figure 6.4).

The addition of ferrous chloride to the mid-run 1 product served to lower the melting point needed to consolidate the sodium-ferrous chloride product. Some reddish-brown fuming was observed during the consolidation step, which was attributed to ferrous chloride with a vapor pressure at 700°C of 1700 Pa compared to 3 Pa for pure sodium chloride. [33]

The melting point suppression from a ferrous chloride addition to sodium chloride comes at an expense, as the theoretical volume and mass of the consolidated product are roughly double and triple those, respectively, of pure sodium chloride. Furthermore, the possible presence of sodium and iron metal in the consolidated product via XRD (see Figure 6.4) is troubling, which would require further investigation to determine its validity and origin. On the other hand, the consolidation of the mid-run 2 product at 850°C yielded a pure sodium chloride (see Figure 6.4) that separated readily from a glassy carbon crucible.

The deactivation of sodium metal with ferrous chloride (m.p. = 677°C) was performed in a temperature range of 300 – 330°C for direct comparison to the ammonium chloride runs. As described, the intermediate product was a dark thick slurry, which made further mixing of the reactant difficult. Furthermore, uncontrolled reaction of the mixture occurred upon heating in a furnace, as evidenced by spikes in furnace thermocouple readings and reddish-brown fuming. With a melting point of 677°C it is likely that surfaces of ferrous chloride particles became passivated without completely reacting upon their addition and stirring in molten sodium at approximately 300 – 330°C on a hot plate. After heating in a furnace at 330°C, the passivation layers were likely breached, allowing the ferrous chloride-sodium metal reaction to proceed at an accelerated rate. As shown in Eqs. 6.1 and 6.2, the heat of reaction from ferrous chloride and sodium metal is substantially higher than that from ammonium chloride and sodium metal. Specifically, the former heat of reaction could have led to melting, accelerated reaction with sodium, and fuming of ferrous chloride along with an accompanying temperature spike of the furnace thermocouple.

The formation of an iron product in run 3 likely contributed to the spreading of sodium as it wetted the metal product, which was in stark contrast to the balling of molten

sodium upon reaction in runs 1 and 2. The stiff consistency of the mid-run 3 product also contrasted sharply to the loose particulate midway through runs 1 and 2. The stiff consistency precluded the mixing of additional ferrous chloride prior to consolidation of the run 3 product, which necessitated stepping the operating temperature from 700 to 850°C to obtain sufficient superheat to melt the mixture. Characterization of the run 3 final product identified the possible presence of sodium metal, suggesting an incomplete conversion of the feed material to its chloride.

6.5 Summary and Conclusions

A series of three runs was performed to assess the conversion of sodium metal to sodium chloride separately with ammonium chloride and ferrous chloride. Metering and stirring a stoichiometric addition of ammonium chloride into molten sodium at a temperature range of 300 – 330°C successfully produced a loose particulate product with a violet hue and no observable sodium metal in two separate runs. Deactivation of the sodium metal in these two runs proceeded without sputtering or other signs of reaction excursion. Mixing a 10% stoichiometric excess of ammonium chloride into the violet particulate products and heating to 400°C formed colorless loose particulate products, which were characterized as pure sodium chloride. One batch of loose sodium chloride particulate was successfully consolidated upon heating to 850°C, forming pure translucent sodium chloride. The other was successfully consolidated upon blending with ferrous chloride and heating at 700°C, although some fuming of the product was observed. Further investigation into the makeup of the latter product is needed to assure the complete absence of sodium metal.

It proved challenging to deactivate sodium metal with ferrous chloride using the same approach as with ammonium chloride, as evidenced by (1) the inability to adequately blend

the reactant with the sodium metal and its attendant reaction products and (2) reaction excursions and the accompanying fuming of the product. Consolidation of the product in the third run required a higher than anticipated temperature, i.e., 850°C in lieu of 700°C, resulting in significant fuming of the product. Furthermore, characterization of the final product from the third run exhibited the possible presence of sodium metal. Consequently, it is not recommended to deactivate sodium metal directly with ferrous chloride under the operating conditions applied in this study. In fact, the benefit of adding ferrous chloride to pure sodium chloride particulate to afford a slightly lower consolidation temperature is questionable. In short, deactivation of sodium metal with ammonium chloride in this study identified a controlled conversion of the metal to its chloride. This method lends itself well to deactivating bond sodium, which may contain high levels of radioactively and are consequently handled in remotely operated inert-atmosphere environments.

This page intentionally left blank

7. Synthesis of High-Purity Uranium Trichloride

Forthcoming in *Journal of Nuclear Materials*, "Synthesis and Characterization of High-Purity Uranium Trichloride in Alkali-Metal Chloride Media"

7.1 Objectives

The objective of this experimental study was not to produce isolated uranium trichloride, but rather a concentrated high-purity uranium trichloride in alkali-metal chloride media at bench scale. Specifically, uranium metal powder and uranium hydride powder were contacted separately with ammonium chloride in one of the identified alkali-metal chloride media under heat to produce molten salt solutions containing uranium trichloride, per the following anticipated reaction mechanisms. [33]

$$U + 3\ NH_4Cl \rightarrow UCl_3 + 3\ NH_3(g) + 3/2\ H_2(g) \qquad \Delta G_{Rx,338C} = -416\ kJ \qquad (7.1)$$

$$UH_3 + 3\ NH_4Cl \rightarrow UCl_3 + 3\ NH_3(g) + 3\ H_2(g) \qquad \Delta G_{Rx,338C} = -403\ kJ \qquad (7.2)$$

The ammonium chloride was delivered substoichiometrically for a given mass of uranium feed material to promote the formation of uranium trichloride over uranium tetrachloride in accordance with Eq. 2.53. Furthermore, the bench-scale experiments were conducted using materials that were compatible with a chlorinating environment to preclude impurity introduction into the product.

7.2 Experimental Aspects

7.2.1 Approach

The approach for this experimental study was based on production of a eutectic mixture of uranium trichloride and sodium chloride, i.e., NaCl – 32 mol% UCl_3, which has a

eutectic melting point of 525°C, [143] while the melting point for a similarly proportioned mixture of LiCl-KCl-UCl_3 was expected to be approximately 475°C. [144] The scale of this experimental study was limited to uranium metal feeds of 100 g per batch. Accordingly, 100.000 g of uranium (as metal or hydride powder) was blended in a glass jar with 64.047 g of ammonium chloride, which was sufficient to react with 95% of the uranium in the feed materials. Then 49.566 g of alkali-metal chloride (i.e., sodium chloride or lithium chloride – potassium chloride eutectic) was blended with the uranium feed and ammonium chloride in the same jar. This dry blend was then transferred into a glassy carbon crucible, which was covered and heated to approximately 500°C at 10°C/hr to sublimate ammonium chloride and thereby chlorinate the uranium metal or hydride. The lithium chloride – potassium chloride mixtures were then heated to 650°C at 5°C/min to ensure molten conditions, while the sodium chloride mixtures were heated to 850°C at 5°C/min for the same reason. The furnace cover was then removed, and each molten mixture was stirred momentarily with a glassy carbon rod to ensure homogeneity and verify the absence of any substantial solid phase. A ported cover was then placed atop the crucible, and the melt temperature was lowered to 500°C for the lithium chloride – potassium chloride mixtures and 650°C for the sodium chloride mixtures. A dip sample of the molten salt was taken with a glassy carbon rod, after which a uranium metal rod was suspended in the salt pool to a depth of approximately 1 cm. An electrolytic cell was established between the glassy carbon crucible as the anode and the uranium metal rod as the cathode to electrotransport excess uranium metal in contact with the crucible to the uranium metal rod at a controlled potential for an overnight period. The electrolytic cell was stopped, and the system was left at open circuit for several hours. The uranium rod was removed, and a dip sample of the salt was taken with a glassy carbon rod.

The furnace was de-energized, and the crucible was removed after sufficient cool down. Post-run components and products were weighed and transferred to sealed storage containers for future use. The series of four synthesis runs was performed with the lithium chloride – potassium chloride, ammonium chloride, uranium metal and uranium hydride powders first, followed by those with sodium chloride. A summary of conditions for this series of runs is shown in Table 7.1.

Table 7.1. Conditions for series of uranium trichloride synthesis runs.

Run	Mixture	Heating	Electrolytic Cell
1	U metal, NH_4Cl, LiCl-KCl eutectic	Ambient → 500°C at 10°C/hr 500°C → 650°C at 5°C/min	1 V cell voltage at 500°C
2	UH_3, NH_4Cl, LiCl-KCl eutectic		
3	U metal, NH_4Cl, NaCl	Ambient → 500°C at 10°C/hr 500°C → 850°C at 5°C/min	0.9 V cell voltage at 650°C
4	UH_3, NH_4Cl, NaCl		

7.2.2 Test Specific Equipment

A bench-top jeweler furnace (Kerr, Auto Electro-Melt Furnace, Maxi 3kg) was used to perform the series of synthesis runs. The furnace instrumentation was modified to facilitate ramp rate and cut-out temperature controls. The vendor-provided graphite crucible within the furnace was machined to accommodate a tapered glassy carbon crucible (SIGRADUR, GAT 32, 320 ml). The glassy carbon crucible was fitted with a glassy carbon cover (SIDRADUR, GAD 3), atop which steel wool was placed and around which a steel mesh ring was fitted. The nested crucibles, cover, steel wool, and ring were covered with an

insulated vendor-provided lid, as shown in Figure 7.1, which constituted the configuration of the furnace for heating of the salt mixtures. A separate ported furnace cover was fabricated to replace the vendor-provided lid to facilitate salt sampling and electrolytic cell operations. The various components for the furnace in heat-up and electrolytic cell operations are also shown in Figure 7.1. A 9-mm diameter by 250-mm long glassy carbon rod (SIGRADUR) was used for salt stirring and dip salt sampling.

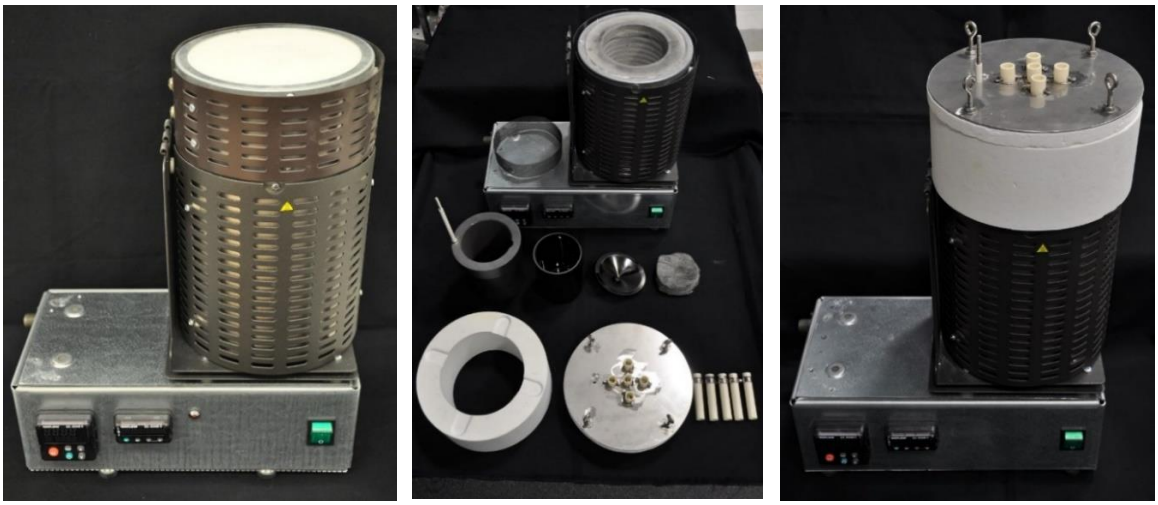

Figure 7.1. Furnace and components for synthesis runs, including heat-up configuration (left), disassembled components (center), and electrolytic cell configuration (right).

An electrolytic cell was established in each molten salt pool during the series of synthesis runs by connecting working and counter electrode leads from a potentionstat (Solartron, model 1287) to a steel rod that was threaded into the graphite crucible and to a uranium rod that was suspended in the salt pool via an electrically insulated furnace cover port. A simplified diagram of the electrolytic cell is shown in Figure 7.2.

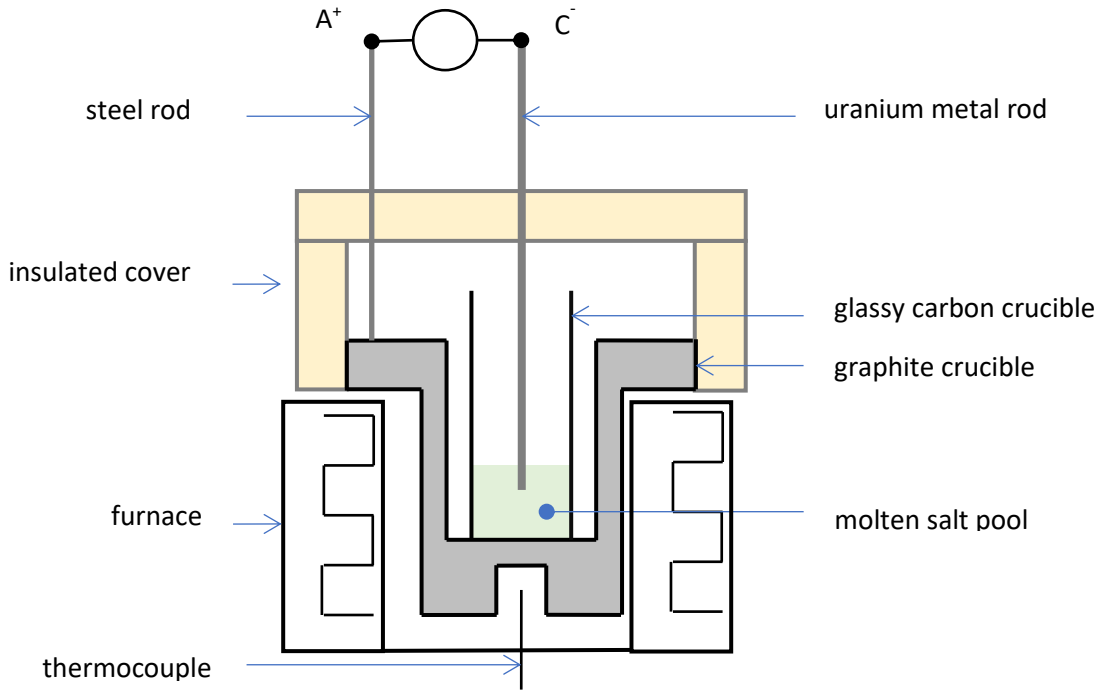

Figure 7.2. Simplified diagram of electrolytic cell for synthesis runs.

The furnace was positioned and operated inside an argon-atmosphere radiological glovebox at INL's FCF (see Section 3.1.2.2). Sealed feedthroughs into the glovebox accommodated electrical leads for the furnace and potentiostat to support the described operations. Ammonia and hydrogen chloride gas detectors (Dräger diffusion tubes) were positioned directly above the furnace and at the opposite end of the glovebox during portions of the latter two synthesis runs.

7.2.3 Test Specific Materials

The primary materials for the series of synthesis runs consisted of uranium feed materials, ammonium chloride, and alkali-metal halide salts, each requiring its own preparation. Specifically, the uranium metal powder was prepared by chopping depleted uranium metal rod (Aerojet Ordnance Tennessee, Inc.) and alternately exposing up to 100 g

of it at a time to vacuum (~30 mTorr) and a pure hydrogen atmosphere (ambient pressure) at nominal 30-minute intervals in a sealed chamber within a horizontal tube furnace at 275 ± 25°C. The furnace was operated in an argon-atmosphere radiological glovebox at INL's Fuels and Applied Science Building (see Section 3.1.2.1). Exposure of the uranium metal to hydrogen gas at temperature promoted the formation of particulate uranium hydride via the following reaction mechanism. [33]

$$U + 3/2\ H_2(g) \rightarrow 4\ UH_3 \qquad \Delta G_{Rx,275C} = -25\ kJ \qquad (7.3)$$

Subsequent vacuum conditions promoted the reverse of Eq. 7.3 to form uranium metal powder. The uranium hydriding/dehydriding cycle was repeated several times, after which the furnace was unloaded, and the product was transferred to a 50-mesh sieve. The uranium metal particles below 50-mesh were collected as feed material for uranium trichloride synthesis runs, while the particles above 50-mesh were reloaded into the furnace along with additional uranium metal pieces, as needed, for uranium metal powder formation. The production of uranium hydride was accomplished by loading 100.000 g of uranium metal powder (i.e., -50 mesh) in the furnace and heating the powder to 275 ± 25°C under a pure hydrogen atmosphere for several hours. The chamber was then unloaded, and the uranium hydride powder was collected as feed material for synthesis runs. Accordingly, 101.000 g and 101.100 g of uranium hydride were prepared for synthesis runs 2 and 4.

Two uranium rods were used in this study – one for contact with the lithium chloride – potassium chloride melts and the other for contact with the sodium chloride melts. Each rod was cast from depleted uranium metal (Aerojet Ordnance Tennessee, Inc.) into 6-mm diameter by 150-mm long rods.

Ammonium chloride is hygroscopic and was not available in a high-purity anhydrous form from suppliers. Consequently, the ammonium chloride (Alfa Aesar, 99.999%, Puratronic) used in this study was dried and sieved to the desired particle size using a bench-top box furnace in an argon atmosphere glovebox. Specifically, the procured granular ammonium chloride was loaded into trays and heated to 120°C for at least 20 hours, followed by heating at 140°C for at least four hours. The dried material was crushed and sieved to particle sizes below 30-mesh.

Lithium chloride – potassium chloride eutectic (Sigma Aldrich, 99.99%, 44 wt% LiCl) and sodium chloride (Sigma Aldrich, 99.999%) were procured as anhydrous -10 mesh beads packaged under argon. Each of these alkali-metal chlorides was crushed and sieved to particle sizes below 30-mesh.

7.2.4 Sample Characterization

Salt samples from the series of synthesis runs, including one before and one after each electrolytic cell conditioning operation for a set of eight samples, were split into additional sample sets and subjected to chemical and microscopic analyses as follows. One set of salt samples was characterized for elemental makeup via ICP-OES. Another set of salt samples was characterized for chemical speciation via XRD. This involved loading each sample onto a tray and sealing it with a domed cover under a dry argon atmosphere to preclude moisture absorption into the sample. Each covered sample was analyzed with a PANalytical AERIS X-ray diffractometer (Malvern Panalytical, LLC), equipped with a Cu Kα source at 40 kV and 15 mA. Scan parameters were 10-110° with a step of 0.0109° and a counting time of 118 s.

The last set of salt samples was characterized with a Titan Themis 200 probe Cs corrected FEG scanning transmission electron microscope, which provided sub-angstrom imaging and spectroscopy. The microscope was equipped with a super-x energy-dispersive X-ray spectroscopy system and a Gatan Continuum system.

7.3 Calculations

The high surface area of uranium metal and uranium hydride feed materials along with the multiple constituent phases that were expected in this series of runs created a complex set of conditions that warranted calculations prior to proceeding with the experiments. Specifically, a model was created to assess possible chemical equilibrium conditions and related reaction mechanisms to ensure that a high-purity uranium trichloride would be produced in the respective media. Additionally, a conservative adiabatic reaction temperature determination was conducted to ensure that a worst-case exotherm in a synthesis run was manageable using the described experimental conditions and equipment configurations.

Chemical equilibrium calculations provide a straightforward means of assessing product compositions as a function of temperature for a given quantity of raw materials. Commercially available software, HSC Chemistry 8, [33] was used to perform such calculations with a Gibbs energy minimization model, which is based on prior work by others. [136] After inputting the defined feed materials for synthesis run 1 and assuming unit activities and ideal mixing, the model produced a plot of possible constituent concentrations as a function of temperature as shown in Figure 7.3. Only the predominant compounds of over 30 selected possible compounds are shown in Figure 7.3. Noteworthy findings from the model are (1) the predominant formation of uranium trichloride compared to an

inconsequential presence of uranium tetrachloride and (2) the decomposition of ammonia into nitrogen and hydrogen gases from possible intermediate interactions with uranium metal. The latter finding suggests overall reaction mechanisms for uranium trichloride synthesis per the following mechanisms in lieu of, or in addition to, those in Eqs. 7.1 and 7.2.

$$U + 3\ NH_4Cl \rightarrow UCl_3 + 3/2\ N_2(g) + 6\ H_2(g) \qquad \Delta G_{Rx,338C} = -467\ kJ \qquad (7.4)$$

$$UH_3 + 3\ NH_4Cl \rightarrow UCl_3 + 3/2\ N_2(g) + 15/2\ H_2(g) \qquad \Delta G_{Rx,338C} = -454\ kJ \qquad (7.5)$$

A similar model was created for synthesis run 2, which produced a nearly identical outcome except for a higher hydrogen concentration owing to the decomposition of uranium hydride. Additional models were generated for synthesis runs 3 and 4 which produced similar outcomes to those from runs 1 and 2, aside from the unchanging presence of sodium chloride in lieu of lithium and potassium chloride.

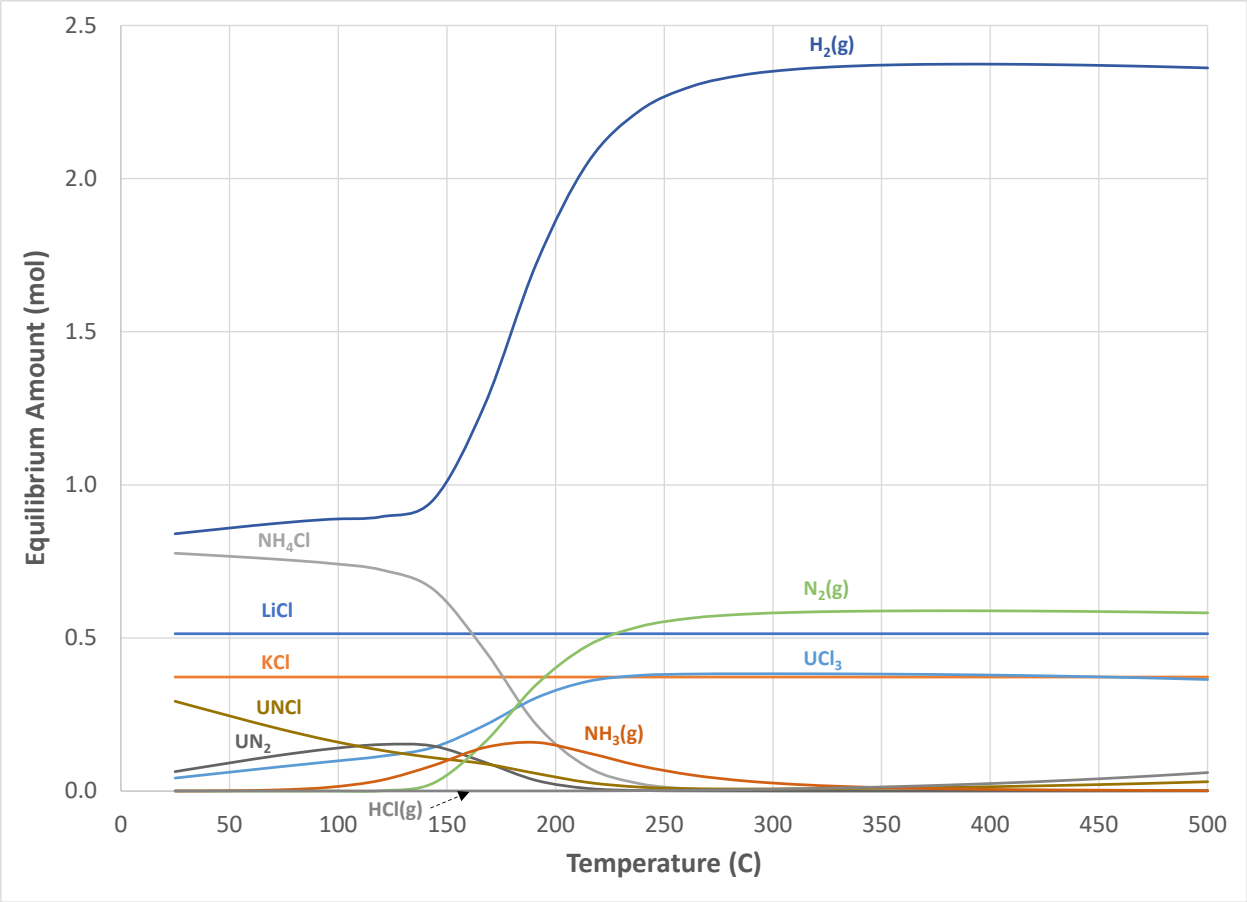

Figure 7.3. Modeled equilibrium constituent concentrations versus temperature for synthesis run 1.

Uranium metal and uranium hydride powders are pyrophoric materials, as they can ignite and rapidly burn in air in an uncontrolled manner. Consequently, these powders were prepared and handled under inert argon atmospheres in this study. However, this study pursued blending of a hydrogen chloride source, in the form of sublimating ammonium chloride, together with a near stoichiometric mass of uranium metal or uranium hydride powder, as opposed to metering one reactive component into the other. Thus, an adiabatic reaction temperature determination was performed per the following energy balance to assess the consequences of an accelerated reaction per Eq. 7.1, which represents runs 1 and 3 with a

worse case exothermic heat of reaction (ΔH_{Rx}) at -86 kJ compared to +48 kJ for runs 2 and 4 per Eq. 7.2. [33]

$$\Delta H_{Rx} = \int_{Ti}^{Tf} \sum n_i * C_{p,i}(T) * dT \qquad (7.6)$$

where: T_i = initial temperature

T_f = final temperature

n_i = stoichiometric moles of reaction product i

C_{pi} = heat capacity of reaction product i

In this calculation it was conservatively assumed that no reaction occurred during heating of a mixture from run 1 or 3 until the sublimation point of ammonium chloride (338°C) was reached, at which point the heat of reaction was fully absorbed by the reaction products alone. Accordingly, the initial temperature used in Eq. 7.6 was 338°C. Given heat capacities as a function of temperature for the reaction products, [33] the final temperature (i.e., adiabatic reaction temperature) per Eq. 7.6 was determined to be 630°C. Thus, an accelerated reaction per Eq. 7.1 was deemed to be sufficiently bounded by the experimental conditions and test configuration, as the adiabatic reaction temperature was below planned operating temperatures of 650 and 850°C for runs 1 and 3, respectively.

7.4 Operations and Results

The prescribed uranium metal powder, ammonium chloride, and lithium chloride – potassium chloride eutectic salts were blended in a 250-ml glass jar, as shown in Figure 7.4, for uranium trichloride synthesis run 1. The mixture was transferred to a pre-weighed glassy carbon crucible, also shown in Figure 7.4. After heating the mixture to 650°C, the furnace lid was removed, and no discoloration of the steel wool or mesh was observed. The molten

solution was stirred, and no substantial solid phase was apparent. Molten salt dip samples were taken, as shown in Figure 7.5, before (designated as sample A) and after (designated as sample B) the described electrolytic cell operations. The uranium metal rod exhibited a net mass loss of 2.518 g. The furnace was de-energized, and the cooled salt ingot separated readily from the glassy carbon crucible. The ingot was dark, as shown in Figure 7.5, with an apparent density of 3.4 g/cc based on mass and gross dimensions.

Figure 7.4. Uranium metal powder, ammonium chloride, and lithium chloride – potassium chloride blend before (left) and after (right) loading in glassy carbon crucible.

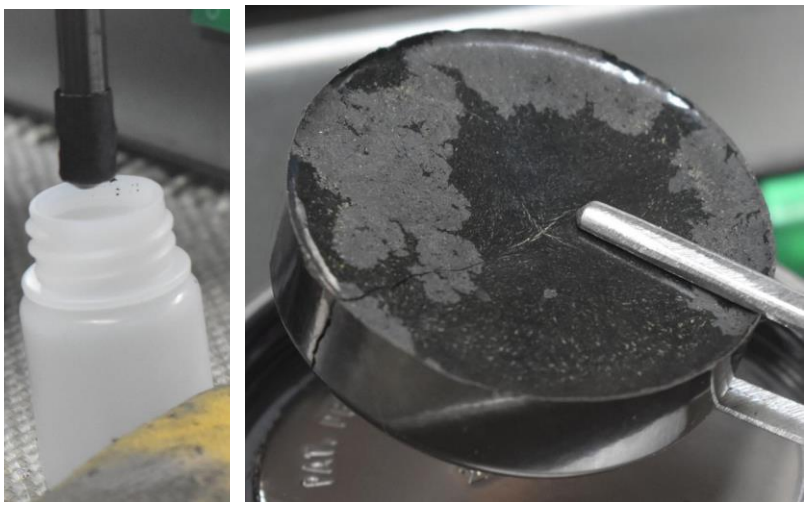

Figure 7.5. Dip sample of molten salt after electrolytic cell operations in synthesis run 1 (left) and post-run salt ingot (right).

The procedure was repeated for uranium trichloride synthesis runs 2 – 4, as outlined in Table 7.1. Notable mass measurements for each of the runs are listed in Table 7.2. No discoloration or notable increase in mass was observed on the steel wool or ring throughout the runs, nor was any substantial solid phase detected prior to electrolytic cell operations. Small decreases in mass were observed in the respective uranium metal rods for runs 1, 3, and 4, while a slight increase in mass was observed on the rod for run 2. Each of the product salt ingots from runs 1 – 4 were similar in appearance and size. No degradation or notable change in mass was observed in the glassy carbon crucible throughout the series of runs.

Table 7.2. Summary of recorded masses from uranium trichloride synthesis runs 1 – 4.

grams	Run 1	Run 2	Run 3	Run 4
Mixture in crucible	213.493	214.484	213.488	214.645
Salt sample A	1.512	2.207	0.574	0.720
Salt sample B	1.192	1.112	0.907	1.341
Change in uranium rod	-2.518	+0.033	-2.252	-2.926
Salt ingot	192.505	188.996	191.836	192.766

Ammonia gas detection tubes were positioned directly above the furnace (near) and at the opposite end of the glovebox (far) for run 3. The near and far tubes read 500 and 200 ppm-hr, respectively, after 25 hours of run time with the furnace at 280°C, while the same read 1500 (maximum reading) and 800 ppm-hr, respectively, after 47 hours of run time with the furnace at 500°C.

Both ammonia and hydrogen chloride gas detections tubes were positioned in pairs near and far from the furnace for run 4. The near and far ammonium gas detection tubes read 1300 and 700 ppm-hr, respectively, after 22 hours of run time with the furnace at 250°C, while the same read 1500 (maximum reading) and 800 ppm-hr, respectively, after 27 hours of run time with the furnace at 300°C. The near ammonium gas detection tube remained at 1500 ppm-hr after 47 hours of run time with the furnace at 500°C, while the far tube read 1100 ppm-hr. At no point during run 4 did either hydrogen chloride gas detection tube indicate a presence of the gas.

Each of the eight salt samples from runs 1 – 4 were split roughly in half to support post-run characterization. The first set of samples was subjected to analysis of the primary

elements in the samples via ICP-OES, the results of which with a margin of error of ± 5% at 2 sigma are shown in Table 7.3.

Table 7.3. Salt sample elemental analysis results.

ppm	**Run 1**		**Run 2**		**Run 3**		**Run 4**	
Sample	**A**	**B**	**A**	**B**	**A**	**B**	**A**	**B**
U	513,000	508,000	506,000	484,000	441,000	458,000	451,000	447,000
K	78,700	74,500	83,000	79,000	--	--	--	--
Li	20,000	18,900	21,100	19,600	--	--	--	--
Na	--	--	--	--	97,500	95,900	92,500	92,200

The second set of eight samples were ground to a powder in an argon atmosphere glovebox, from which XRD and STEM sample mounts were prepared. The XRD patterns of samples from runs 1 and 2 are shown in Figures 7.6, while those for runs 3 and 4 are shown in Figure 7.7. STEM images of samples 1A, 2A, 3A, and 4A are shown in Figure 7.8, while those for samples 1B, 2B, 3B, and 4B are shown in Figure 7.9. Compositions of the samples from runs 1 – 4, based on EDS from images in Figures 7.8 and 7.9, are listed in Table 7.4. A STEM-EDS map of sample 1A is shown in Figure 7.10.

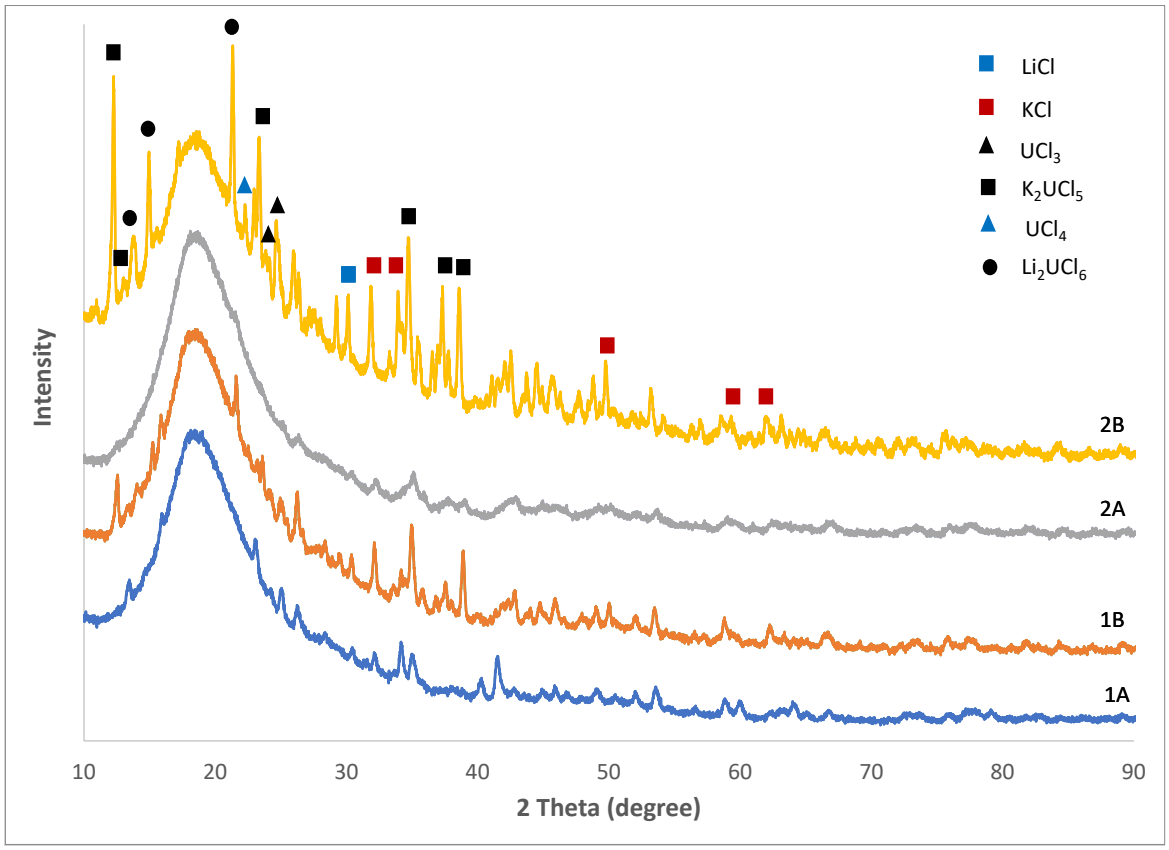

Figure 7.6. XRD patterns of sample material from runs 1 and 2.

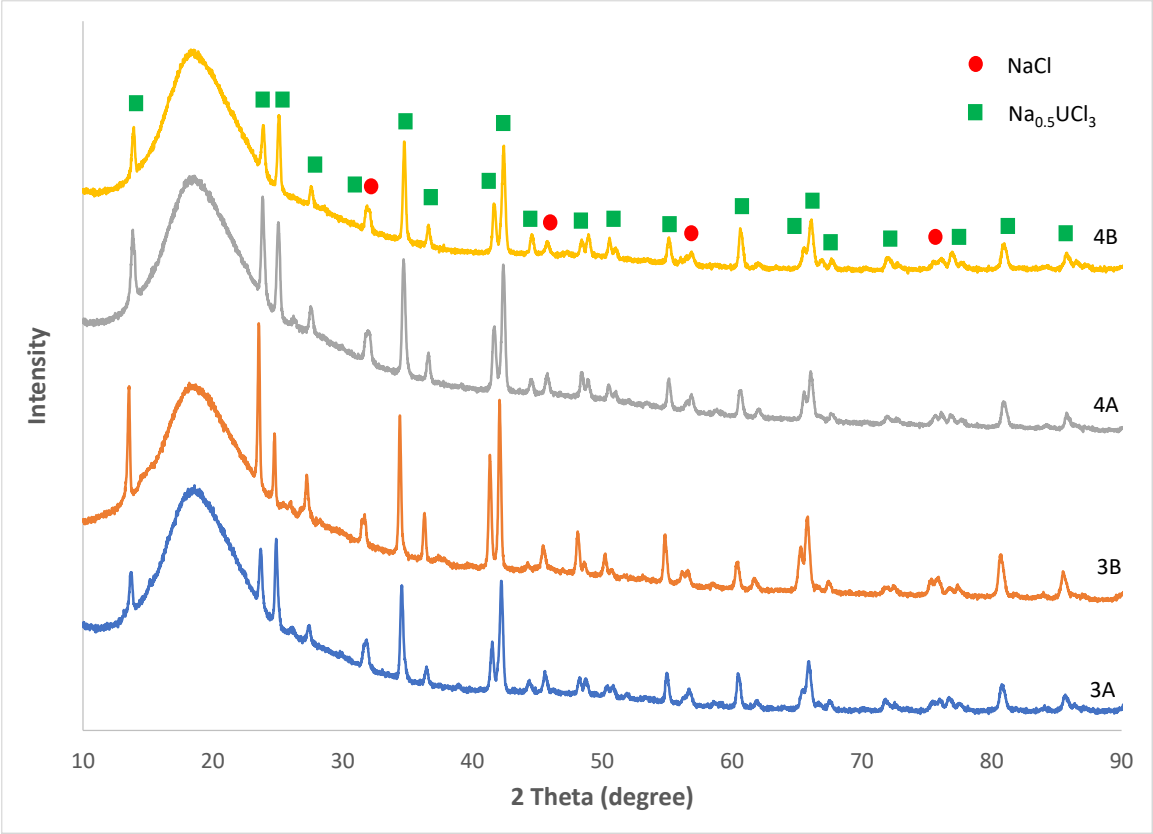

Figure 7.7. XRD patterns of sample material from runs 3 and 4.

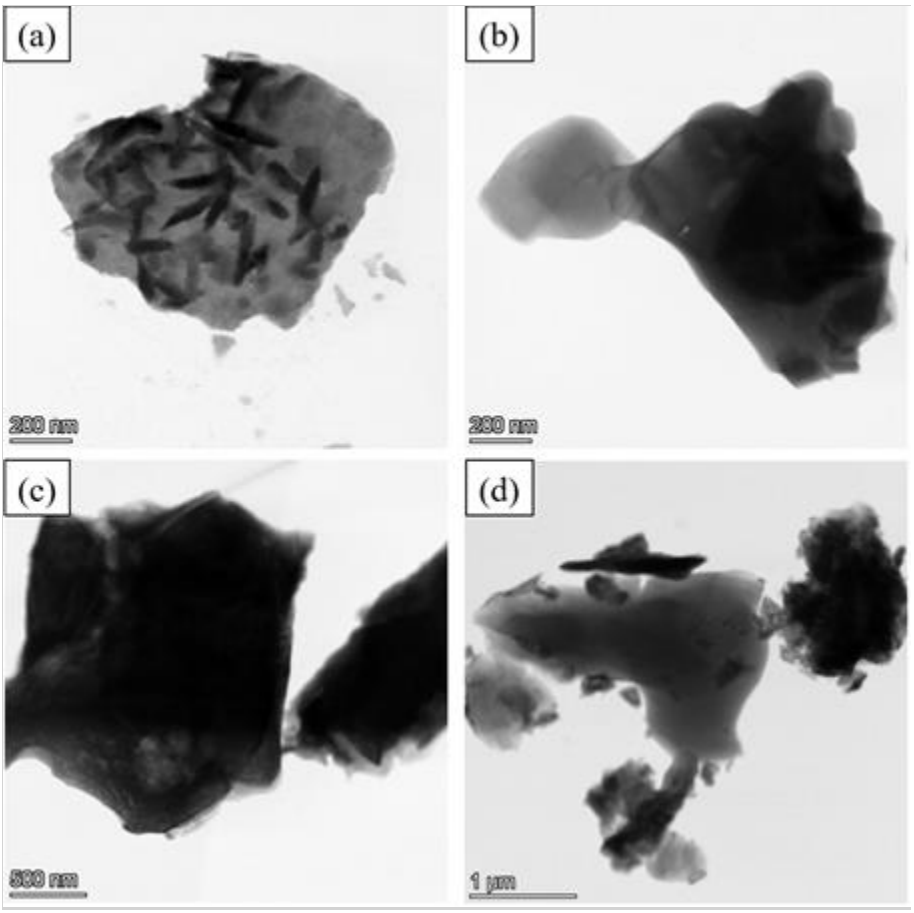

Figure 7.8. STEM images of samples (a) 1A, (b) 2A, (c) 3A, and (d) 4A.

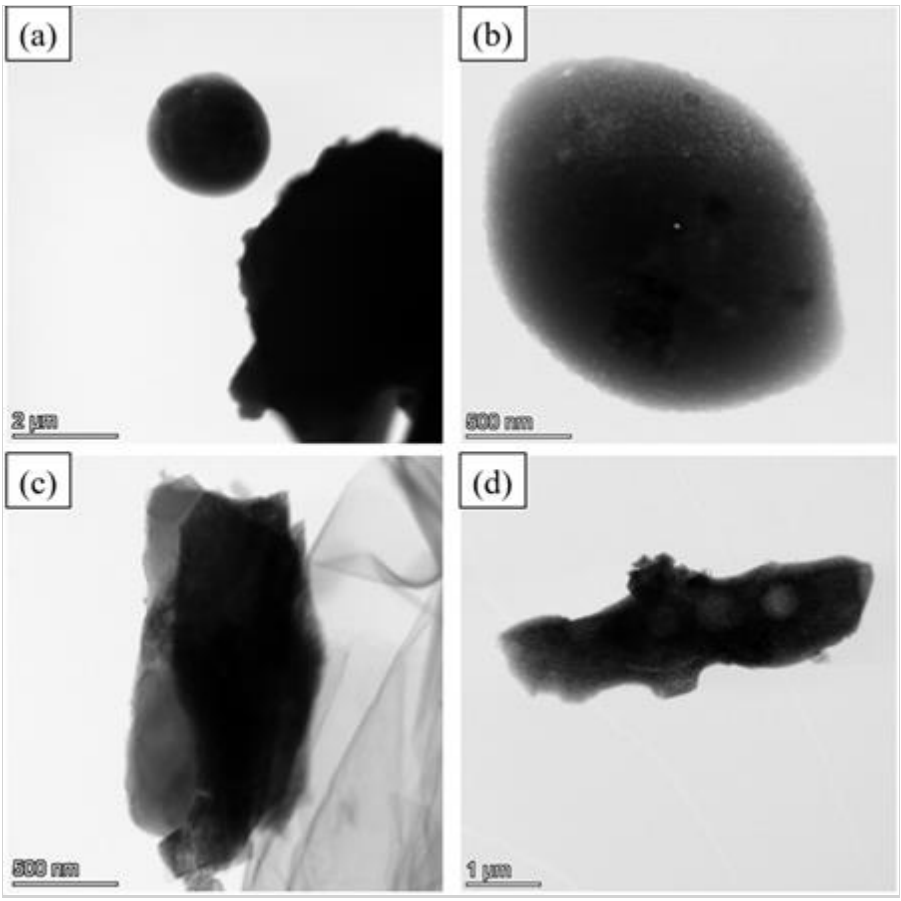

Figure 7.9. STEM images of samples (a) 1B, (b) 2B, (c) 3B, and (d) 4B.

Table 7.4. EDS compositions of samples from runs 1 – 4.

Samples	U		Cl		K		Na	
	at%	wt%	at%	wt%	at%	wt%	at%	wt%
1A	41.6	82.6	51.3	15.1	7.1	2.3	-	-
1B	39.9	81.2	39.1	11.8	20.9	7.0	-	-
2A	44.0	83.7	40.2	11.4	15.7	4.9	-	-
2B	49.0	86.4	42.9	11.3	8.1	2.3	-	-
3A	29.2	74.8	57.1	21.8	-	-	13.7	3.4
3B	20.3	66.1	52.4	25.4	-	-	27.3	8.6
4A	26.4	73.4	47.5	19.6	-	-	26.1	7.0
4B	38.6	82.3	45.0	14.3	-	-	16.4	3.4

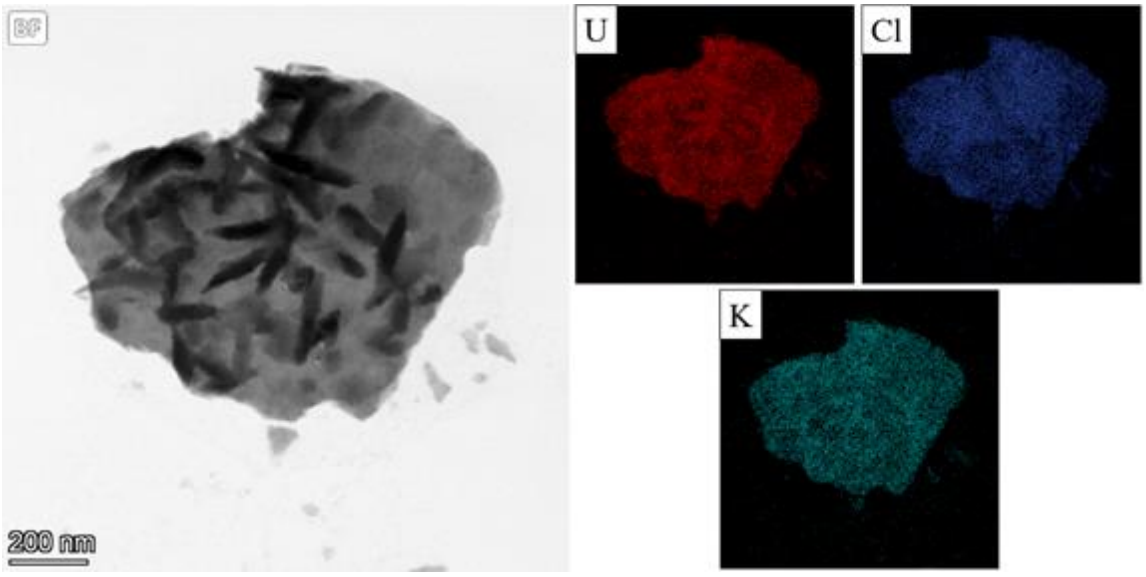

Figure 7.10. STEM-EDS map of sample 1A.

7.5 Discussion

The theoretical composition of reaction products per Eqs. 7.1 and 7.2 for the series of uranium trichloride synthesis runs were calculated based on the feed material input and the following assumptions. First, the prescribed blends of uranium feed material, ammonium chloride, and alkali-metal halide in the glass jar did not all transfer to the glassy carbon crucible, as some residual powder adhered to the inner jar walls. It was assumed that the mixtures that were transferred to the glassy carbon crucible for each run contained the same proportions of materials that were initially loaded in the respective glass jars. Second, all the nitrogen and hydrogen from ammonium chloride and uranium hydride, as applicable, separated from the reaction product as an off gas. Third, all the chloride from ammonium chloride was retained in the reaction to form uranium trichloride in the molten phase. Fourth, excess uranium metal, including the net mass gain or loss from the uranium metal electrode, was ascribed to an insoluble metal phase. Finally, the alkali-metal chlorides were present entirely in the molten phase without any reaction or material loss. Accordingly, the calculated elemental compositions of reaction product phases from the series of synthesis runs are shown in Table 7.5.

Table 7.5. Calculated elemental composition of reaction product phases from runs 1 – 4.

grams	**Run 1**	**Run 2**	**Run 3**	**Run 4**
Molten phase				
U	94.947	94.944	94.945	94.971
K	14.549	14.548	--	--
Li	3.569	3.569	--	--
Na	--	--	19.487	19.493
Cl	73.846	73.843	72.476	72.496
Total molten phase	186.911	186.904	186.908	186.960
Insoluble phase				
U	7.515	4.963	7.248	7.924
Total salt product	194.426	191.867	194.156	194.884
Gas phase				
N	16.761	16.761	16.761	16.765
H	4.825	5.824	4.825	5.926
Total off gas	21.586	22.585	21.586	22.691

The performance of the series of synthesis runs can be assessed by comparing the calculated and measured composition values. Specifically, the combination of the measured salt sample and salt ingot masses for each run from Table 7.2 can be compared to the

corresponding calculated total salt product mass from Table 7.5 to assess an overall material balance, as shown in Table 7.6.

Table 7.6. Comparison of overall material balance for series of synthesis runs.

	Run 1	Run 2	Run 3	Run 4
Measured salt product	195.209 g	192.315 g	193.317 g	194.827 g
Calculate salt product	194.426 g	191.867 g	194.156 g	194.884 g
Measured : calculated salt product	100.4%	100.2%	99.6%	100.0%

The overall material balances exhibited excellent consistencies between the measured and calculated values for each of the synthesis runs, which support the assumptions that essentially all the nitrogen and hydrogen from the ammonium chloride and uranium hydride, as applicable, separated from the salt product while all the chlorine remained behind. This observation was also substantiated by the presence of ammonia gas in the glovebox during the latter two runs and the absence of hydrogen chloride gas detection in the last run.

The calculated elemental concentrations can also be determined and compared to measured values to further assess performance of the series of runs. Specifically, the calculated uranium, potassium, lithium, and sodium concentrations in the molten phase (see Table 7.5) are compared to the measured values (see Table 7.3), including ratios of uranium to other metal cations, as shown in Table 7.7.

Table 7.7. Comparison of calculated and measured constituent concentrations from series of runs.

wt%	Run 1			Run 2			Run 3			Run 4		
sample	Calc.	1A	1B	Calc.	2A	2B	Calc.	3A	3B	Calc.	4A	4B
[U]	50.8	51.3	50.8	50.8	50.6	48.4	50.8	44.1	45.8	50.8	45.1	44.7
[K]	7.78	7.87	7.45	7.78	8.30	7.90	--	--	--	--	--	--
[Li]	1.91	2.00	1.89	1.91	2.11	1.96	--	--	--	--	--	--
[Na]	--	--	--	--	--	--	10.43	9.75	9.59	10.43	9.25	9.22
[U]:[K]	6.53	6.52	6.82	6.53	6.10	6.13	--	--	--	--	--	--
[U]:[Li]	26.6	25.7	26.9	26.6	24.0	24.7	--	--	--	--	--	--
[U]:[Na]	--	--	--	--	--	--	4.87	4.52	4.76	4.87	4.88	4.85

The calculated and measured concentrations of uranium, potassium, and lithium in runs 1 and 2 are relatively consistent, excepting slightly higher measured potassium and lithium values for run 2. The ratios of constituent concentrations provided a check on possible analytical error, in the case that all constituents for a particular sample were consistently high or low. While the calculated and measured ratios for run 1 are relatively consistent, those for run 2 are generally low. Thus, it appears that conversion of uranium hydride to uranium trichloride in run 2 was lower than that in run 1. Given a favorable overall material balance (including chlorine inventory) for run 2 along with a lower apparent trichloride concentration might suggest that some uranium tetrachloride formed and did not convert to uranium trichloride per Eq. 2.53.

The measured uranium and sodium concentrations in runs 3 and 4 are consistently lower than calculated values. However, the measured uranium to sodium concentration ratio is nearly identically to the calculated value for run 4, while that for run 3 is slightly lower. Thus, it appears that uranium hydride facilitated a higher conversion to uranium trichloride in run 4 than that of uranium metal in run 3. Again, the favorable material balances and lower apparent trichloride concentration in run 3 could suggest the presence of a minor fraction of uranium tetrachloride.

The initial heat-up rate for the series of synthesis runs was intentionally set at a low rate of 10°C/hr to meter the gasification and consequent delivery of hydrogen chloride reactant into the reactive, high-surface area uranium feed materials. The low heat-up rate also served to promote residence time for gaseous hydrogen chloride to react with the uranium feed materials. The parity between calculated and measured material balances for the series of synthesis runs suggests that no appreciable unreacted hydrogen chloride escaped from the glassy carbon crucible, which is further substantiated by the absence of steel wool or ring degradation and the lack of hydrogen chloride detection in gaseous diffusion tubes. On the other hand, gaseous ammonia was routinely observed during the runs in which the respective gaseous diffusion tubes were installed, suggesting that uranium trichloride synthesis occurred at least in part by the reaction mechanisms identified in Eqs. 7.1 and 7.2.

The intent of applying an electrolytic cell to the synthesized molten salt was to remove excess uranium metal from the product. The applied cell voltage provided ample overpotential to oxidize uranium metal in contact with the glassy carbon crucible without oxidizing uranium (III) ions to uranium (IV) ions. [145] However, in runs 1, 3, and 4, uranium metal was added to the system instead of removed. Although the electrolytic cell

failed to remove excess uranium in most of the synthesis runs, it did promote expected or higher than expected ratios of uranium to alkali-metal concentrations in the salt for runs 1 and 4. If separation of excess uranium metal from the synthesized salt were necessary, then distillation of the salt could be performed, which was beyond the scope of this study.

The XRD patterns for runs 1 and 2 (see Figure 7.6) exhibited a significant number of peaks of varying intensities, reflecting the number of possible species in the salt samples. The reactions of ammonium chloride with excess uranium metal and hydride per Eqs. 7.1 and 7.2 were expected to produce uranium trichloride. However, the formation of uranium tetrachloride is possible in the absence of localized excess uranium metal or hydride. The combination of lithium and potassium chloride with uranium trichloride and tetrachloride could lead to several mixed chloride formations, including K_2UCl_5 and Li_2UCl_6, as identified in their respective phase diagrams. [146-147] Indeed, the XRD patterns for runs 1 and 2 did exhibit each of the aforementioned simple and mixed chlorides. However, the prevalence of uranium (IV) chlorides in these samples was not expected to be significant, as the uranium concentrations in the same samples (see Table 7.7) were consistent with relatively high concentrations of uranium trichloride.

The XRD patterns for runs 3 and 4 (see Figure 7.7) were remarkably consistent between each sample, and they contained fewer peaks than those in runs 1 and 2. The primary expected constituents in runs 3 and 4 were sodium chloride and uranium trichloride. The phase diagram for sodium chloride and uranium trichloride [143] does not identify a mixed chloride; however, researchers have identified a reduced metallic chloride of uranium in combination with sodium chloride with a uranium oxidation state of +2.5. [148] Indeed, the primary species identified in the XRD patterns of samples in runs 3 and 4 was a reduced

metallic chloride of uranium in combination with sodium chloride. Sodium chloride was the only other species identified in these patterns. No uranium tetrachloride or mixed sodium chloride and uranium tetrachloride (e.g., Na_2UCl_6) were identified in these patterns.

The STEM images in Figures 7.8 and 7.9 exhibit a variety of crystalline structures. Dark needle-like structures are observed in samples 1A and 4A, while dark spots are apparent in samples 1B, 2B, and 4B. Dark planar structures are observed in samples 2A, 3A, 3B. Generally, the images of samples before electrolytic conditioning (see Figure 7.8) appear to be more heterogeneous with sharper edges, while those after electrolytic conditioning (see Figure 7.9) appear to be more homogenous with smoother surfaces.

The STEM-EDS map of sample 1A in Figure 7.10 identifies a relative uranium concentration density that is consistent with the dark needle-like crystalline structures. Furthermore, the relative potassium concentration density is consistent with that of uranium, suggesting a possible mixed potassium and uranium chloride phase (e.g., K_2UCl_5) like that observed in the XRD patterns for this same sample (see Figure 7.6).

The composition of samples from runs 1 – 4 per EDS are relative to the selected species, as EDS lacks the ability to identify low atomic mass elements such as lithium. Thus, the EDS values are not directly comparable to element analysis via ICP-OES. Nevertheless, the EDS values trend with relative loaded values of uranium (17 at%), chlorine (67 at%), and potassium (16 at%) in runs 1 and 2 and uranium (12 at%), chlorine (62 at%), and sodium (26 at%) in runs 3 and 4.

7.6 Summary and Conclusions

A series of four experiments was successfully conducted, producing high-purity uranium trichloride from uranium metal or uranium hydride powder and ammonium chloride

in either a lithium chloride – potassium chloride eutectic or sodium chloride medium. Near stoichiometric blends of uranium and ammonium chloride particulate along with select alkali-metal chloride particulate were heated at a low initial heat-up rate of 10°C/hr. The low heat-up rate effectively metered hydrogen chloride to react with the high-surface area uranium metal or hydride. This approach provided sufficient residence time for chlorination of uranium and its consequent fusion with the respective alkali-metal chlorides without any notable loss of chlorine from the system, based on material balances and hydrogen chloride detection mechanisms during the series of runs. Nitrogen and hydrogen from the ammonium chloride and uranium hydride feed materials were liberated in the reaction, dissipating in gaseous diatomic and ammonia forms. The products from the series of runs were dark consolidated salt ingots with an apparent density of 3.4 g/cc.

Elemental analysis of molten samples from each salt product revealed uranium concentrations ranging from 44 – 51 wt% compared to an expected concentration of 50.8%, suggesting that a minor fraction of uranium tetrachloride may have been present in some of the synthesized products. Characterization of ternary salt product samples from runs 1 and 2 via XRD identified expected simple and mixed chlorides, including lithium chloride, potassium chloride, uranium trichloride, and mixed potassium-uranium (III) chloride, as well as uranium tetrachloride and mixed lithium-uranium (IV) chloride. Diffractometry of binary salt product samples from runs 3 and 4 only identified sodium chloride and a mixed sodium – reduced uranium chloride. No uranium (IV) chloride in simple or mixed form was identified in the binary salt product samples. Microscopic analyses of product samples identified needle-like and planar crystalline structures, and EDS mapping identified relative constituent compositions consistent with loaded values.

8. Conclusions

Molten salt systems are promising media for dissolution of nuclear research reactor fuel constituents. The first focus of this study was an experimental investigation of operating parameters and associated reaction mechanisms that promoted the dissolution of used nuclear oxide fuel constituents in LiCl-KCl-UCl_3. This investigation concluded that the rate and extent of used oxide fuel constituent dissolution in the specified salt system were enhanced by (1) imposing reducing conditions in the oxide fuel matrix, (2) preconditioning the oxide fuel, (3) increasing the salt system temperature from 500 to 800°C, and (4) increasing the uranium fraction in the salt phase from 6 to 19 wt%. These parameters resulted in extents of alkali, alkaline earth, lanthanide, and transuranium constituent dissolution above 90%. Dissolution mechanisms involving the formation of uranium (III) oxychloride were proposed, which mechanisms likely contributed to the observed blending of uranium isotopes within the system. Further refinement of this oxide fuel dissolution technique could facilitate an approach to detoxify used nuclear oxide fuel such that the uranium oxide (which makes up ~94% of the metal mass in used nuclear oxide fuel) and accompanying noble metal fission products (which are primarily soft beta emitters) could be more readily disposed, while the reactive fission and transuranium constituents could be incorporated into highly leach-resistant, robust waste forms.

In the second focus of this study, a halogenation technique (including chlorination and bromination) was demonstrated to separate forms of aluminum metal from neodymium metal (as a surrogate for uranium metal) in molten halide (including chloride and bromide) salt systems. Ammonium halides (including chlorides and bromides) were used as the halogenating agents. This demonstration concluded that aluminum metal in both powder and

sheet form can be effectively separated as a gaseous aluminum halide from neodymium metal, which simultaneously formed neodymium halide and fused with its corresponding lithium halide. The separated aluminum, as condensed aluminum halide particulate, was subsequently processed into a consolidated waste form. This demonstration identified a viable pyrochemical approach to treating used aluminum matrix research reactor fuels, including used ATR fuel, via dissolution in molten salt systems. This approach could facilitate conversion of HEU from used ATR fuel to LEU, removing a proliferation concern, and incorporate the fuel's fission and transuranium constituents into highly leach-resistant, robust waste forms.

In the third focus of this study, deactivation methods for bond sodium by using ammonium and ferrous chlorides were investigated. The metered addition of ammonium chloride into molten sodium deactivated the pyrophoric and reactive metal into a stable sodium chloride without reaction excursion. However, deactivation of sodium metal with ferrous chloride produced a less pure product and exhibited occasional reaction excursion, resulting in a less attractive approach than reaction with ammonium chloride. This investigation identified a non-aqueous approach to deactivation of sodium metal that could be deployed in a dry remote operating environment. Indeed, this technique could be readily incorporated into exiting systems at INL to facilitate the safe and effective deactivation of bond sodium from LMR fuels.

In the fourth focus of this study, high-purity uranium trichloride was successfully synthesized using uranium metal and uranium hydride powders blended with ammonium chloride and alkali metal chlorides, including lithium chloride – potassium chloride eutectic and sodium chloride. The products were characterized to show the predominant presence of

uranium trichloride over uranium tetrachloride. This investigation identified a straightforward method to produce uranium trichloride in media suited for dissolution studies in molten salt systems. Application of this method is currently being investigated for synthesis of uranium trichloride in existing uranium electrorefining systems at INL.

Collectively, the research in this four-fold study has demonstrated the safe and effective dissolution of nuclear research reactor fuel constituents in select molten salt systems. Each of the four individual studies identified a path forward to address a specific need for treating and dispositioning legacy materials at INL.

This page intentionally left blank

Dissemination

1. S. D. Herrmann, P. K. Tripathy, S. M. Frank, and J. A. King, "Comparative Study of Monolithic Platinum and Iridium as Oxygen-Evolving Anodes during the Electrolytic Reduction of Uranium Oxide in a Molten LiCl-Li_2O Electrolyte," *Journal of Applied Electrochemistry*, **49**, 379 (2019)

   (Presented at University of Idaho for Qualification Exam in 2019)

2. Steven Herrmann and Kevin Norbash, "Method of Separating and Recovering Uranium from Aluminum-Clad Metallic Nuclear Fuel," U.S. Patent No. 10,418,138 (2019).

3. S. D. Herrmann, G. L. Fredrickson, S. M. Frank, "Recovery of Lanthanide Metal Fission Products from a Molten Chloride Salt System at Bench-Scale," proceedings of 43rd Annual Actinide Separations Conference, Kingsport, TN (2019).

4. S. D. Herrmann, D. L. Wahlquist, J. C. Price, M. N. Patterson, "Removal of Bond Sodium from an Irradiated Full-Length Experimental Breeder Reactor – II Blanket Element via Melt-Drain-Evaporate Process," proceedings of Global 2019, Seattle, WA (2019).

5. Guy L. Fredrickson, Guoping Cao, Prabhat K. Tripathy, Michael R. Shaltry, Steven D. Herrmann, Tae-Sic Yoo, Toni Y. Karlsson, David C. Horvath, Ruchi Gakhar, Ammon N. Williams, Robert O. Hoover, William C. Phillips, and Ken C. Marsden, "Review – Electrochemical Measurements in Molten Salt Systems: A Guide and Perspective," *Journal of The Electrochemical Society*, **166** (13) D645 (2019).

6. G. Cao, S. Herrmann, S. Li, R. Hoover, J. King, B. Serrano-Rodriguez, K. Marsden, "Development of a Li_2O Sensor Based on a Yttria Stabilized Zirconia (YSZ) Membrane for Oxide Reduction in a Molten LiCl-Li_2O Electrolyte at 650 °C," *Nuclear Technology*, **206**, 577 (2020).

7. Brian Westphal, David Tolman, Kevin Tolman, Steven Frank, Steve Herrmann, Stephen Warmann, Kenneth Marsden, and Michael Patterson, "Options Study for the

Neutralization of Elemental Sodium During the Pyroprocessing of Used Nuclear Fuel," *Journal of Nuclear Fuel Cycle and Waste Technology*, **18** (2), 113 (2020).

8. Tae-Sic Yoo, Steven D. Herrmann, Su-Jong Yoon, Ken C. Marsden, "Analysis and Modeling of Oxide Reduction Processes for Uranium Oxides," *Journal of Nuclear Materials*, **545** (2021) 152625

9. Steven D. Herrmann, Haiyan Zhao, Meng Shi, and Michael N. Patterson, "Controlled Conversion of Sodium Metal from Nuclear Systems to Sodium Chloride," accepted for publication in *Journal of Nuclear Fuel Cycle and Waste Technology* (2021 est.)

   (Included in dissertation)

10. Steven D. Herrmann, Haiyan Zhao, Meng Shi, Matthew M. Jones, and Michael N. Patterson, "Halogenation of Used Aluminum Matrix Test Reactor Fuel – A Bench-Scale Demonstration with Surrogate Materials," under review with *Journal of Nuclear Science and Technology* (2021 est.)

    (Included in dissertation)

11. Steven D. Herrmann, Brian R. Westphal, Shelly X. Li, and Haiyan Zhao, "Parametric Study of Used Nuclear Oxide Fuel Constituent Dissolution in Molten LiCl-KCl-UCl_3," under review with *Nuclear Technology* (2021 est.)

    (Included in dissertation)

12. Steven D. Herrmann, Haiyan Zhao, Kaustubh K. Bawane, Lingfeng He, Kevin Tolman, and Xiaofei Pu, "Synthesis and Characterization of High-Purity Uranium Trichloride in Alkali-Metal Chloride Media," awaiting submittal to *Journal of Nuclear Materials* (2021 est.)

    (Included in dissertation)

13. Prabhat K. Tripathy, Guy L. Fredrickson, Steven D. Herrmann, and Michael F. Simpson, "Electrochemical Materials and Energy Process," *Treatise on Process Metallurgy*, 2nd Ed., Elsevier, projected publication in 2023.

    (Invited in 2021 as co-author for a book chapter)

References

[1] https://www.world-nuclear.org/information-library/current-and-future-generation/nuclear-power-in-the-world-today.aspx

[2] https://www.eia.gov/tools/faqs/faq.php?id=207&t=3

[3] https://www.eia.gov/energyexplained/nuclear/us-nuclear-industry.php

[4] https://www.id.energy.gov/insideNEID/BriefHIstory.htm#:~:text=Site%20History,management%20of%20spent%20nuclear%20fuel.

[5] Lamarsh, J. R., *Introduction to Nuclear Engineering, 2nd Ed.,* Addison-Wesley Publishing Company, Massachusetts (1983).

[6] https://en.wikipedia.org/wiki/Nuclear_fuel

[7] Till, C. E. and Chang, Y. I., *Plentiful Energy*, ISBN: 978-1466384606, (2011).

[8] *Controlled Nuclear Chain Reaction*, American Nuclear Society, La Grange Park, Illinois (1992).

[9] https://www.energy.gov/sites/prod/files/AEC%20History.pdf

[10] Stevenson, C. E., *The EBR-II Fuel Cycle Story*, American Nuclear Society, La Grange Park, Illinois (1987).

[11] Westphal, C., "Vision and reality: The EBR-II story," *Nuclear News*, p25, February 2004.

[12] U.S. Department of Energy, "Record of Decision for the Treatment and Management of Sodium-Bonded Spent Nuclear Fuel," *Federal Register*, Vol. 65, No. 182, (2000).

[13] http://ansnuclearcafe.org/2014/10/10/they-harnessed-the-atom-the-first-navy-prototype-nuclear-plant/#sthash.es7Wj5os.dpbs

[14] https://www.eia.gov/energyexplained/nuclear/nuclear-power-plants-types-of-reactors.php

[15] https://www.energy.gov/ne/articles/5-fast-facts-about-spent-nuclear-fuel#:~:text=The%20United%20States%20does%20not,nuclear%20fuel%20in%20the%20future.

[16] https://www.epa.gov/laws-regulations/summary-nuclear-waste-policy-act#:~:text=(1982),or%20disposal%20of%20radioactive%20waste.&text=It%20directs%20EPA%20to%20develop,of%20radioactive%20material%20in%20repositories.

[17] Davis, W., "The MTR – Gone now, but not forgotten," ANS Nuclear Café, posted on October 25, 2012, http://ansnuclearcafe.org/2012/10/25/mtr-gone-now-but-not-forgotten/#sthash.P2ydb9NN.dpbs

[18] U.S. Department of Energy "Engineering Test Reactor Vessel Relocated," posted on October 2, 2007, https://www.id.energy.gov/news/PressReleases/PR071002.htm

[19] U.S. Department of Energy, Office of Nuclear Energy, "7 Fast Facts about Idaho National Laboratory's Advanced Test Reactor," posted on March 12, 2018, https://www.energy.gov/ne/articles/7-fast-facts-about-idaho-national-laboratorys-advanced-test-reactor

[20] Szilagyi, A. "US DOE Idaho national laboratory reactor decommissioning," NEA/RWM/R(2012)8, https://inis.iaea.org/collection/NCLCollectionStore/_Public/45/073/45073555.pdf

[21] Gibson G.W., deBoisblanc D.R., "The Use of Uranium Aluminide Powders in Nuclear Reactor Fuel Elements." In: Hausner H.H. (eds) *Modern Developments in Powder Metallurgy*, Springer, Boston, MA (1966) https://doi.org/10.1007/978-1-4684-7712-2_2

[22] U.S. Department of Energy, "The Advanced Test Reactor at INL," https://www.id.energy.gov/News/PDF/06-GA50553-02b_Web.pdf

[23] O'Kelly, S. "Advanced Test Reactor (ATR) and Materials Testing," INL/CON-17-41579, Idaho National Laboratory (2017) https://www.aps.org/policy/issues/energy/upload/AdvancedTestReactorMaterialsTesting.pdf

[24] Baum, E., Ernesti, M. C., Know, H. D., Miller, T. R., Watson, A. M., *Nuclides and Isotopes Chart of the Nuclides*, 17th Ed., Bechtel Marine Propulsion Corporation (2010).

[25] World Nuclear Organization, "Mixed Oxide (MOX) Fuel," (2017); https://www.world-nuclear.org/information-library/nuclear-fuel-cycle/fuel-recycling/mixed-oxide-fuel-mox.aspx

[26] Zohuri B., Fission Product Buildup and Decay. In: Neutronic Analysis for Nuclear Reactor Systems. Springer, Cham. (2019) https://doi.org/10.1007/978-3-030-04906-5_15

[27] Wagner, J., et al., "Characterization of Used Nuclear Fuel Inventory in Support of a Comprehensive National Nuclear Fuel Cycle Strategy," Oak Ridge National Laboratory, ORNL/TM-2012/308 FCRD-FCT-2012-000232 (2012); https://www.energy.gov/sites/prod/files/2013/08/f2/CategorizationUsedNuclearFuelInventory.pdf

[28] Lambert, J. D. B, Strains, R., "Oxide Fuels," *Materials Science and Technology*, Wiley-VCH Verlag GmbH & Co. (2006).

[29] Wigeland, R., et al., "Spent Nuclear Fuel Separations and Transmutation Criteria for Benefit to a Geologic Repository," Waste Management 2004 Conference, Tucson, USA (2004).

[30] Balzhiser, R. E., Samuels, M. R., Eliassen, J. D., *Chemical Engineering Thermodynamics: The Study of Energy, Entropy, and Equilibrium*, Prentice-Hall, Inc., Englewood Cliffs, New Jersey (1972).

[31] Fogler, H. S., *Elements of Chemical Reaction Engineering*, 4th Ed., Pearsons Education, Inc. (2006).

[32] Fuller, T. F., Harb, J. N., Electrochemical Engineering, John Wiley & Sons, Inc. (2018).

[33] Outotec, HSC Chemistry 8, Pori (2015).

[34] Vivadifferences, “How is an Electrolytic Cell Different from an Electrochemical (Galvanic) Cell; https://vivadifferences.com/difference-between-electrolytic-cell-and-galvanic-cell/

[35] U. S. Department of Energy, “Disposition of Surplus Highly Enriched Uranium Final Environmental Impact Statement,” DOE/EIS-0240 (1996).

[36] U. S. Department of Energy, “Final Environmental Impact Statement for the Treatment and Management of Sodium-Bonded Spent Nuclear Fuel,” DOE/EIS-0306 (2000).

[37] National Research Council, “Electrometallurgical Techniques for DOE Spent Fuel Treatment: Final Report (2000),” National Academy Press, Washington D.C., ISBN 978-0-309-07095-9, (2000).

[38] G. K. Johnson, R. D. Pierce, D. S. Poa, and C. C. McPheeters, “Pyrochemical Recovery of Actinide Elements from Spent Light Water Reactor Fuel,” *Actinide Processing: Methods and Materials*, B. Mishra and W. A. Avrill, Eds., TMS Publications, Warrendale, PA (1994).

[39] E. J. Karell, R. D. Pierce, and T. P. Mulcahey, “Treatment of Oxide Spent Fuel Using the Lithium Reduction Process,” *proceedings of ANS Topical Meeting*, Reno, NV (1996).

[40] K. V. Gourishankar and E. J. Karell, “Application of Lithium in Molten-Salt Reduction Processes,” *Light Metals 1999*, C. Edward Eckert, Ed., TMS Society, Warrendale, PA (1999).

[41] E. J. Karell, K. V. Gourishankar, J. L. Smith, L. S. Chow, L. Redey, “Separation of Actinides from LWR Spent Fuel Using Molten-Salt-Based Electrochemical Processes,” *Nuclear Technology*, **136** (2001).

[42] Y. Kado, T. Goto, and R. Hagiwara, “Dissolution Behavior of Lithium Oxide in Molten LiCl-KCl Systems,” *J. Chem Eng. Data*, **53** (2008).

[43] K. Gourishankar, L. Redey, and M. Williamson, "Electrolytic Reduction of Metal Oxides in Molten Salts," *Light Metals 2002*, W. Schneider, Ed., TMS Society, Warrendale, PA (2002).

[44] S. D. Herrmann, S. X. Li, and M. F. Simpson, "Electrolytic Reduction of Spent Oxide Fuel – Bench-Scale Test Results," proceedings of Global 2005, Tsukuba, Japan (2005).

[45] S. D. Herrmann, S. X. Li, M. F. Simpson, and S. Phongikaroon, "Electrolytic Reduction of Spent Nuclear Oxide Fuel as Part of an Integral Process to Separate and Recover Actinides from Fission Products," *Separation Science and Technology*, **41**, 1965 (2006).

[46] S. Herrmann, S. Li, and M. Simpson, "Electrolytic Reduction of Spent Light Water Reactor fuel – Bench-Scale Experiment Results," Journal of Nuclear Science and Technology, **44** (3) 361 (2007).

[47] S. D. Herrmann, S. X. Li, D. A. Sell, and B. R. Westphal, "Electrolytic Reduction of Spent Nuclear Oxide Fuel – Effects of Fuel Form and Cathode Containment Materials on Bench-Scale Operations," proceedings of Global 2007, Boise, Idaho (2007).

[48] L. A. Barnes and J. L. Willit, "Direct Electrolytic Reduction of UO_2 vs. U_3O_8," proceedings of Global 2007, Boise, Idaho (2007).

[49] S. D. Herrmann, S. X. Li, and B. E. Serrano-Rodriguez, "Observations of Oxygen Ion Behavior in the Lithium-Based Electrolytic Reduction of Uranium Oxide," proceedings of Global 2009, Paris, France (2009).

[50] S. D. Herrmann and S. X. Li, "Separation and Recovery of Uranium Metal from Spent Light Water Reactor Fuel via Electrolytic Reduction and Electrorefining," *Nuclear Technology*, **171**, 247 (2010).

[51] S. D. Herrmann, S. X. Li, and B. R. Westphal, "Separation and Recovery of Uranium and Group Actinide Products from Irradiated Fast Reactor MOX Fuel via Electrolytic Reduction and Electrorefining," *Separation Science and Technology*, **47**, 2044 (2012).

[52] A. Merwin, P. Motsegood, J. Willit, and M. A. Williamson, "A Parametric Study of Operating Carbon Anodes in the Oxide Reduction Process," *Journal of Nuclear Materials*, **511**, 297 (2018).

[53] S. D. Herrmann, P. K. Tripathy, S. M. Frank, and J. A. King, "Comparative Study of Monolithic Platinum and Iridium as Oxygen-Evolving Anodes during the Electrolytic Reduction of Uranium Oxide in a Molten LiCl-Li_2O Electrolyte," *Journal of Applied Electrochemistry*, **49**, 379 (2019).

[54] A. Burak, J. Chamberlain, and M. F. Simpson, "Study of Entrainment of Li_2O in Product from Direct Electrolytic Reduction of UO_2 in Molten LiCl-Li_2O. Part 1: Post-Processing and Analysis Techniques," *Journal of Nuclear Materials*, **529**, 1 (2020).

[55] M. Kurata, T. Inoue, J. Serp, M. Ougier, and J. P. Glatz, "Electro-Chemical Reduction of MOX in LiCl," *Journal of Nuclear Materials*, **328**, 97 (2004).

[56] M. Iizuka, Y. Sakamura, and T. Inoue, "Electrochemical Reduction of (U-40Pu-5Np)O_2 in Molten LiCl Electrolyte," *Journal of Nuclear Materials*, **359**, 102 (2006).

[57] Y. Sakamura, M. Kurata, and T. Inoue, "Electrochemical Reduction of UO_2 in Molten $CaCl_2$ or LiCl," *Journal of The Electrochemical Society*, **153** (3) D31 (2006).

[58] M. Iizuka, T. Inoue, M. Ougier, and J. P. Glatz, "Electrochemical Reduction of (U,Pu)O_2 in Molten LiCl and $CaCl_2$ Electrolytes," *Journal of Nuclear Science and Technology*, **44** (5) 801 (2007).

[59] Y. Sakamura, T. Omori, and T. Inoue, "Application of Electrochemical Reduction to Produce Metal Fuel Material from Actinide Oxides," *Nuclear Technology*, **162**, 169 (2008).

[60] M. Kurata and N. Yahagi, "Electrochemical Reduction of MOX Pellets in Molten Lithium Chloride Based on a Practical Operating Condition," *Nuclear Technology*, **164**, 433 (2008).

[61] Y. Sakamura and T. Omori, "Electrolytic Reduction and Electrorefining of Uranium to Develop Pyrochemical Reprocessing of Oxide Fuels," *Nuclear Technology*, **171**, 266 (2010).

[62] Y. Sakamura, "Effect of Alkali and Alkaline-Earth Chloride Addition on Electrolytic Reduction of UO_2 in LiCl Salt Bath," *Journal of Nuclear Materials*, **412**, 177 (2011).

[63] Y. Sakamura and M. Akagi, "Pyrochemical Reprocessing Tests to Collect Uranium Metal from Simulated Spent Oxide Fuel," *Nuclear Technology,* **179**, 220 (2012).

[64] J. M. Hur, C. S. Seo, S. S. Hong, D. S. Kang, and S. W. Park, "Metallization of U_3O_8 via Catalytic Electrochemical Reduction with Li_2O in LiCl Molten Salt," *Reaction Kinetics and Catalysis Letters,* **80** (2) 217 (2003).

[65] C. S. Seo, S. B. Park, B. H. Park K. J. Jung, S. W. Park, and S. H. Kim, "Electrochemical Study on the Reduction Mechanism of Uranium Oxide in a LiCl-Li_2O Molten Salt," *Journal of Nuclear Science and Technology,* **43** (5) 587 (2006).

[66] S. M. Jeong, S. B. Park, S. S. Hong, C. S. Seo, and S. W. Park, "Electrolytic Production of Metallic Uranium from U_3O_8 in a 20-kg Batch Scale Reactor," *Journal of Radioanalytical and Nuclear Chemistry*, **268** (2) 349 (2006).

[67] S. B. Park, B. H. Park, S. M. Jeong, J. M. Hur, C. S. Seo, S. H. Choi, and S. W. Park, "Characteristics of an Integrated Cathode Assembly for the Electrolytic Reduction of Uranium Oxide in a LiCl-Li_2O Molten Salt," *Journal of Radioanalytical and Nuclear Chemistry*, **268** (3) 489 (2006).

[68] S. M. Jeong, J. M. Hur, S. S. Hong, D. S. Kang, M. S. Choung, C. S. Seo, J. S. Yoon, and S. W. Park, "An Electrochemical Reduction of Uranium Oxide in the Advanced Spent-Fuel Conditioning Process," *Nuclear Technology*, **162**, 184 (2008).

[69] B. H. Park, I. W. Lee, and C. S. Seo, "Electrolytic Reduction Behavior of U_3O_8 in a Molten LiCl-Li_2O Salt," *Chemical Engineering Science*, **63**, 3485 (2008).

[70] J. M. Hur, I. K. Choi, S. H. Cho, S. M. Jeong, and C. S. Seo, "Preparation and Melting of Uranium from U_3O_8," *Journal of Alloys and Compounds*, **452**, 23 (2008).

[71] S. M. Jeong, H. S. Shin, S. H. Cho, J. M. Hur, and H. S. Lee, "Electrochemical Behavior of a Platinum Anode for Reduction of Uranium Oxide in a LiCl Molten Salt," *Electrochimica Acta,* **54**, 6335 (2009).

[72] S. M. Jeong, H. S. Shin, S. S. Hong, J. M. Hur, J. B. Do, and H. S. Lee, "Electrochemical Reduction Behavior of U_3O_8 Powder in a LiCl Molten Salt," *Electrochimica Acta*, **55**, 1749 (2010).

[73] J. M. Hur, S. M. Jeong, and H. Lee, "Underpotential Deposition of Li in a Molten LiCl-Li_2O Electrolyte for the Electrochemical Reduction of U from Uranium Oxides," *Electrochemistry Communications,* **12**, 706 (2010).

[74] S. M. Jeong, B. H. Park, J. M. Hur, C. S. Seo, H. S. Lee, and K. C. Song, "An Experimental Study on an Electrochemical Reduction of an Oxide Mixture in the Advanced Spent-Fuel Conditioning Process," *Nuclear Engineering and Technology*, **42** (2) 183 (2010).

[75] E. Y. Choi, J. M. Hur, I. K. Choi, S. G. Kwon, D. S. Kang, S. S. Hong, H. S. Shin, M. A. Yoo, and S. M. Jeong, "Electrochemical Reduction of Porous 17 kg Uranium Oxide Pellets by Selection of an Optimal Cathode/Anode Surface Area Ratio," *Journal of Nuclear Materials*, **418**, 87 (2011).

[76] E. Y. Choi, J. W. Lee, J. J. Park, J. M. Hur, J. K. Kim, K. Y. Jung, and S. M. Jeong, "Electrochemical Reduction Behavior of a Highly Porous SIMFUEL Particle in a LiCl Molten Salt," *Chemical Engineering Journal*, **207-208**, 514 (2012).

[77] J. M. Hur, S. S. Hong, and H. Lee, "Electrochemical Reduction of UO_2 to U in a LiCl-KCl-Li_2O Molten Salt," *Journal of Radioanalytical Nuclear Chemistry*, **295**, 851 (2013).

[78] W. Park, J. K. Kim, J. M. Hur, E. Y. Choi, H. S. Im, S. S. Hong, "Application of a Boron Doped Diamond (BDD) Electrode as an Anode for the Electrolytic Reduction of UO_2 in Li_2O-LiCl-KCl Molten Salt," *Journal of Nuclear Materials*, **432**, 175 (2013).

[79] E. Y. Choi, J. K. Kim, H. S. Im, I. K. Choi, S. H. Na, J. W. Lee, S. M. Jeong, and J. M. Hur, "Effect of the UO_2 Form on the Electrochemical Reduction Rate in a LiCl-Li_2O Molten Salt," *Journal of Nuclear Materials*, **437**, 178 (2013).

[80] W. Park, J. M. Hur, S. S. Hong, E. Y. Choi, H. S. Im, S. C. Oh, and J. W. Lee, "An Experimental Study for Li Recycling in an Electrolytic Reduction Process for UO_2 with a Li_2O-LiCl Molten Salt," *Journal of Nuclear Materials*, **441**, 232 (2013).

[81] E. Y. Choi, S. H. Im, and J. M. Hur, "Effect of the Anode-to-Cathode Distance on the Electrochemical Reduction in a LiCl-LI_2O Molten Salt," *Journal of the Korean Electrochemical Society*, **16** (3) 138 (2013).

[82] J. M. Hur, J. S. Cha, and E. Y. Choi, "Can Carbon be an Anode for Electrochemical Reduction in a LiCl-Li_2O Molten Salt?" *ECS Electrochemistry Letters*, **3** (10) E5 (2014).

[83] E. Y. Choi, C. Y. Won, J. S. Cha, W. Park, H. S. Im, S. S. Hong, and J. M. Hur, "Electrochemical Reduction of UO_2 in LiCl-Li_2O Molten Salt Using Porous and Nonporous Anode Shrouds," *Journal of Nuclear Materials*, **444**, 261 (2014).

[84] S. W. Kim, W. Park, H. S. Im, J. M. Hur, S. S. Hong, S. C. Oh, and E. Y. Choi, "Electrochemical Behavior of Liquid Sb Anode System for Electrolytic Reduction of UO_2," *Journal of Radioanalytical Nuclear Chemistry*, **303**, 1041 (2015).

[85] E. Y. Choi, C. Y. Won, D. S. Kang, S. W. Kim, J. S. Cha, S. J. Lee, W. Park, H. S. Im, and J. M. Hur, "Production of Uranium Metal via Electrolytic Reduction of Uranium Oxide in Molten LiCl and Salt Distillation," *Journal of Radioanalytical Nuclear Chemistry*, **304**, 535 (2015).

[86] S. W. Kim, E. Y. Choi, W. Park, H. S. Im, and J. M. Hur, "A Conductive Oxide as an O_2 Evolution Anode for the Electrolytic Reduction of Metal Oxides," *Electrochemistry Communications*, **55**, 14 (2015).

[87] E. Y. Choi C. Y. Won, S. J. Lee, D. S. Kang, S. W. Kim, J. S. Cha, W. Park, H. S. Im, and J. M. Hur, "Use of a Single Fuel Containment Material during Pyroprocessing Tests," *Annals of Nuclear Energy*, **76**, 305 (2015).

[88] W. Park, E. Y. Choi, S. W. Kim, S. C. Jeon, Y. H. Cho, and J. M. Hur, "Electrolytic Reduction of a Simulated Oxide Spent Fuel and the Fates of Representative Elements in a Li_2O-LiCl Molten Salt," *Journal of Nuclear Materials*, **477**, 59 (2016).

[89] M. W. Lee, E. Y. Choi, S. C. Jeon, J. Lee, S. B. Park, S. Paek, M. F. Simpson, and S. M. Jeong, "Enhanced Electrochemical Reduction of Rare Earth Oxides in Simulated Oxide Fuel via Co-Reduction of NiO in Li_2O-LiCl Salt," *Electrochemistry Communications*, **72**, 23 (2016).

[90] S. W. Kim, M. K. Jeon, H. W. Kang, S. K. Lee, E. Y. Choi, W. Park, S. S. Hong, S. C. Oh, and J. M. Hur, "Carbon Anode with Repeatable Use of LiCl Molten Salt for Electrolytic Reduction in Pyroprocessing," *Journal of Radioanalytical Nuclear Chemistry*, **310**, 463 (2016).

[91] E. Y. Choi, J. Lee, S. J. Lee, S. W. Kim, S. C. Jeon, S. H. Cho, S. C. Of, M. K. Jeon, S. K. Lee, H. W. Kang, and J. M. Hur, "Stability of Yttria-Stabilized Zirconia during Pyroprocessing Tests," *Journal of Nuclear Materials*, **475**, 57 (2016).

[92] S. W. Kim, D. H. Heo, S. K Lee, M. K. Jeon, W. Park, J. M. Hur, S. S. Hong, S. C. Oh, and E. Y. Choi, "A Preliminary Study of Pilot-Scale Electrolytic Reduction of UO_2 Using a Graphite Anode," *Nuclear Engineering and Technology*, **49**, 1451 (2017).

[93] S. W. Kim, S. K. Lee, H. W. Kang, E. Y. Choi, W. Park, S. S. Hong, S. C. Oh, and J. M. Hur, "Electrochemical Properties of Noble Metal Anodes for Electrolytic Reduction of Uranium Oxide," *Journal of Radioanalytical Nuclear Chemistry*, **311**, 809 (2017).

[94] E. Y. Choi, M. K. Jeon, J. Lee, S. W. Kim, S. K. Lee, S. J. Lee, D. H. Heo, H. W. Kang, S. C. Jeon, and J. M. Hur, "Reoxidation of Uranium Metal Immersed in a Li_2O-LiCl Molten Salt after Electrolytic Reduction of Uranium Oxide," *Journal of Nuclear Materials*, **485**, 90 (2017).

[95] E. Y. Choi, J. Lee, D. H. Heo, S. K. Lee, M. K. Jeon, S. S. Hong, S. W. Kim, H. W. Kang, S. C. Jeon, and J. M. Hur, "Electrolytic Reduction Runs of 0.6 kg Scale-Simulated Oxide Fuel in a Li_2O-LiCl Molten Salt Using Metal Anode Shrouds," *Journal of Nuclear Materials*, **489**, 1 (2017).

[96] E. Y. Choi, J. Lee, D. H. Heo, and J. M. Hur, "Quantitative Analysis of Oxygen Gas Exhausted from Anode through In Situ Measurement during Electrolytic Reduction," *Science and Technology of Nuclear Installations,* (2017).

[97] E. Y. Choi, M. K. Jeon, J. M. Hur, "Reoxidation of Uranium in Electrolytically Reduced Simulated Oxide Fuel during Residual Salt Distillation," *Journal of Radioanalytical Nuclear Chemistry,* **314**, 207 (2017).

[98] E. Y. Choi and J. Lee, "Complete Reduction of High-Density UO_2 to Metallic U in Molten Li_2O-LiCl," *Journal of Nuclear Materials,* **494**, 439 (2017).

[99] E. Y. Choi and J. Lee, "Feasibility Tests of Nickel as a Containment Material of Molten Li_2O-LiCl Salt Containing Li Metal at 650 °C during Electrolytic Reduction," *Journal of Nuclear Materials*, **495**, 85 (2017).

[100] E. Y. Choi, J. Lee, D. H. Heo, and J. M. Hur, "Separation of Electrolytic Reduction Product from Stainless Steel Wire Mesh Cathode Basket via Salt Draining and Reuse of the Cathode Basket," *Science and Technology of Nuclear Installations*, (2017).

[101] S. K. Lee, M. K. Jeon, S. W. Kim, E. Y. Choi, J. Lee, S. S. Hong, S. C. Oh, and J. M. Hur, "Evaluation of Pt Anode Stability in Repeated Electrochemical Oxide Reduction Reactions for Pyroprocessing," *Journal of Radioanalytical Nuclear Chemistry,* **316**, 1053 (2018).

[102] E. Y. Choi and H. W. Kang, "Quantitative Analysis of Barium and Strontium in Simulated Oxide Fuel during Electrolytic Reduction and Salt Distillation," *Journal of Radioanalytical Nuclear Chemistry,* **317**, 853 (2018).

[103] E. Y. Choi and J. Lee, "Highly Enhanced Reduction of Rare Earth Oxides in Simulated Oxide Fuel in Li_2O-LiCl Salt Using Lithium Metal," *Journal of Nuclear Materials*, **511**, 367 (2018).

[104] T. B. Joseph, N. Sanil, K. S. Mohandas, and K. Nagarajan, "A Study of Graphite as Anode in the Electro-Deoxidation of Solid UO_2 in LiCl-Li_2O Melt," *Journal of The Electrochemical Society,* **162** (6) E51 (2015).

[105] G. F. Brunzie, T. R. Johnson, and R. K. Steunenberg, "Selective Dissolution of Uranium from Uranium – Uranium Oxide Mixtures by Bromine – Ethyl Acetate," *Analytical Chemistry*, **33** (8) 1005 (1961).

[106] A. W. Ashbrook, "The Determination of Uranium Metal in Products from the Reduction of Uranium Oxides with Magnesium," *The Analyst*, **87**, 751 (1962).

[107] I. Glagolenko, D. Wachs, N. Woolstenhulme, G. Chang, B. Rabin, C. Clark, "Irradiation Testing of the RERTR Fuel Miniplates with Burnable Absorbers in the Advanced Test Reactor," proceedings of RERTR 2010, Lisbon (2010).

[108] G. Petersen, "Evaluation of Neutron Absorbers in the DOE Standardized SNF Canister, INL/EXT-19-53193, Idaho National Laboratory (2019).

[109] D. Stahl, "Fuels for Research and Test Reactors, Status Review: July 1982," ANL-83-5, Argonne National Laboratory (1982).

[110] International Atomic Energy Agency, "Research reactor core conversion guidebook, Volume 4: Fuels (Appendices I-K," IAEA-TECDOC-643 (1992).

[111] L. B. Lundberg and M. L. Croson, "Corrosion of Spent Advanced Test Reactor Fuel," EGG-M-9422, Idaho National Engineering and Environmental Laboratory (1994).

[112] U.S. Nuclear Waste Technical Review Board, "Management and Disposal of U.S. Department of Energy Spent Nuclear Fuel -- A Report to the United States Congress and the Secretary of Energy," Arlington (2017).

[113] ASM International, Diagram No. 900138 (2006).

[114] S. Herrmann, K. Norbash, D. Wachs, "Separation and Recovery of Uranium from Next Generation Research Reactor Fuel via Molten Salt Electrorefining," Fray International Symposium, Volume 3: Molten Salts and Ionic Liquids 2011, ISBN: 978-0-9879974-0-1 (2012).

[115] J. L. Willit, E. C. Gay, W. E. Miller, C. C. McPheeters, and J. J. Laidler, "Electrometallurgical Treatment of Aluminum-Matrix Fuels," proceedings of DOE Spent Nuclear Fuel and Fissile Material Management Embedded Topical Meeting, Reno (1996).

[116] C. C. McPheeters, E. C. Gay, E. J. Karell, and J. P. Ackerman, "Electrometallurgically Treating Metal, Oxide, and Al Alloy Spent Nuclear Fuel Types," *JOM,* 22, July 1997.

[117] J. L. Willit, S. A. Slater, A. Raraz, and E. C. Gay, "Electrometallurgical Treatment of Aluminum-based Fuels," proceedings of Third Topical Meeting on DOE Spent Nuclear Fuel and Fissile Materials Management," Charleston (1998).

[118] S. A. Slater, A. G. Raraz, J. L. Willit, E. C. Gay, "Electrochemical separation of aluminum from uranium for research reactor spent nuclear fuel applications," *Separations and Purification Technology*, **15**, 197 (1999).

[119] E. Mendes, L. Cassayre, R. Malmeck, P. Soucek, R. Jardin, J. P. Glatz, "Recovery of Actinides from Actinide-Aluminum Alloys: Chlorination Route," proceedings of ATALANTE 2008, Montpellier (2008).

[120] P. Soucek, R. Malmbeck, E. Mendes, C. Nourry, R. Jardin, J. P. Glatz, "Separation of Uranium from Uranium-Aluminum Alloys by Chlorination Process," proceedings of Global 2009, Paris (2009).

[121] P. Soucek, R. Malmbeck, C. Nourry, and J. P. Glatz, "Pyrochemical Reprocessing of Spent Fuel by Electrochemical Techniques Using Solid Aluminum Cathodes," *Energy Procedia,* **7**, 396 (2011).

[122] R. Meier, P. Soucek, R. Malmbeck, T. Fanghaenel, "Recycling of Uranium from Uranium-Aluminum alloys by Chlorination with HCl(g)," *Procedia Chemistry*, **7**, 785 (2012).

[123] A. Bohel, H. Nassini, A. Bevilacqua, and D. Pasquevich, "Chlorination Reactions Applied to Reprocessing of Aluminum-Uranium Spent Nuclear Fuels," *Materials Research Society Symposium Proceedings,* **506**, 535 (1997).

[124] S. D. Herrmann, J. A. Buzzell, M. J. Holzemer, "Treatment of EBR-I NaK Mixed Waste at Argonne National Laboratory and Subsequent Land Disposal at the Idaho National Engineering and Environmental Laboratory," proceedings of Waste Management '98 Conference, Tuscon, Arizona (1998).

[125] S. D. Herrmann, H. W. Buschman, R. A. Washburn, "Conversion of Elemental Sodium to Sodium Carbonate at Argonne National Laboratory," proceedings of ANS Annual Meeting, Philadelphia, Pennsylvania (1995).

[126] B. Westphal, D. Tolman, K. Tolman, S. Frank, S. Herrmann, S. Warmann, and M. Patterson, "Options Study for the Neutralization of Elemental Sodium during the Pyroprocessing of Used Nuclear Fuel," *Journal of Nuclear Fuel Cycle and Waste Technology*, **18** (2) 123 (2020).

[127] D. Bradley, "The Preparation and Properties of the Chlorides of Uranium, Plutonium, Thorium and of the Fission Product Chlorides," Atomic Energy Research Establishment, CE/R 2215, Berkshire, UK (1957).

[128] W. E. Miller and Z. Tomczuk, "Method for Making a Uranium Chloride Salt Product," U.S. Patent No. US 6,800,262 (2004).

[129] B. R. Westphal, J. C. Price, R. D. Marini, "Synthesis of Uranium Trichloride for the Pyrometallurgical Processing of Used Nuclear Fuel," Fray International Symposium, Volume 3: Molten Salts and Ionic Liquids 2011, ISBN: 978-0-9879974-0-1 (2012).

[130] H. Lambert, T. Kerry, C. A. Sharrad, "Preparation of Uranium (III) in a Molten Chloride Salt: A Redox Mechanistic Study," *Journal of Radioanalytical and Nuclear Chemistry*, **317**, 925 (2018).

[131] G. Y. Kim, T. J. Kim, J. Jang, H. C. Eun, S. J. Lee, "Synthesis of Uranium Trichloride Salt Using $ZnCl_2$," *Journal of Radioanalytical and Nuclear Chemistry*, **318**, 2173 (2018).

[132] H. C. Eun, T. J. Kim, J. H. Jang, G. Y. Kim, S. J. Lee, J. M. Hur, "A Study of Chlorination of Uranium Metal Using Ammonium Chloride," *Journal of Radioanalytical Nuclear Chemistry*, **314**, 533 (2017).

[133] A. L Hames, A. Paulenova, J. L. Willit, M. A. Williamson, "Phase Equilibria Studies of the LiCl-KCl-UCl_3 System," *Nuclear Technology*, **203**, 272 (2018).

[134] https://science.sckcen.be/en/Facilities/BR3

[135] B. R. Westphal, K. J. Bateman, C. D. Morgan, J. F. Berg, P. J. Crane, D. G. Cummings, J. J. Giglio, M. W. Huntley, R. P. Lind, and D. A. Sell, "Effect of Process Variables During the Head-End Treatment of Spent Oxide Fuel," *Nuclear Technology*, **162**, 153 (2008).

[136] W. B. White, S. M. Johnson, G. B. Dantzig, "Chemical Equilibrium in Complex Mixtures," *The Journal of Chemical Physics*, **28**, 751 (1958); https://doi.org/10.1063/1.1744264.

[137] J. C. Levet and H. Noel, "Synthesis, Crystallographic and Magnetic Properties of the Trivalent Uranium Oxyhalides UOCl, UOBr, and UOI," *Journal of Inorganic Nuclear Chemistry,* **43**, *8,* 1841 (1981); https://doi.org/10.1016/0022-1902(81)80394-6.

[138] K. Grjotheim, J. L. Holm, M. Roetnes, "System $MgCl_2$ - NaCl," (1972) Phase Equilibrium Diagram No. 5661 in *ACerS – NIST Phase Equilibria Diagrams,* National Institute of Standards and Technology, PC Database, Version 4.0, Gaithersburg, Maryland (2013).

[139] A. Blair and H. Ihle, "The Thermal Decomposition and Thermodynamic Properties of Uranium Pentabromide," *Journal of Inorganic Nuclear Chemistry,* **35**, 3795 (1973).

[140] N. V. Galitskii, V. I. Borodin, and A. I. Lystsov, "System $FeCl_2$-NaCl," (1966) Phase Equilibrium Diagram 5660 in *ACerS – NIST Phase Equilibria Diagrams,* National Institute of Standards and Technology, PC Database, Version 4.0, Gaithersburg, Maryland (2013).

[141] L. H. Jepsen, P. Wang, G. Wu, Z. Xiong, F. Besenbacher, P. Chen, and T. R. Jensen, "Thermal Decomposition of Sodium Amide, $NaNH_2$, and Sodium Amide Hydroxide Composites, $NaNH_2$-NaOH," *Physical Chemistry Chemical Physics*, **18**, 25257 (2016).

[142] W. I. F. David, J. W. Makepeace, S. K. Callear, H. M. A. Hunter, J. D. Taylor, T. J. Wood, and M. O. Jones, "Hydrogen Production from Ammonia Using Sodium Amide," *Journal of the American Chemical Society*, **136**, 13082 (2014).

[143] C. A. Kraus, "System NaCl-UCl_3," (1959) Phase Equilibrium Diagram 1318 in *ACerS – NIST Phase Equilibria Diagrams*, National Institute of Standards and Technology, PC Database, Version 4.0, Gaithersburg, Maryland (2013).

[144] S. Ghosh, B. P. Reddy, K. Nagarajan, K. C. H. Kumar, "Experimental Investigations and Thermodynamic Modeling of KCl-LiCl-UCl_3 System," *CALPHAD: Computer Coupling of Phase Diagrams and Thermochemistry*, **45**, 11, (2014).

[145] J. A. Plambeck, "Fused Salt Systems," in *Encyclopedia of Electrochemistry of the Elements*, Vol. X, ed. A. J. Bard, Marcel Dekker, Inc., New York (1976).

[146] I. G. Suglobova and D. E. Chirkst, "System KCl-UCl_3," (1981) Phase Equilibrium Diagram 93-275 in *ACerS – NIST Phase Equilibria Diagrams*, National Institute of Standards and Technology, PC Database, Version 4.0, Gaithersburg, Maryland (2013).

[147] C. J. Barton, A. B. Wilkerson, T. N. McVay, R. J. Sheil, and W. R. Grimes, "System KCl-UCl_4," (1959) Phase Equilibrium Diagram 1282 in *ACerS – NIST Phase Equilibria Diagrams*, National Institute of Standards and Technology, PC Database, Version 4.0, Gaithersburg, Maryland (2013).

[148] T. Schleid and G. Meyer, "NaU_2Cl_6, a Reduced Metallic Chloride of Uranium," *Naturwissenshaften*, 76, 118 (1989).